Xia, Yuanjie (2024) *Reconfigurable liquid crystals for wearable applications.* PhD thesis.

https://theses.gla.ac.uk/84284/

Reconfigurable Liquid Crystals for Wearable Applications

Yuanjie Xia

12 DEC 2023

To my parents,
Supervisors and Friends.

Abstract

This thesis explores the integration of liquid crystal (LC) materials into wearable devices, focusing on applications beyond Liquid Crystal Displays (LCDs). The investigation begins with a thorough review of smart contact lenses and glasses, identifying a gap in research on LC materials for vision assistance. Subsequent chapters introduced the background of LCs and summarized materials and techniques for LC cell fabrication. After that, I proposed methods for depositing materials on patterned surfaces, which could be used for the next generation of optic devices. Subsequently, my thesis demonstrates the reconfigurability of an antenna for smart glasses applications using LC materials, where the resonant frequency of the antenna can be tuned by LC substrate from 3.3 to 3.8 GHz. Moreover, due to the selective reflection nature of cholesteric liquid crystals (CLCs), I have shown how CLCs can be used in smart glasses. For example, I proposed CLC-based vision assist modules, which involve a CLC-based optical combiner (OC) and thermal-controlled glass lenses for epilepsy treatment. The CLC-based OC is able to seamlessly switch smart glasses between augmented reality (AR), virtual reality (VR), and transparent modes via temperature variation. Furthermore, the tunable glasses lens was proposed utilizing selective reflection of CLC materials to block a range of wavelengths of light that would trigger photosensitive epilepsy, showcasing the versatility of LC materials in healthcare applications. In conclusion, this thesis contributes to the advancement of reconfigurable and adaptive solutions in various wearable technologies using LC material, addressing critical aspects of Human-Machine Interaction (HMI) and healthcare needs.

Contents

List of Tables

List of Figures

xi

Acknowledgements

I would like to express my sincere gratitude to my advisors, Prof. Rami Ghannam and Prof. Hadi Heidari, for their invaluable guidance, unwavering support, and insightful feedback throughout the entire research process. Their expertise and encouragement have been instrumental in shaping this work.

I am also thankful to the members of my research group, including the ICE research group and meLAB, for their constructive comments and valuable suggestions that greatly enhanced the quality of this thesis.

I extend my appreciation to my colleagues and friends who contributed to the research discussions and provided a stimulating academic environment.

Last but not least, I want to express my deepest gratitude to my family for their unwavering support, love, and understanding throughout this academic journey.

This research would not have been possible without the collaborative efforts and support of all those mentioned above. Thank you.

Declaration

I declare that, except where explicit reference is made to the contribution of others, that this dissertation is the result of my own work and has not been submitted for any other degree at the University of Glasgow or any other institution

_____

Yuanjie Xia

Abbreviations

- **5CB** - 4-Cyano-4'-pentylbiphenyl

- **5CT** - 4-Cyano-4´-n-pentyl-p-terphenyl

- **8OCB** - 4 -(Octyloxy)-4-biphenylcarbonitrile

- **AFM** - Atomic Force Microscopy

- **AgNW** - Silver Nanowire

- **AR** - Augmented Reality

- **BJT** - Bipolar Junction Transistor

- **CLC** - Cholesteric Liquid Crystal

- **CNTs** - Carbon Nanotubes

- **FDA** - Food and Drug Administration

- **FOV** - Field of View

- **HCl** - Hydrogen Chloride

- **HMD** - Head-mounted Display

- **HUD** - Head-up Display

- **HMI** - Human-Machine Interaction

- **HTP** - Helical Twisting Power

- **IMU** - Inertial Measurement Unit

- **IoT** - Internet of Things

- **ITO** - Indium Tin Oxide

- **IPA** - Isopropyl Alcohol

- **LC** - Liquid Crystal

- `LCoS` - Liquid Crystal on Silicon

- `LED` - Light-Emitting Diodes

- `LdG` - Landau de Gennes

- `LHCLC` - Left-handed Cholesteric Liquid Crystal

- `MIMO` - Multiple Input Multiple Output

- `MR` - Mixed Reality

- `MOSFET` - Metal Oxide Semiconductor Field-effect Transistor

- `NED` - Near-eye Display

- `NLC` - Nematic Liquid Crystal

- `NTC` - Negative Temperature Coefficient

- `OLEDs` - Organic Light-Emitting Diodes

- `PCB` - Printed Circuit Board

- `PEDOT:PSS` - Poly(3,4-ethylenedioxythiophene) Polystyrene Sulfonate

- `PI` - Polyimide

- `PID` - Proportional-Integral-Derivative

- `PMMA` - Poly(methyl methacrylate)

- `PWM` - Pulse-width modulation

- `PVA` - Polyvinyl Alcohol

- `PVC` - Polyvinyl Chloride

- `R811` - (R)-2-Octyl 4-[4-(Hexyloxy)benzoyloxy]benzoate

- `RF` - Radio Frequency

- `RFID` - Radio Frequency Identification

- `RGB` - Red Green Blue

- `RHCLC` - Right-handed Cholesteric Liquid Crystal

- `S1011` - 4-(trans-4-pentylcyclohexyl)-1,1'-[(1(S)(+))-1-phenyl-1,2-ethanediyl] ester

- `S811` - (S)-2-Octyl 4-[4-(Hexyloxy)benzoyloxy]benzoate

- `SAR` - Specific Absorption Rate

- `SEM` - Scanning Electron Microscope

- `TN` - Twisted Nematic

- `VR` - Virtual Reality

- `WPT` - Wireless Power Transfer

- ZBD - Zenithal Bistable Device

List of Publication

During my PhD, I published four journal papers and four conference papers:

- "Beyond Flexibility: Transparent Silver Nanowire Electrodes on Patterned Surfaces for Reconfigurable Devices", Accepted for Publication on Advanced Engineering Materials

- "Reconfigurable Wearable Antenna for 5G Applications using Nematic Liquid Crystals", Published on Nano Select, Wiley, 2023.

- "State-of-the-Art in Smart Contact Lenses for Human Machine Interaction", Published on IEEE Transactions on Human-Machine Systems, IEEE, 2022.

- "Low Cost Real-time Eye Tracking System for Motorsports", published on 29th IEEE International Conference on Electronics, Circuits and Systems (ICECS), IEEE, 2022

- "Analysis and Comparison of Two-and Four-State Operation Modes of Parallel-Hybrid Multi-Path Buck DC-DC Converter", published in 2022 29th IEEE International Conference on Electronics, Circuits and Systems (ICECS), IEEE, 2022

- "Reconfigurable Surfaces Using Fringing Electric Fields from Nanostructured Electrodes in Nematic Liquid Crystals", Published on Advanced Theory and Simulations, Wiley, 2021

- "Hybrid Microenergy Harvesters for Smart Contact Lenses", Published on 27th IEEE International Conference on Electronics, Circuits and Systems (ICECS), IEEE, 2020

- "Smart Wristband for Gesture Recognition", Published on International Conference on UK-China Emerging Technologies (UCET), IEEE, 2020

In addition to the above, I have submitted the following articles, which are currently under review :

- "Cholesteric Liquid Crystal Based Reconfigurable Optical Combiner for Head-Mounted Display Application", submitted to IEEE VR 2024 and has the possibility to be accepted by IEEE Transactions on Visualization and Computer Graphics.
- "Thermal Controlled Cholesteric Liquid Crystal Wavelength Filter Lens for Photo-sensitive Epilepsy Treatment", submitted to Nature Communications, Nature.

<div align="right">Chapter 1</div>

Using Our Eyes for Human-Machine Interaction

Human-machine interaction (HMI) is concerned with how people and automated systems interact and communicate with each other. This has long ceased to be confined to just traditional machines in the industry and now also relates to computers, digital systems or devices for the 'Internet of Things' (IoT) [1]. More and more devices are connected and automatically carry out tasks in the background. Operating all of these machines, systems and devices need to be intuitive and must not place excessive demands on users. Therefore, smooth communication between people and machines requires user-friendly interfaces. Smart contact lenses and smart glasses are two optional interfaces that could broaden the potential applications and facilitate HMI using our eyes.

Firstly, in Section 1.1 and 1.2, I will demonstrate how the eyes can be used for HMI applications from a physiological and technical perspective. Next, in Section 1.3 and 1.4 of the chapter I will discuss the State-of-the-Art review papers on smart contact lenses and smart glasses. Additionally, I will describe the methodology for compiling relevant research articles that match the search criteria. Subsequently, I will discuss and analyse the results from the search, which enable me to determine the direction of future research direction.

1.1 Physiology of the Eye

Before reviewing the range of contact lens and glasses technologies that can be used for HMI, it is important to understand the basic physiology of the eye, how it moves and what are the muscles responsible for this movement. The eye is a spherical organ with a mean diameter of around 24 mm. As demonstrated in figure 1.1, eye rotation is controlled by six ocular muscles, which are the superior rectus, inferior rectus, lateral rectus, medial rectus, superior oblique and inferior oblique. The contraction of these six eye muscles results in eye movements [2]. There are three main reasons for eye movements, which are reducing image motion, positioning the fovea and avoiding double vision [3, 4]. Moreover, there are six types of basic eye movements, which include abduction, adduction, supraduction, infraduction, incyclotorsion and excyclotorsion [5]. In abduction and adduction, the cornea moves away from and towards the midline, respectively. Similarly, supraduction and infraduction mean that the cornea moves upwards and downwards, respectively. In addition to the previous four movements, the eye can rotate clockwise or counterclockwise thanks to the superior oblique and inferior oblique muscles, respectively. In fact, every complex eye movement is made up of these six basic eye movements, which could be controlled by humans consciously.

(a)   (b)
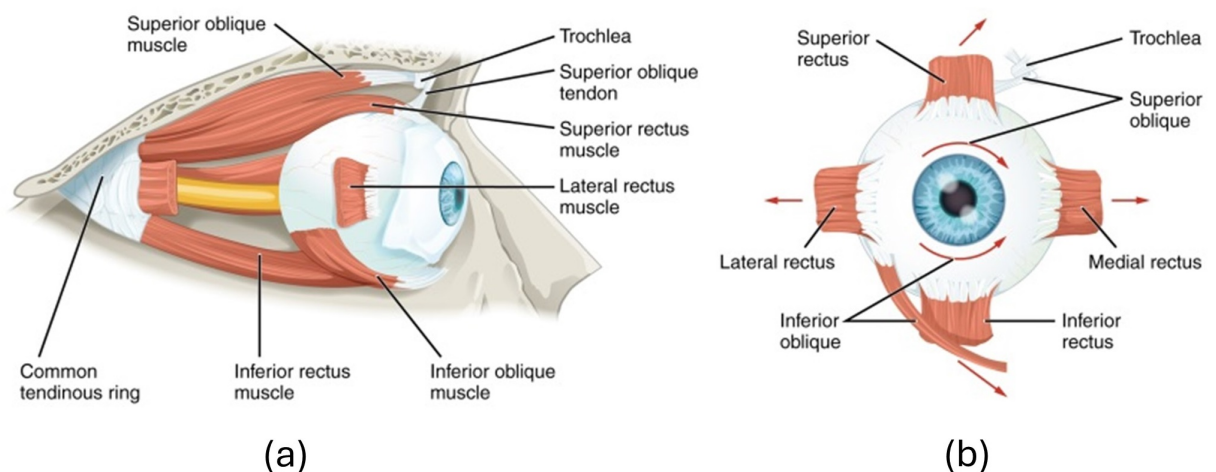
Figure 1.1: (a) Lateral view of the right eye and (b) Anterior view of the right eye, which shows six essential muscles that are responsible for eye movements. (Adapted from [6] © 2021, StatPearls Publishing LLC.)

1.2 Advantages of Eyes for Human-Machine Interaction

HMI applications require an input device, which may involve a touch-screen device, touch pad or keyboard [7]. However, most of these input devices require manual manipulation. Moreover, since our eyes are used to collect the necessary visual information from these machines, we can also use them to control and interact with these machines for HMI applications. Consequently, hardware and software can be developed to detect eye movements and gestures such as gaze and blinking to facilitate HMI. In fact, there are a variety of methods in the literature that can be used for gaze and eye tracking, which include computer vision [8, 9], magnetic sensing [10] and laser sensing [11].

Therefore, in comparison to traditional input devices, eye-related gesture recognition and tracking avoid physical contact and benefit people with impaired movement. For example, previous studies in the literature confirmed that eye blinking could be used to facilitate HMI [12, 13]. Here, 'blinking' is a semi-automatic reflex function that is controlled by two muscles, which are the levator palpebrae superioris and the orbicularis oculi [14]. People sometimes blink consciously as a form of body language or gesture, which is interpreted as 'winking'. Therefore, by combining blink detection, gaze tracking and eye movement, our eyes could be used as an effective and user-friendly interface for HMI applications. HMI using our eyes can be achieved in two ways: through smart contact lenses and smart glasses. Therefore, I will introduce the pros and cons of each of these methods in the following sections.

1.3 The Development of Smart Contact Lens

1.3.1 Overview

Contact lenses are thin lenses which can be placed directly on the surface of human eyes. They have historically been used for vision correction and they were first developed by Adolf Fick in 1887 to correct astigmatism [15]. These lenses have now undergone a series of innovations and are gaining popularity due to recent developments in materials engineering and microfabrication. Currently, these innovative platforms are mainly being considered for a plethora of medical applications since they are noninvasive [16] and can be used to deliver medicines [17]. In comparison to traditional implantable devices, contact lenses do not require surgery and are capable of monitoring bio-markers continuously. This is especially true since tear fluid carries philological bio-markers that can be used to monitor the health of its wearer [18].

Advancements in smart contact lenses were impeded by the ability to communicate the 'sensed' data wirelessly. In fact, this technological challenge hindered the development of smart contact lenses during the past two decades. However, advanced microfabrication technologies enabled miniature electronic components to be integrated into a contact lens. Contact lenses can now integrate sensors, driver electronics, energy modules, antennae and I/O terminals on the same platform. Progress in microelectronics packaging technology as well as nanofabrication and nanocommunications has therefore resulted in multiple potential applications for smart contact lenses. For example, in addition to their use for vision correction, medical staff could potentially monitor diabetes patients in real-time using these smart contact lenses [19–21].
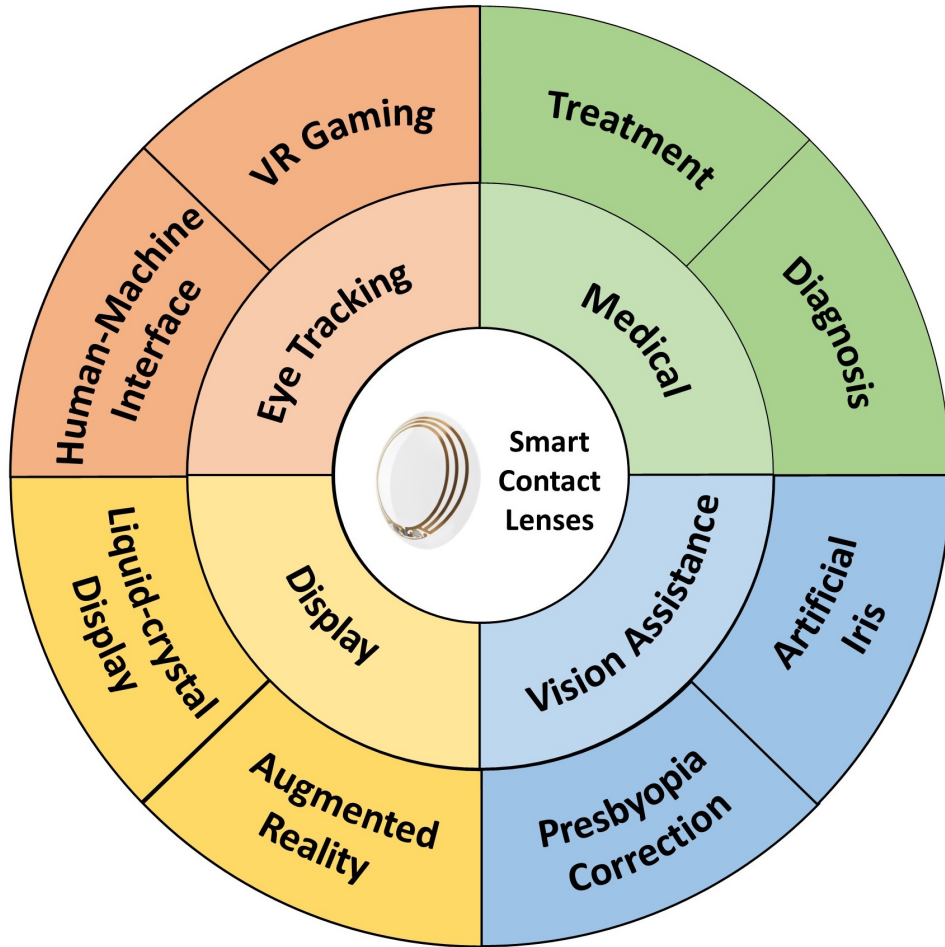
Figure 1.2: Range of contact lens applications for HMI that include medical, eye tracking, display and vision assistance.

In addition to the healthcare field, there are a variety of promising smart contact lens applications, as shown in Fig. 1.2. According to my investigations, applications of existing smart contact lenses could be divided into four main categories, which are: (a) eye tracking, (b) healthcare (medical), (c) displays and (d) vision correction. I will discuss recent progress in each of these application areas in the Application section. Moreover, I identified six constituent building blocks of smart contact lenses, which are the (a) Sensor, (b) Energy, (c) Driver Chip, (d) Communications, (e) Input/Output (I/O) Interface and (f) Substrate & Interconnection modules. I chose to discuss recent developments in smart contact lenses according to these five building blocks. As is shown in Fig. 1.3, the energy module is concerned with power harvesting and storage, while the Driver Chip module provides and regulates this energy, ensuring all electronic modules operate safely. Furthermore, I included a fifth module called "Substrate & Interconnection", which hosts and connects all these electronic modules together.
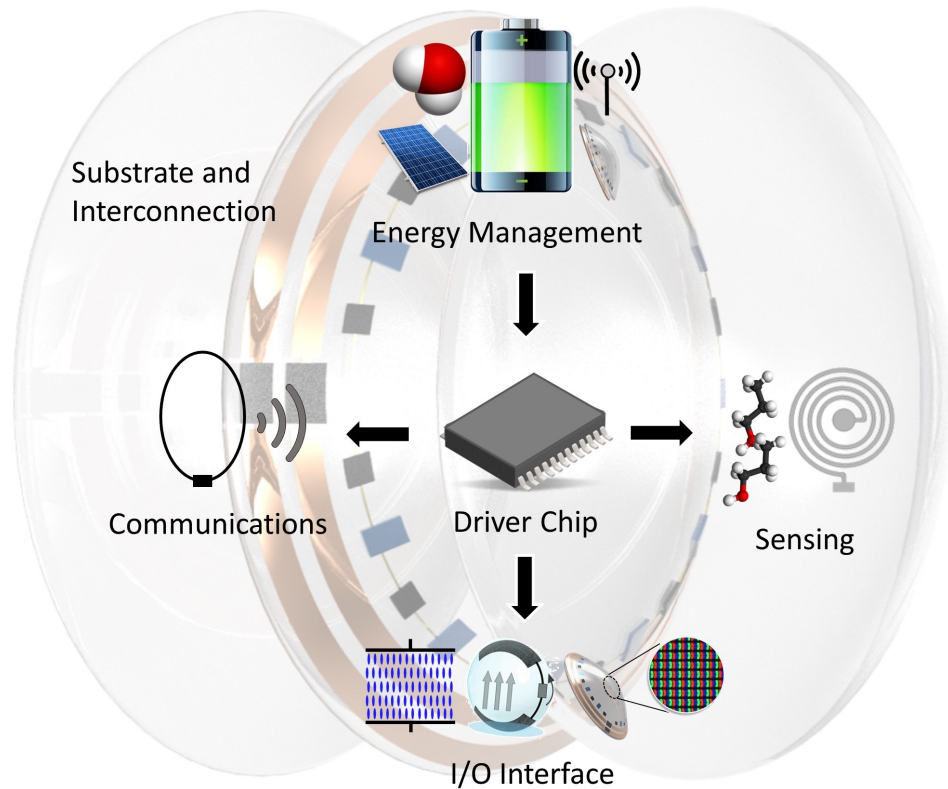
Figure 1.3: Constituent building blocks of smart contact lenses, which include the Energy Management, Communications, Driver Chip, Sensing, I/O Interface and the Substrate & Interconnection modules.

1.3.2 State of the Art

Over the past two decades, major advances in electronics have allowed researchers to design and integrate miniature electronic systems into contact lens platforms. Smart contact lenses have become an increasingly popular topic in electronic wearable devices. In previous studies, researchers have proposed and realized contact lenses for health monitoring, gaze tracking and many other applications. The purpose of this subsection is to survey the latest review articles on contact lens technology. In table 1.1, I summarized the published year and contributions of 3 previous review papers in this field. Additionally, I will conclude the limitations of previous review papers and show how my work could address the limitations.

Table 1.1: Comparison with previous literature review

Ref.	Year	Contribution
[22]	2015	Survey on contact lenses for biosensing applications. Manuscript also reviews the contact lens market and the Food and Drug Administration (FDA) regulatory requirements.
[23]	2018	Survey on tear-based biosensing technology.
[24]	2020	Survey on contact lenses for medical applications, which includes the latest trends in biosensing, information transmission, drug delivery and energy storage.
[25]	2022	Systematic review of current trends, challenges and future research directions on smart contact lenses for a wide variety of applications, including medicine, displays, vision assistance and eye tracking.

Farandos *et al.* published the first review article on smart contact lenses in 2015 [22]. They confirmed that contact lenses are attractive platforms for health monitoring applications in comparison to other wearable technologies due to their 'minimalistic nature'. Their manuscript started with background information regarding the physical characteristics of the eye, followed by an analysis of tear fluid composition. They reviewed the state-of-the-art contact lens sensor fabrication, and detection techniques as well as the energy harvesting and readout systems. They also analyzed the market for contact lenses and FDA regulatory requirements for the commercialization of contact lens sensors. Their manuscript focused on reviewing advances in monitoring intraocular pressure (IOP) and tear glucose, which were the two main application areas of smart contact lenses at that time. Their paper mentioned that commercial contact lens products require sufficient selectivity, sensitivity, and reproducibility and could ensure patient compliance. They also mentioned that treatment capabilities could be integrated into the contact lens platform. For future development, they highlighted three main challenges with contact lenses, which were energy harvesting, wireless connectivity and sensor stability.

Moreover, in 2018 Tseng *et al.* evaluated different kinds of contact lenses for biosensing applications [23]. Their article focused on reviewing the different methods for using tear fluid as a detection medium for different diseases such as cancer, ocular disorders and diabetes. They reviewed previous manuscripts about tear content and evaluated both

active as well as passive sensors for tear content sensing. Their review paper predicted that future smart contact lenses would lead to better personalized medical treatment. Similar to the review article by Farandos *et al.*, they again highlighted that contact lens stability and sensor data repeatability are a challenge. Other challenges that were mentioned were wearer comfort and cost.

In 2020, Kim *et al.* published another review article on smart contact lenses for biosensing applications that focus on disease diagnosis [24]. Their review analysed both physical and chemical sensors. They also briefly introduced state-of-the-art contact lenses for drug delivery, data transmission and power storage. They mentioned that further research is necessary to fully appreciate what biomarkers can be detected in tear fluid. They also indicated that an optimisation of sensor accuracy is necessary since this depends on the nature of the disease to be detected and some diseases require higher sensing accuracy than others. Moreover, they raised concerns regarding sensor stability and biocompatibility. However, they concluded that smart contact lenses could enable noninvasive health monitoring and diagnosis based on people's tear fluids, which is likely to be used more extensively.

Based on the above, state-of-the-art review articles on smart contact lenses have focused on biosensing applications. In this chapter, I aimed to systematically review the range of contact lens technologies that facilitate HMI. These technologies include biosensing and other relevant technologies, such as LCDs and AR. In this context, this work goes beyond existing review articles in this field, since it aims to showcase how contact lenses have supported HMI and have been used in applications other than the medical field.

1.3.3 Methodology

In this subsection, I define the research methodology for collecting and synthesizing evidence on smart contact lenses using clearly defined criteria. Academic journal articles and conference papers were chosen for review, considering their relatively high impact. Web of Science, which was one of the largest academic databases, was used for identifying the articles using certain keywords to confine the results. In addition, the keywords that were used for the search query are shown in table 1.2. The (AND) Boolean operator was used to connect these descriptors. All manuscripts that contain the aforementioned keywords were included in the review.

Similar to the methodology described in [26], I first defined the research questions and the inclusion criteria of the search. Second, I selected relevant manuscripts that met these criteria. Third, I analyzed and interpreted the search results. In this case, I defined the following research questions (RQ):

1. RQ1: Where is the research activity on smart contact lenses mainly located?
2. RQ2: What are the building blocks and device architectures?
3. RQ3: What are the applications and different ways in which contact lenses have been used to facilitate HMI?

Based on the above questions, the following inclusion criteria (InC) were defined:

1. InC 1: Articles written in English;
2. InC 2: Articles matching the definitions and descriptors mentioned in table 1.2.

Table 1.2: Descriptors and synonyms used for the search

Descriptor	Definition	Synonyms
Contact Lens	Contact lenses are thin lenses placed directly on the surface of the eyes [27]	Contacts, soft lenses and extended-wear lenses
Smart	A smart device is able to do many of the things that a computer does [28]	Autonomous
Electronic	An electronic device has transistors or silicon chips which control and change the electric current passing through the device [29]	Electronics
Wireless	Wireless technology uses radio waves rather than electricity and therefore does not require any wires [30]	Radio Frequency (RF) powered

Having defined the research questions as well as the inclusion criteria, I defined the approach in searching for the relevant literature. I used the 'Web of Science' portal for the search with the descriptors: smart contact lens, electronic contact lens, wireless contact lens and sensing contact lens. A forward and backward search was also performed via 'Google Scholar' to make sure that all literature had been captured.

1.3.4 Results and Discussion

In this subsection, I will analyze the literature on smart contact lenses for HMI applications. In total, 83 manuscripts satisfied the search criteria, which were described previously.
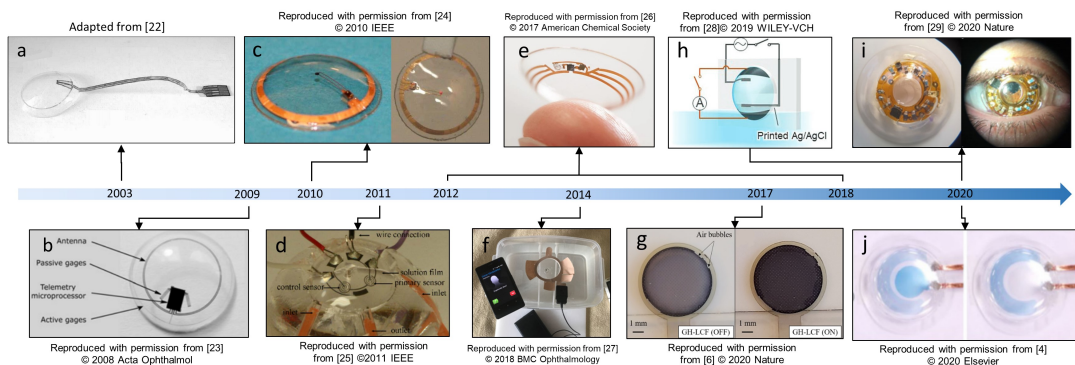
Figure 1.4: Timeline of smart contact lens development from 2000 to 2020.

The timeline of the development of smart contact lens was demonstrated in Fig. 1.4. The earliest smart contact lens developed by M. Leonardi *et al.* in 2003[31], as shown in Fig. 1.4 a. Subsequent advancements in the micro-fabrication industry led to the development of more sophisticated contact lenses six years later, as shown in Fig. 1.4 b. For example, the first contact lens was designed for intraocular pressure (IOP) monitoring [32]. In Fig. 1.4 c, an antenna was integrated into a contact lens for energy harvesting. The harvested power was used to power a single-pixel LED [33]. Fig. 1.4d demonstrated the first contact lens designed for glucose monitoring [34]. Fig. 1.4 e showed that Google aimed to commercialize contact lenses for glucose measurement, but the project was discontinued due to inaccuracies when using tear glucose to predict blood glucose [35]. After that, as shown in Fig. 1.4 f, SENSIMED also developed and commercialized contact lenses for IOP sensing [36]. Fig. 1.4 showed the first contact lens artificial iris design used LCs for changing the transparency of the contact lens [20]. The Fig. 1.4 h to j show the most recent smart contact lens applications for dry eye treatment [37], gaze tracking [38] and hazard perception [18].
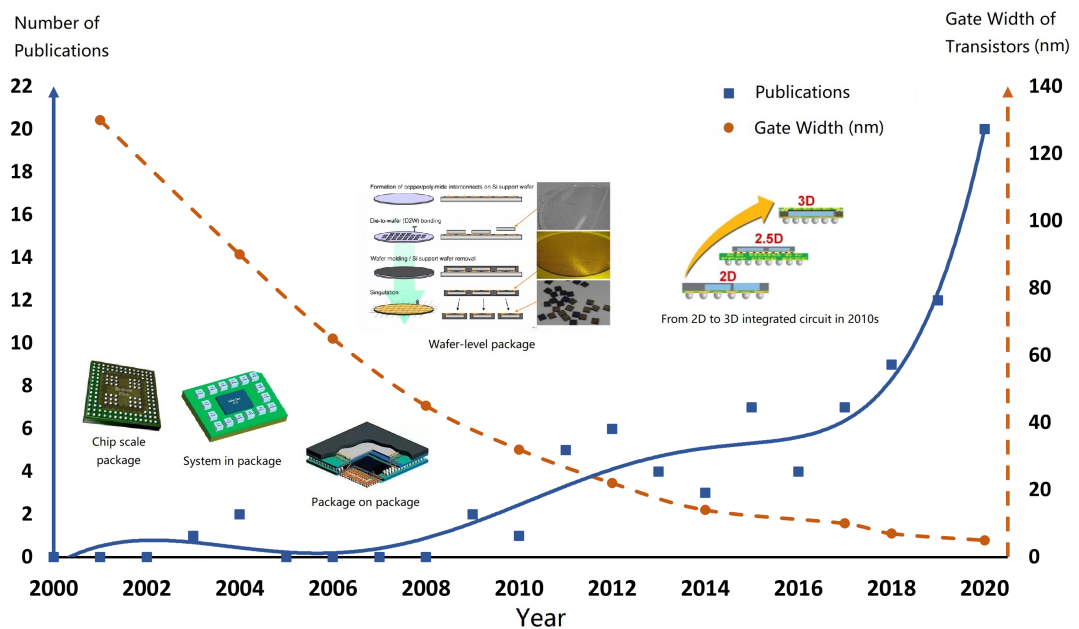
Figure 1.5: Comparison between the publications activity on smart or electronic contact lenses with CMOS gate width dimensions. A rise in publications activity started in 2008, which corresponded to the 45 nm gate width.

A total of 37 articles were published from Asia, 22 from Europe, 22 from North America, and 2 from South America. The majority of these manuscripts (approximately 61%) were published during the past 5 years. Therefore, in response to RQ1, the Asian continent is most productive in contact lens research.
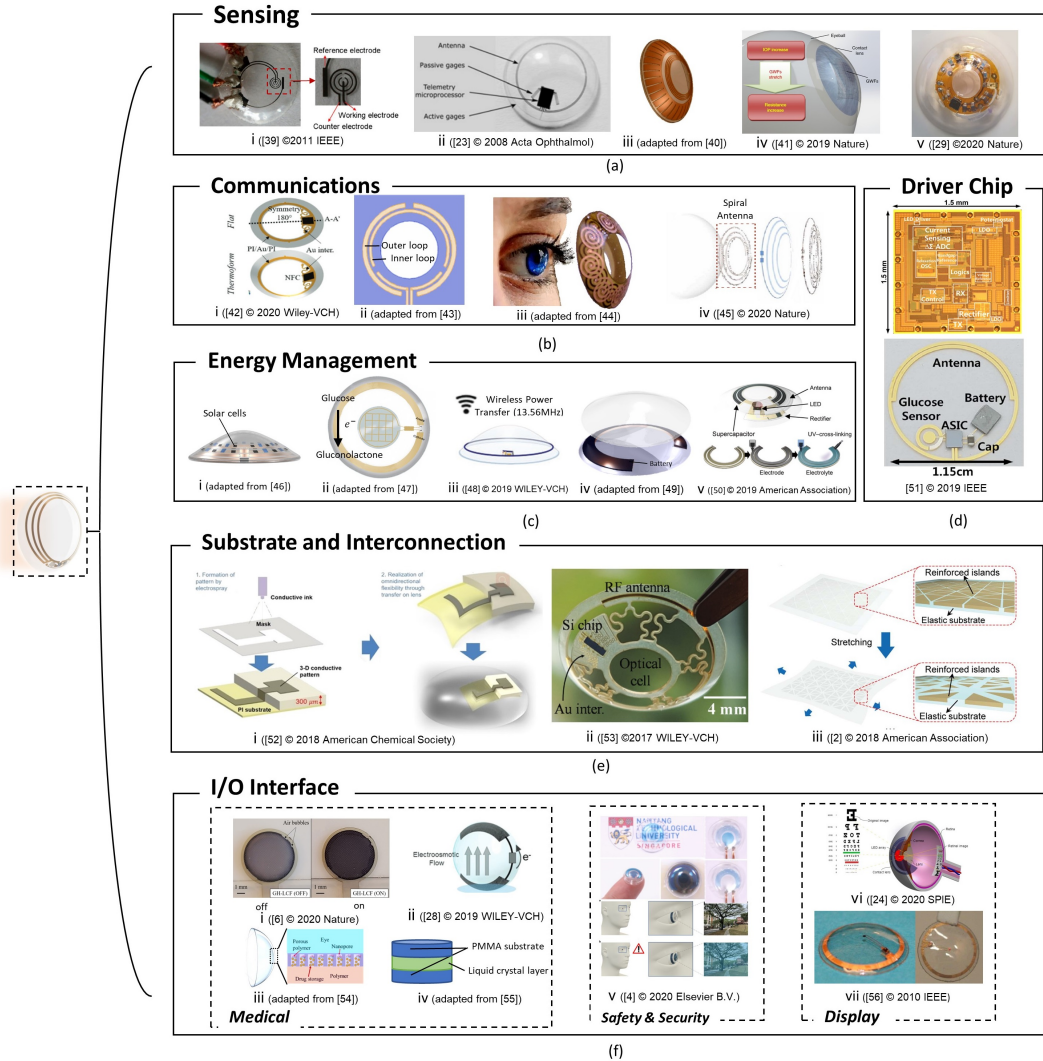
Figure 1.6: Essential building blocks of a smart contact lens, which include: (a) Sensors: (i) Glucose sensing [39], (ii) IOP sensing [32], (iii) IOP sensing [40], (iv) IOP sensing [41] and (v) Eye tracking [38]. Subfigure (b) demonstrates different types of antenna design including: the loop antennae as demonstrated by (i) [42], (ii) [43]; the spiral antenna as demonstrated by (iii) [44], and (iv) [45]. Subfigure (c) demonstrates different types of energy modules including: energy harvesters, as demonstrated by (i) [46], (ii) [47] and (iii) [48]. Moreover, power storage methods in contact lenses were demonstrated by (iv) [49] and (v) [50]. Subfigure (d) shows a driver chip design [51]. Subfigure (e) demonstrates innovative substrate and interconnection design for smart contact lenses [52, 53, 16]. Subfigure (f) demonstrates input/output terminal block for applications that include, (i) an artificial iris [20], (ii) dry eye treatment [37], (iii) drug delivery [54], (iv) presbyopia treatment [55], (v) safety & security [18], (vi) display demonstrated [33] (v) display [56].

Accordingly, I noticed an onset of research interest in smart or electronic contact lenses from 2008, as shown in Fig. 1.5. This is just one year after the emergence of the first Apple iPhone (2007). It is also just four years after the beginning of the nanometer-sized transistors. The year 2008 also signifies an important milestone in the transistor industry, since it marks the emergence of the 45 nm node technology, thus paving the way for advanced processors such as the atom and the core i7 [57]. Such critical technological advancements had an important role in the development of electronic components of contact lens systems. I will discuss the range of technologies in each of these sections. In fact, 50 articles have been published since 2015, which accounts for 73.5% of all the publications on smart or electronic contact lenses. I also observed an obvious rise in publications in this field from 2000 to 2020, as is shown in Fig. 1.5.
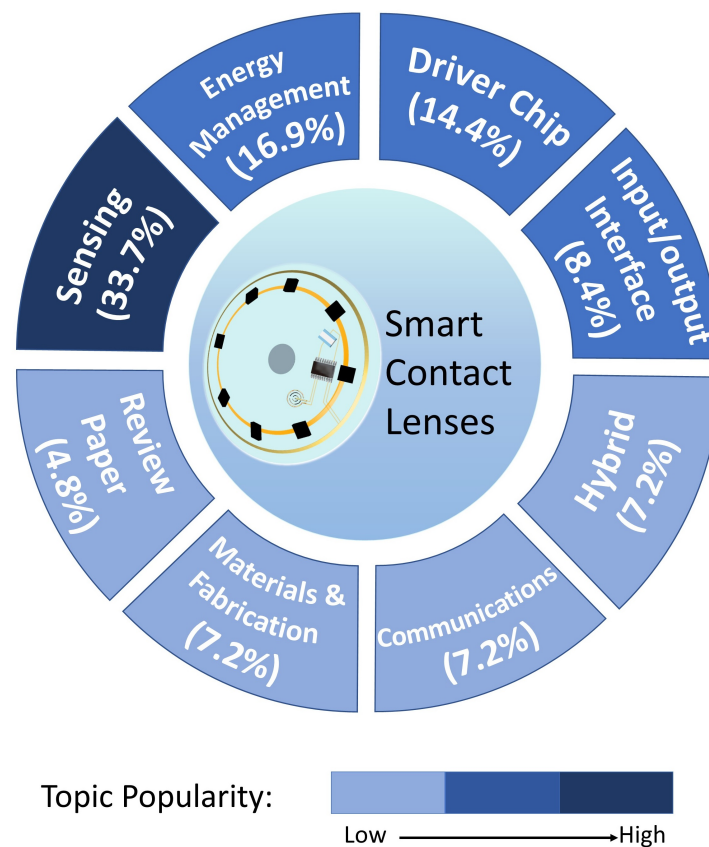
Figure 1.7: Different components and building blocks of a smart contact lens. These are the Sensing, I/O Interfacing, Communications, Driver Chip and Substrate and interconnecting modules. A hybrid category was introduced to include smart contact lens developments in more than one building block. This search also included four review papers. According to the search, the majority of the literature has focused on developments in the sensing, energy and driver chip modules, with fewer publications on the Communications and well as I/O Interfacing modules.

To address RQ2 and based on the gathered research data, recent developments in smart contact lenses can be categorised according to the six previously mentioned building blocks. Approximately 7% of these manuscripts reported developments in more than one building block and a "Hybrid" category was introduced, as shown in figure 1.7. Furthermore, almost a third (33.7%) of all the literature was devoted to the "Sensing" category, whereas roughly another third reported developments in the "Energy" and "Driver Chip" modules (16.9% and 14.4% of manuscripts, respectively). With the exception of the "Hybrid" papers and the four Review papers, a fifth of all the literature reported developments in the remaining four building blocks of smart contact lenses.

1.3.5 Applications

To address RQ3 and according to the review, 58 out of the 83 manuscripts specifically mentioned an application for their contact lenses. I subsequently identified four main areas where these contact lenses were used, which include (i) medicine, (ii) displays, (iii) eye tracking and (iv) vision assistance. From these application areas, the medical field accounts for almost three quarters (74%) of all publications in smart contact lenses, as shown from the results presented in Fig. 1.8.

Medical applications of smart contact lenses include the measurement of corneal temperature [58], intraocular pressure (IOP) [59, 60] and glucose levels [61–63]. Continuously monitoring these health indicators helps improve disease diagnosis and treatment. In addition to these health indicator measurements, contact lenses have also been used for treating dry eye disease [64, 37] and for releasing drugs [54].
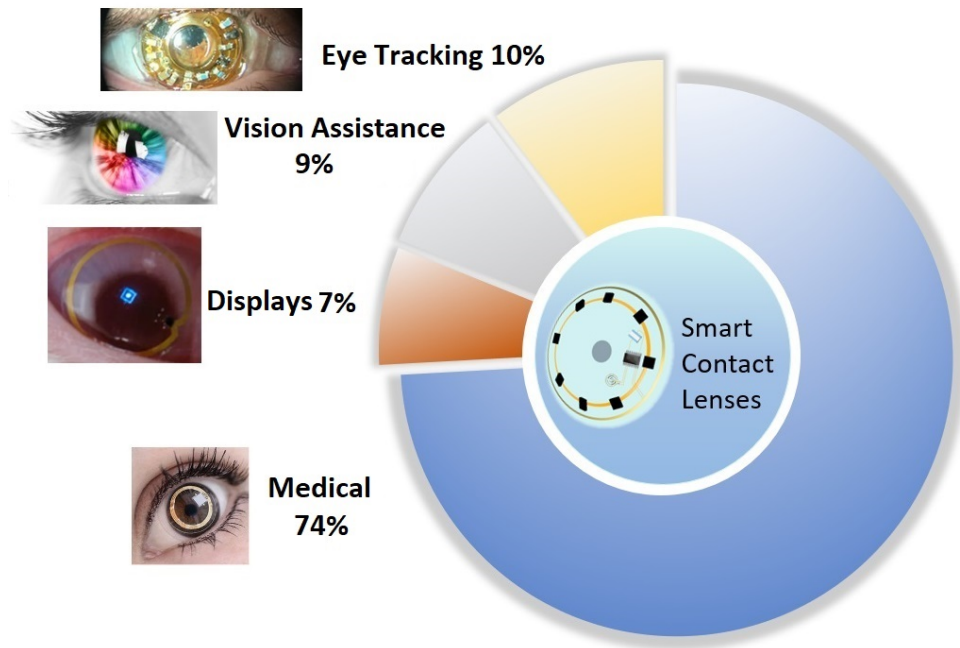
Figure 1.8: Pie chart for smart contact lens applications. The pie chart above shows the distribution of the application areas in the reviewed manuscripts.

Since 2016, smart contact lenses have been used in other non-medical applications. For example, they have been used in applications that include vision assistance, display and eye tracking. Quintero *et al.* proposed a design of an artificial iris with smart contact lens and LC material [20] for vision correction, as demonstrated in Fig. 1.6e i. A similar design was also made by Raducanu *et al.* [21] and Vanhaverbeke *et al.* [65]. They manipulate LC material by voltage variation. The switching of LC would cause the transparency variation of the contact lens, therefore it can avoid patients with iris diseases exposed to intense light. In addition to artificial iris, Milton *et al.* proposed a novel contact lens design for presbyopia treatment using contact lens and LC [55], which is shown in Fig. 1.6e iv. Their design used the optic and electric properties of LCs. The focus length of the contact lens could be controlled by voltage. Their design could help people with presbyopia adjust the focus length of the contact lens based on their requirements. These studies inspired me to explore using LC materials to fabricate reconfigurable wearable devices.

In terms of HMI, eye tracking using smart contact lenses has also been demonstrated in the literature [66, 11, 10]. Contact lenses with eye tracking functionality could be used in many scenarios. For instance, in virtual gaming and online education, there are projected benefits of contact lenses for entertainment applications in comparison to wearable devices that have limitations with accuracy and can be remedied using contact lenses [11]. Additionally, contact lenses with display modules are also developed to facilitate the HMI. These contact lenses could be used to transmit visualized data, which can be applied in augmented reality applications [56].

Moreover, contact lenses have also been demonstrated for eye tracking applications. Eye tracking is currently a hot topic that enables a computer to detect where the eye is looking. However, current methods rely on cameras and computer vision software as well as signal processing and machine learning algorithms to determine the eye's position. However, these conventional hardware configurations accommodate a limited range of head movement and suffer from poor precision [67]. In contrast, eye-wear-based systems have improved accuracy, tracking speed, mobility and portability, which are important attributes for a wearable HMI application [68].

Furthermore, smart contact lenses were used as near eye display (NED) modules. For example, LC materials were used for displaying information, as demonstrated by the early work of de Smet *et al.* in [69], as well as their most recent work in [20]. The versatility of such materials in contact lenses enabled them to be used for both sensing and display applications [70]. Moreover, the concept of using Light Emitting Diodes (LEDs) in contact lenses for AR applications was proposed by [56]. Although an experimental setup was not shown, simulation results using CODE V software predicted a high resolution smart contact lens with a wide field of view (FOV) that can move or rotate freely without the need for eye tracking.

In terms of eye and gaze tracking applications, camera-less tracking using contact lenses was demonstrated by Massin *et al.*, which was 2.5 times better than current camera-based eye-trackers [66, 11]. In addition to their improved accuracy, such camera-less systems are more cost effective for eye and gaze tracking applications [71].

1.4 The Development of Smart Glasses

1.4.1 Overview & Method

Compared with smart contact lenses, smart glasses have seen more progress and widespread adoption. Due to the size of smart glasses, more electronic components are able to be integrated, which enable more function than smart contact lenses, including display, sensing and communication. According to 'Web of Science', there have over thousands of papers related to key keywords 'smart glasses' and 'wearable glasses' in the last 5 years, which is much more than that of contact lenses. However, due to the large amount of research papers in this area, restrictions need to be added to the search scope to further narrow down the range of articles. Therefore, only journal and review papers that are within the 'Electrical and Electronic Engineering' category are considered. Subsequently, the articles were manually filtered to exclude irrelevant papers, including 40 research papers and 3 review papers. Noticeably, since 'Web of Science Categories' was used to restrict the search scope, all publications in the sample set are in the 'Electrical and Electronic Engineering' field, which results in the number of publications being smaller than that of smart contact lenses. However, the restriction of search scope can help to analyze the current development and trend of smart glasses in the electrical and electronic engineering field. In this section, I focus on summarizing these 43 papers that are related to smart glasses in the electrical and electronic engineering field.
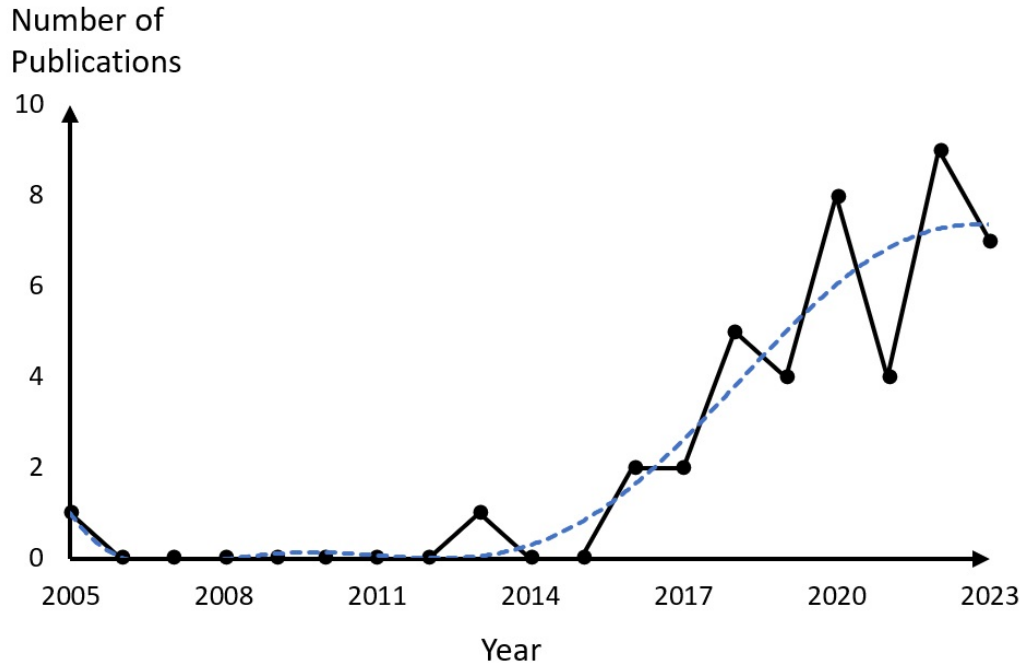
Figure 1.9: The trend of publication relates to 'smart glasses' and 'wearable glasses' in the electronic engineering field.

The eligible papers were categorized by published year, where the trend of publication is shown in Fig. 1.9. A rise in publications activity started in 2012 and the maximum quantity of publication occurs in 2022. In this section, I first established the research questions and the search criteria. Second, I selected relevant journal papers which met these criteria. Third, I analyzed and discussed the search results. In this case, I defined the following research questions (RQ):

1. RQ1: Where is the research activity on smart glasses mainly located?
2. RQ2: What are the applications of smart glasses?
3. RQ3: What are the challenges and future research directions?

1.4.2 State-of-the-Art

To start with, I summarized three previous review papers and listed them in Table 1.3. Anna *et al.* reviewed available AR glasses products in the smart factory in 2017. The purpose of the paper is to facilitate and accelerate the adoption of AR technology in the manufacturing industry. The researchers indicated that the massive quantity and range of available AR product choices make it complicated to identify the best alternative. To address the issue, the paper proposed a process to evaluate AR glasses, which enables companies to quickly make optimal decisions about AR products.

Apart from that, Lee *et al.* reviewed the interaction methods for smart glasses in 2018. This review summarized up-to-date interaction methods of smart glasses, including handheld, touch and touchless input. After that, they discussed present research challenges within the field of human-computer interaction using smart glasses. The researchers also provided an overview of the ongoing research of touch and touchless input methods.

In 2020, Cecilia *et al.* reviewed the adoption of AR/VR glasses in Industry 4.0. Industry 4.0 refers to the industry concerning the fourth industrial revolution. Compared with Anna's review in 2017, this review includes the application of VR glasses in the industry. They discussed whether AR/VR systems or devices designed for industrial applications can fulfil the requirements of the industry. In addition, they also explored whether AR/VR devices are designed to facilitate the operation of factories.

According to the summary of previous review articles, I noticed that they are more focused on the application of smart glasses rather than the techniques being applied to smart glasses. Here, I reviewed techniques being applied to smart glasses in electrical and electronic engineering aspects.

Table 1.3: Previous literature review of smart glasses in electrical and electronic engineering category

Reference	Year	Contribution
[72]	2017	Survey on tear-based biosensing technology.
[73]	2018	Survey on using AR glasses in the smart factory.
[74]	2020	Survey on the adoption of AR/VR glasses in industry 4.0.

1.4.3 Results and Discussion

Apart from three review papers, there are 40 technical articles in the sample set, which can be divided into 7 categories including antenna, display, HMI, sensing, system design, thermal analysis and tunable lenses. Almost a quarter (27.5%) of the literature was devoted to the 'Antenna' category, which makes it the highest proportion among all. Furthermore, approximately 22.5% of these manuscripts reported developments in smart glasses systems, where the 'System Design' category was introduced, as is shown in figure 1.10. The literature reported developments in the 'Sensing' and 'HMI' modules have similar quantities, which are 20% and 17.5%, respectively. In addition to that, only a few literature were related to 'Thermal Analysis', 'Tunable Lens' and 'Display', which are 5%, 5% and 2.5%, respectively. In this section, I will provide a comprehensive introduction and discussion for each category.

1.4.3.1 Antenna

There are over a quarter of publications are related to antenna design and integration. To be specific, there are two main proposes for integrating antenna into smart glasses, including communication and energy harvesting. In this section, I will introduce the representative publications and present personal insights.
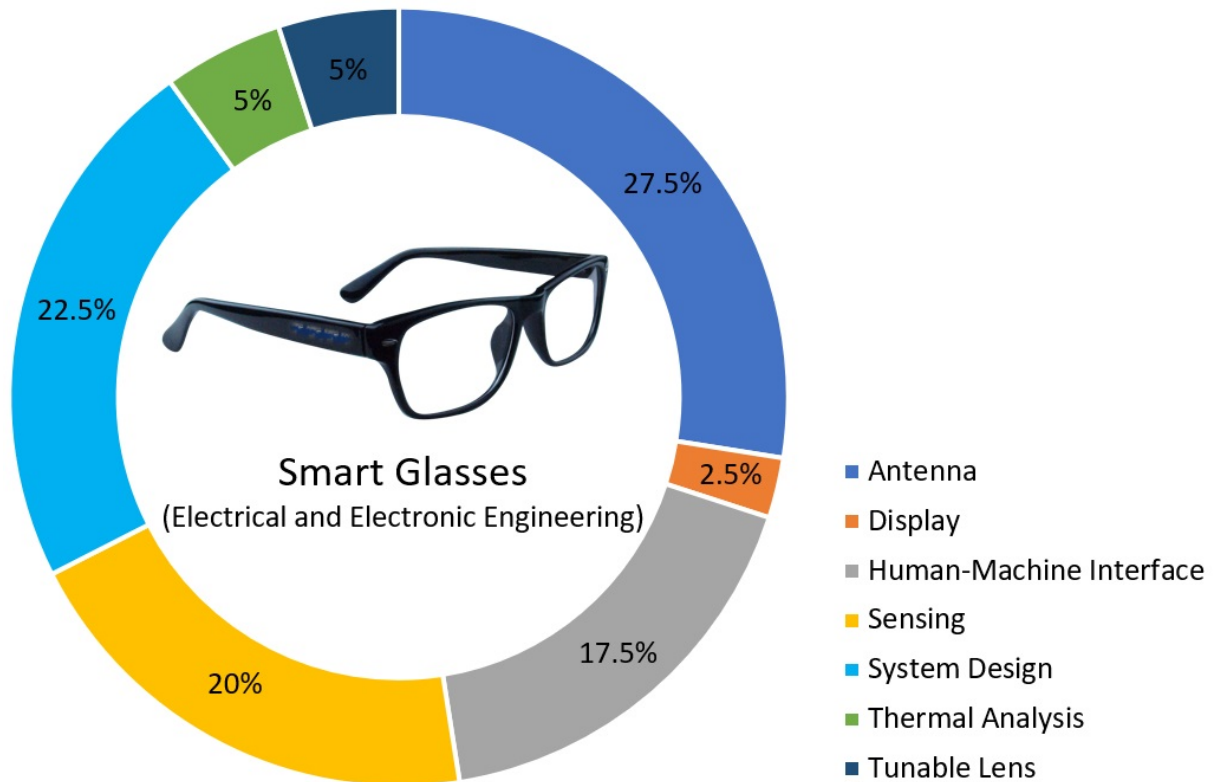
Figure 1.10: Previous research papers can be divided into 7 categories, including antenna, display, HMI, sensing, system design, thermal analysis and tunable lenses.

In 2005, Jeong *et al.* published a paper regarding using antenna in smart glasses for energy harvesting. In the paper, they developed a multi-functional RF integrated passive device, which can be integrated into wearable applications [75]. In 2018, Hong *et al.* proposed a 60 GHz patch antenna array for smart glasses. The resonant frequency of the antenna array is in the millimetre wave range, which can be applied to the next generation of wearable applications and enable high communication speed [76]. Apart from that, Chung *et al.* proposed a 6×6 Multiple Input Multiple Output (MIMO) antenna system for for WiFi 6E and WiFi 7 indoor wireless communication. MIMO systems take advantage of multipath propagation, where signals can take different paths to reach the receiver, by transmitting multiple data streams simultaneously. This antenna system can be used to connect smart glasses to the IoT network [77]. Previously introduced papers have all integrated antennas on the glass frame. However, Cil *et al.* proposed an antenna mounted on the glasses lens.

In their paper, the researchers designed and printed a reconfigurable slot antenna on a glass lens, where the slot could be controlled via switches to operate in two different modes [78]. Due to a large focus on antenna design, I have explored how an antenna can be made tunable using LCs in Chapter 5.

1.4.3.2 Display

After adding restrictions to the search scope, there is only one paper related to display technology applications. However, it does not mean the lack of research in this field. The majority of display technology-related publications are categorized as optical engineering rather than electrical and electronics engineering.

In 2018, Takuji *et al.* proposed a novel production process of a holographic waveguide combiner, which could integrate holographic optical elements onto a plastic substrate [79]. The holographic waveguide combiner enables the projection of digital images or information into the wearer's FOV. The researchers developed a roll-to-roll production process which accurately integrated the holographic optical elements into plastic waveguides, which could be used for AR applications.

1.4.3.3 Human-Machine Interface

According to the survey, 17.5% of the publications are related to HMI. There are different types of interfaces that can be integrated into smart glasses, including head movement, hand gesture and eye movement. Noticeably, most of the publications in the HMI category involve sensor integration. However, I classified them under the HMI category since their novelty lies in proposing an innovative interface for human-machine interaction.

For example, Chui *et al.* developed automatic segmentation and extraction glasses, which can interact with glasses users by processing image data in real-time [80]. They intended to develop an algorithm to enhance HMI using video, which can automatically transform the image data into coherent segments and assess the importance of each segment. In addition, Wang *et al.* introduces a novel head movement capture system called Air Mouse. This system utilized a gyroscope and was able to measure head movement in real-time, which is a hand-free interaction method and enhances human-computer interaction [81]. This design provides flexibility to users to remote control devices which are not directly accessible. The interface is low-cost, accurate, easy to use and provides interaction in real-time. Moreover, Li *et al.* developed a touch sensor to capture hand gesture input, where the user can draw different patterns on the touchpad to interact with the smart glasses [82]. This interface enables participants to enter their passwords quickly and accurately in a variety of situations.

1.4.3.4   Sensing

There are one fifth of publications related to sensing technologies, including sensor design, integration or design of sensing systems. Generally, the sensing system on smart glasses could divided into three different categories, which are gaze sensor, motion sensor and physiological signal sensor.

For the gaze sensor, Hong *et al.* proposed an object recognition system, which could be activated by gaze [83]. In the system, a gaze image sensor was employed, which utilized a pupil edge detection algorithm and consumed minimal energy. After gaze coordinates were calculated, it was mapped with images captured by the front camera to make predictions regarding the user's point of focus. This design can facilitate human-machine interaction

for futuristic head-mounted devices (HMDs). In addition to that, Meyer *et al.* proposed a static laser feedback interferometry-based gaze sensor. Compared with traditional video-based gaze tracking systems, their system has a high update rate, integrateability, slippage robustness, and low power consumption [84, 85].

Hellec *et al.* integrated an inertial measurement unit (IMU) in smart glasses to measure the acceleration of sit-to-stand movements [86]. This design could be applied to the elderly to detect falls. Archer *et al.* proposed a facial expressions detector using an optomyographic sensor network [87]. Motion sensors were placed at different positions of the eye-glass frame and could measure skin movement in three dimensions. Combining the measurement data from the sensor array, the smart glasses can then monitor facial expressions in real-time.

Physiological signal sensors on smart glasses can be used to monitor health and behavior. An emotion detector was proposed by Kwon *et al.* using electrodermal activity and photoplethysmogram sensor [88]. The sensor data were then processed by an emotion recognition algorithm, which demonstrated better accuracy than an image-based emotion detector. Moreover, Doniec *et al.* designed electrooculography (EOG) sensor-based smart glasses to identify road conditions [89]. Based on EOG, acceleration and angular velocity sensor data from the driver, the smart glasses were able to identify four different road types, including the city road, highway, housing estate and undeveloped area.

1.4.3.5 System Design

Moreover, approximately 22.5% of publications proposed a comprehensive system design, involving hardware and software to serve a specific purpose. In this subsection, I will introduce them based on the applications of their respective designs. AR technology has been widely used in smart glasses systems for different applications. To start with, Ahmed proposed a vehicle parking management system using Google Lens [90]. This research

focused on setting up a web service that enables users to scan number plates and assists in analyzing parking situations. Spandonidis *et al.* also utilized AR-based glasses for vision-impaired elderly workers [91]. They indicated that AR glasses could enhance users' vision and improve work performance for those who suffer from visual impairments. Xia *et al.* proposed a smart glasses system using AR technology to display information from multimeter [92]. This work could benefit workers and prevent them from getting distracted when reading data from a multimeter. Furthermore, Runji *et al.* designed an AR glasses system for PCB assembly manufacturing and inspection [93].

Apart from AR-related smart glasses systems, there are a few smart glasses systems that integrate sensors to facilitate HMI. Chang *et al.* integrated a drowsiness fatigue detection system into smart glasses to enhance road safety [94]. This system involved an IR sensor which could detect whether the eyes are open or closed. Based on the eye closed period, the smart glasses could identify if the driver is fatigued. Moreover, this research team also designed a drug pill recognition system using machine learning for visually impaired patients [95]. Bai *et al.* designed smart guiding glasses for visually impaired people in indoor environments [96]. These glasses involved a depth camera and ultrasonic sensor to capture depth images and measure distance. The image and sensor data would be processed via an embedded CPU board. Subsequently, the processed data will be transmitted to the user via AR glasses with a rendered image or through a notice sound from the earphones. A similar design is proposed by Busaeed *et al.* [97]. Moreover, Mukhiddinov *et al.* designed a smart glass system for blind and visually impaired people [98]. Apart from the camera and ultrasonic sensor, a GPS sensor was also integrated into the system to provide position information to the user.

1.4.3.6 Thermal Analysis

According to the survey, two publications are related to thermal analysis for smart glasses. Smart glasses typically incorporate electronic components that generate heat. Monitoring the temperature can help prevent overheating and potential damage. Matsuhashi *et al.* proposed a thermal model and countermeasures for smart glasses in the future [99]. Their model significantly reduced temperatures in the area near the ear that touches the skin by distributing heat sources, placing components strategically, and using specific materials. Kusumi *et al.* introduced a novel approach for optimizing the placement of electronic components in smart glasses to mitigate heat-related issues [100]. Experimental results demonstrate the effectiveness of this method in reducing maximum temperatures in these areas.

1.4.3.7 Tunable Lenses

Lastly, there are two publications about smart tunable lenses for vision assistance. Han designed an IR sensor-synchronized active shutter glasses for 3D HDTV. The smart glasses involve microcontroller units and drivers, which could deliver excellent 3D image viewing performance. Ihmig *et al.* developed and assessed electronic glasses frames for smart LC shutter glasses designed to monitor wearing and occlusion times in children with amblyopia. They refined the electronic glasses frames, tested them on seven healthy children, and evaluated their precision in wearing position detection, activity recognition and occlusion pattern execution. The results demonstrated the successful implementation of adaptive shutter operation and real-time therapy monitoring algorithms, with high accuracy in detecting wearing positions, recognizing activities, and halting occlusion when active motion was detected.

1.5 Summary

1.5.1 Challenges of Smart Contact Lenses

Despite the previously mentioned benefits of smart contact lenses for HMI applications, there are still many challenges. For example, the driving voltages required to power the various electronic modules are still large (> 1 V). Therefore, since power consumption is high, such smart electronic platforms may be unsafe for the eye. Although the advancements in transistor nanofabrication led to a steady reduction in power supply voltage from 1.2 V in 2003 to 0.5 V in 2018 [101, 102], integrating advanced chips into smart glasses may lead to elevated production costs.

Moreover, since contact lenses are regarded as temporary prostheses, regulatory approval is essential before they can be used. For example, the U.S. Food and Drug Agency (FDA) oversees the safety, effectiveness and manufacturing of contact lenses. Such a process has been criticised as expensive and costly [103], which may hinder the introduction of smart contact lenses on a large scale, especially if examination, trialling and practical training by an ophthalmologist is necessary.

Nevertheless, another grand challenge facing smart contact lenses that needs research involves protecting the wearer's sensitive, personal information from data breaches and preventing unauthorised access to confidential information. Convincing users to adopt smart contact lenses, especially for continuous health monitoring, requires addressing privacy concerns. Due to the pervasiveness of mobile phones and the rapid development of Body Sensor Networks (BSN) [68], secure wireless communication between the contact lens system and other peripheral devices is, therefore, urgently needed.

Additionally, integrating electronic systems into a contact lens is another significant challenge. In my previous review, I noticed that most of the publications only focused on developing prototypes of smart contact lenses, which did not take user comfort and vision blockage into consideration. Therefore, I reckoned for a long period that smart contact lenses would remain confined to laboratory research.

1.5.2 Conclusions

In this chapter, I reviewed previous research on smart contact lenses and smart glasses areas. Contact lenses and glasses have traditionally been used for vision correction applications. Recent advances in microelectronics and nanofabrication have now enabled sensors, circuits and other essential components to be integrated into a contact lens platform and glasses frame. This has opened up the possibility of using contact lenses and glasses for a range of human-machine interaction applications including vision assistance, eye tracking, displays and health care. In this chapter, I systematically review the range of smart contact lenses and smart glasses, including materials, device architectures and components that facilitate this interaction for different applications. I classified the literature on smart contact lenses and smart glasses into different building blocks and analyzed recent developments in each of these categories. Both contact lenses and smart glasses play an essential role in facilitating the interaction between humans and machines.

Additionally, I speculated on the challenges of smart contact lenses for human-machine interaction based on my survey. Contact lenses have evolved from vision correction platforms to advanced tools for healthcare, entertainment as well as safety and security applications. However, as mentioned previously, the challenges of smart contact lenses are substantial, including limited power source, safety and biocompatibility. On the other hand, smart glasses are more well-developed industrial products. For example, smart glasses enable higher operation voltage and more complicated electronic systems. Due to the limita-

tion of smart contact lenses, my research will focus on facilitating HMI via the smart glasses platform. Specifically, according to the survey, I noticed that both smart contact lenses and smart glasses fields have publications regarding using LC material for vision assistance.

Consequently, the thesis will focus on the integration of LC materials into smart glasses to facilitate HMI. My research involves answering the following question: 'Can LCs be used in a wearable application to facilitate HMI using our eyes?'. To answer this question, my thesis has explored a number of possibilities that are presented in the chapter of the thesis. Having presented the background and motivation, my thesis is organized as follows:

- Chapter 2: Introduction of the LC materials, including their properties, modelling methods and applications.
- Chapter 3: Introduction of materials related to LC cell fabrication, including electrode materials, alignment materials and spacer materials.
- Chapter 4: A method to deposit transparent electrodes on patterned surfaces, which will benefit the next generation of optical devices.
- Chapter 5: Proposing a tunable antenna on smart glasses for 5G applications, which used LCs as substrate material.
- Chapter 6: Demonstration of tunable optical combiner for AR glasses using CLC materials.
- Chapter 7: Demonstration of tunable color filter glasses for epilepsy treatment using CLC materials.
- Chapter 8: Conclusion and future outlook.

Chapter 2

Introduction to Liquid Crystals

2.1 Physical Properties

In addition to the solid, liquid and gas states, the LC state is termed the fourth state of matter, which was first discovered by the botanist F. Reinitzer in 1888 [104]. LCs are a soft state of matter that exhibit flow properties similar to liquids yet the molecules maintain weak positional and orientational ordering, which allows them to have physical properties that are similar to solids. In fact, the LC phase sustains a molecular orientation ordering that lies between the random (long-range) molecular ordering of the liquid phase and the high (short-range) molecular ordering of the solid phase. LC molecules have rod-like or disk-like structures, whose behavior can be controlled by temperature, magnetic field and electric fields [70].

LCs can be classified into two main types, thermotropic LCs and lyotropic LCs. Thermotropic LCs are most commonly used in display and photonics devices, while lyotropic LCs are mainly used in the biology field [105]. Therefore, my thesis will focus on thermotropic LCs. Thermotropic LCs are in LC phase only in a certain range of temperature. In this chapter, I will mainly introduce Thermotropic LCs. Generally, if the temperature of the LC material is below its melt point, it is in solid state and exhibits crystal properties.

When the temperature is raised above the melting point and between the clear point, the material is in LC phase, which is cloudy and can flow like liquid. If the temperature is increased above the clear point, the LC material will turn into a clear liquid. LC materials in crystalline phase, LC phase and isotropic phase are shown in Fig. 2.1.
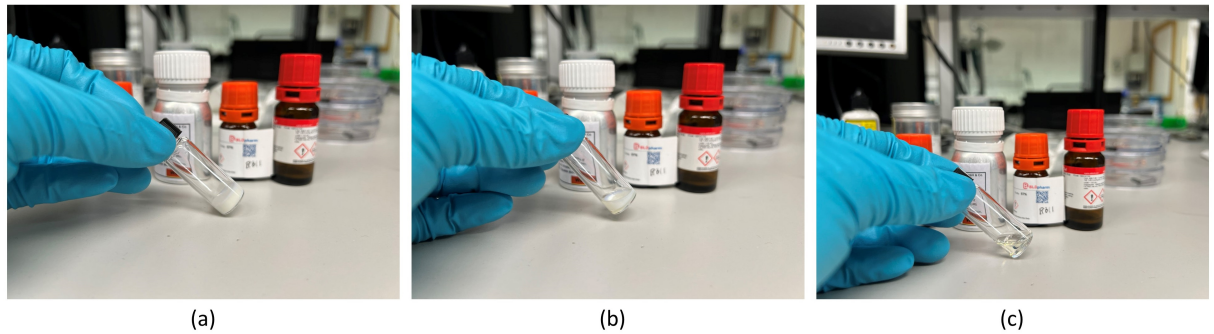
Figure 2.1: (a) LC materials in the crystalline phase. (b) LC materials in the LC phase. (c) LC materials in the isotropic phase.

Anisotropy is one of the most important properties of LCs. To be specific, the properties of LCs are directionally dependent, including optical, electrical and mechanical properties. For rod-like LC molecules, parameters such as refractive index n and dielectric permittivity ε are different parallel and perpendicular to the long axis of the molecule. Orientational order is another important feature of LCs [106]. LC molecules tend to align themselves along a specific axis or direction within the material, which results in anisotropy throughout the LC cell. The orientational ordering of the molecules is defined as director, which represents the ensemble average direction of LC molecular orientation. This orientation is a fundamental characteristic of LCs and can be varied via external conditions applied, for example, electric field, magnetic field and temperature. The most common way to manipulate LCs is by electric field. LCs are highly sensitive to electrical fields, and their molecular orientation can be controlled via varying electric field strength and direction, which is the basis for LCD applications.

The anchoring effect appears at the boundary of LC and substrate, where the surface profile of an alignment layer can determine the orientation of LC molecules. Specifically, an alignment layer is applied to define the orientation of LCs. There are types of anchoring effects, which are planar and homeotropic alignment. For planar alignment, the

LC molecules at the substrate interface tend to align parallel to the surface of the substrate. This type of anchoring is commonly used in many LCDs. Planar anchoring can be achieved by alignment layers that promote a parallel orientation. For example, rubbing polymer material in one direction with cloth could result in planar alignment [107]. For homeotropic alignment, the LC molecules are aligned perpendicular to the substrate surface. This is achieved by an alignment layer that forces the LC molecules to point away from the substrate, for example, lecithin [108]. Homeotropic alignment is used in some LCDs and other optical devices, such as beam steering devices.
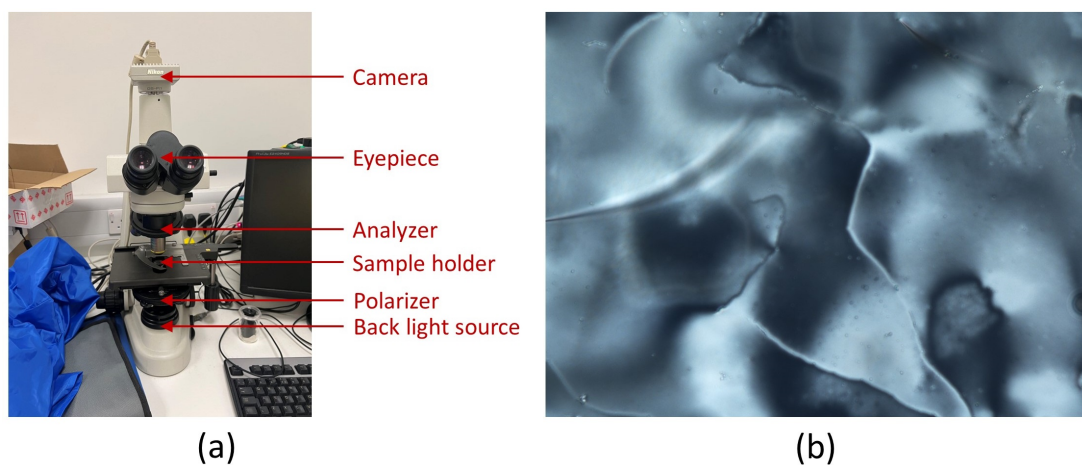
Figure 2.2: (a) Microscope setup used to observe and characterize nematic liquid crystal (NLC) materials. (b) The image of an unaligned NLC sample (5CB, 50 μm). This image was captured using a transmission cross-polarization microscope.

2.2 Common Thermotropic Nematic Liquid Crystal Materials

LCs are made of organic molecules. Cyanobiphenyl LCs were the first type of stable LC material discovered at Hull University [109, 110]. Subsequently, a class of LC compounds consisting of biphenyl molecules that have one or more cyano groups attached to them are discovered by researchers, for example, 4-Cyano-4'-pentylbiphenyl (5CB), as shown in Fig. 2.3. These LC compounds are widely applied in the display field. In addition, some

different types of LC materials are discovered, such as 4 -(Octyloxy)-4-biphenylcarbonitrile (8OCB) and 4-Cyano-4´-n-pentyl-p-terphenyl (5CT). Compared with 8CB, 8OCB has an extra oxygen atom. 5CT has an extra phenyl compared with the molecular formula of 5CB.

$$CH_3(CH_2)_3CH_2 - \bigcirc - \bigcirc - CN \qquad 5CB$$
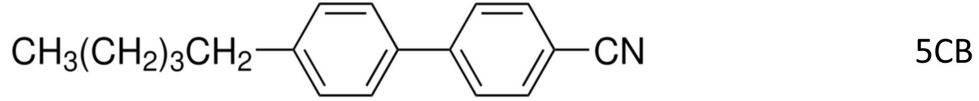
Figure 2.3: 5CB LC material, which is a commonly used material in LCD applications.

Different LC compounds demonstrate different properties, including phase transition temperature, reflect index, dielectric permittivity and viscosity. Therefore, researchers explored in LC mixture to optimize the performance for different applications. For example, E7 is a specific mixture of LC compounds with a nematic phase, which consists of a mixture of various LC compounds, including 5CB, 7CB, 8OCB and 5CT. Compared with other pure substances of LC material, E7 demonstrates significant stability at different temperatures. It exhibit in LC phase from -55°C to 60 °C [111], where 5CB is in LC phase from 22.5 °C to 35 °C [112]. Therefore, E7 is used in various optical and electro-optical devices, including LCDs, optical switches and LC filters.

Previously introduced NLC materials are oriented in a particular direction but with no long-range positional order, thus they have uniform optical properties. By introducing chirality to NLC material, chiral nematic LC material can be obtained, which is also known as CLC. CLC is in the nematic phase, but the average direction of the molecules varies periodically through the material, as is shown in Fig. 2.4. The common way to introduce chirality of NLC material is via chiral dopant, for example, (S)-2-Octyl 4-[4-(Hexyloxy)benzoyloxy]benzoate (S811) and 4-(trans-4-pentylcyclohexyl)-1,1'-[(1(S)(+))-1-phenyl-1,2-ethanediyl] ester (S1011). S811 is a white powder at room temperature. Chiral dopant could be mixed with NLC material by heating to its melt point. Different chiral dopants have different capabilities of twisting NLC materials, which could be represented as helical twisting power (HTP). For example, the HTP of S811 and S1011 is around 11.1 and 33, respectively [113, 114]. Additionally, different chiral dopants could

introduce different chirality. For example, S811 is a left-handed chiral dopant, and (R)-2-Octyl 4-[4-(Hexyloxy)benzoyloxy]benzoate (R811) is a right-handed chiral dopant. These two chiral dopants have the same molecular formula but are able to introduce different handedness to NLC materials.
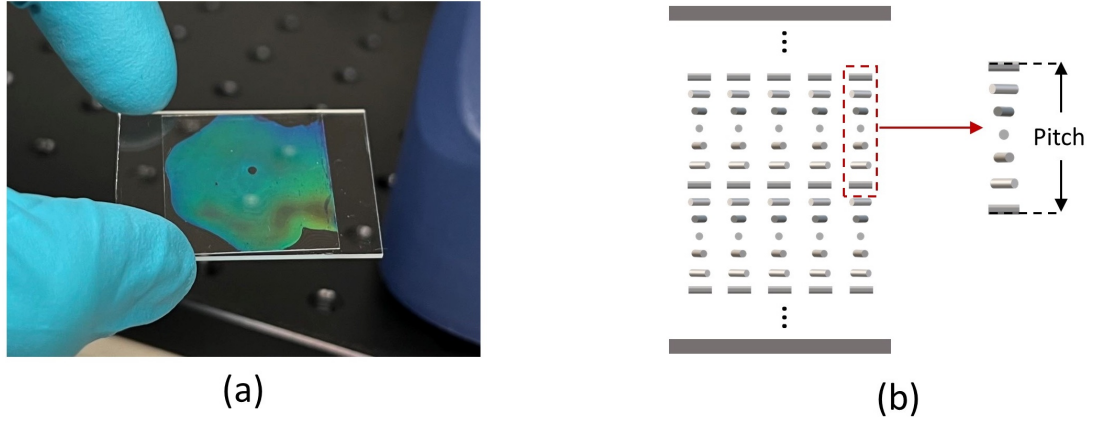
Figure 2.4: (a) A CLC cell that exhibits selective reflection. (b) The helical molecular structure inside the cell.

A CLC cell could be divided into multiple layers, where the directors orientation varies with layers. The variation of director orientation is periodic, where pitch length 'P' represents the distance of directors rotating 360 degrees on the perpendicular axis, as is shown in Fig. 2.4 [104]. The pitch length could be determined by various factors, including the temperature and concentration of the chiral dopant [115], as is demonstrated in Fig.2.5. The helical structure of CLC material throughout the cell results in its special properties, including selective reflection, optical rotation and circular dichroism [116]. Selective reflection means CLC materials can reflect certain wavelengths of light based on their physical properties, which is also called Bragg reflection [117]. The selective reflect wavelength of a CLC cell is determined by pitch length. Specifically, when incident light interacts with the helical structure of CLC material, some light waves that align with the pitch of the helix exhibit constructive interference, which is reflected back in a distinct direction.
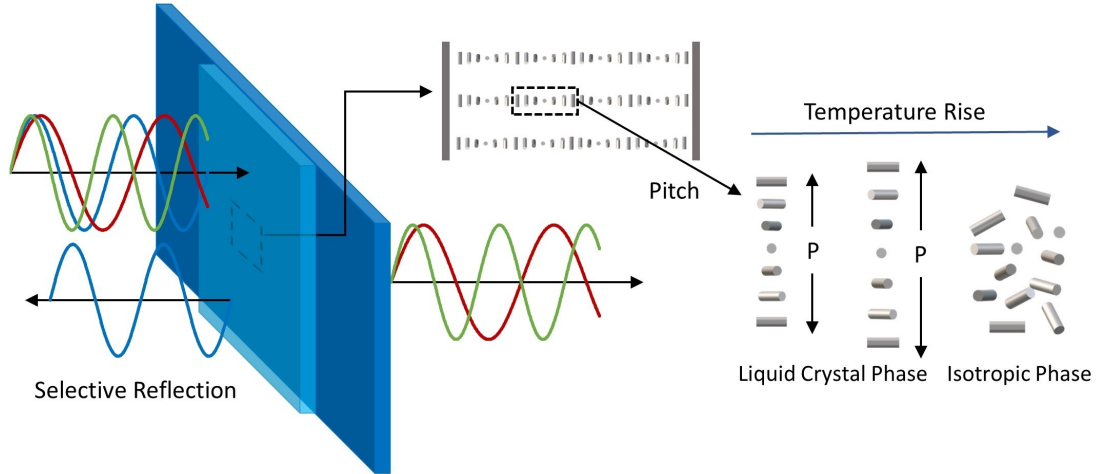
Figure 2.5: The figure demonstrates the selective reflection property of CLC material and illustrates how the pitch length and phase of LC material can be influenced by temperature variations.

2.3 Mathematical Modeling

The behavior of LCs under electric field can be simulated using mathematical models. There are two common modelling techniques for LCs, which are the Landau de Genes **Q**-tensor theory [118] and Oseen-Frank theory [119]. There has been extensive research on both methods [120, 121]. Thanks to advancements in nanotechnology and micro-fabrication, the shrinking size of electrodes that drive these LC devices are bound to induce defects that are caused by strong fringing electric fields, as shown from Fig. 2.6 [70]. These defects are therefore becoming more important in such sub-wavelength devices. Therefore, my thesis focuses on the use of **Q**-tensor theory due to the presence of defects or disclinations [122, 123, 120].

As previously mentioned, LC molecular shape anisotropy results in orientational, and sometimes positional, order, which then translates into a bulk phase anisotropy. These anisotropic properties allow LCs to be manipulated through a balance of forces and torques due to an applied electric field and elastic effects. The orientation of the NLC director can be altered through a balance of effects due to an applied electric (or magnetic) field and internal elasticity. The director configuration that minimises the total free energy, which
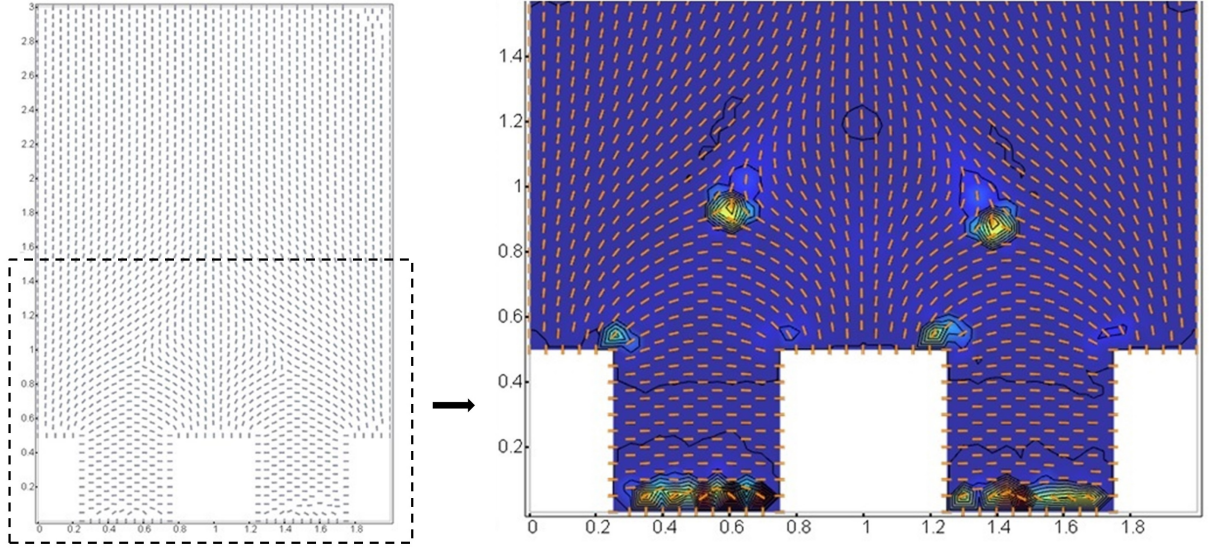
Figure 2.6: Director profile for NLC cell with homeotropic alignment, where the voltage of adjacent electrodes are 5 and -5 V, respectively. All dimensions are in micrometers.

comprises of electrostatic and elastic components, will be the one observed and can be tuned by varying the applied voltage. These two effects are mathematically formulated through the electrostatic energy density F_{es}, which depends on the anisotropic dielectric properties of the material described in terms of a rank-2 dielectric permittivity tensor $\boldsymbol{\epsilon}$, and the bulk nematic energy density which consists of an elastic component F_{el} and a thermotropic component F_{th}. Once the director profile that minimizes the free energy is determined, the optical phase profile of the LC material may then be calculated.

Although the free energy density components may be written in terms of the director, $\mathbf{n(x)}$, problems occur in such a model when high gradients of $\mathbf{n(x)}$ are present, for instance near electrode edges. I therefore use the Landau de Gennes (LdG) model of a NLC, whereby the alignment of the molecules in the LC state is described in terms of both a degree of orientational order, $S(\mathbf{x})$, and the preferred direction of orientation, $\mathbf{n(x)}$. Each free-energy component is then written in terms of the '$\mathbf{Q}$-tensor', a rank-2 tensor, which takes the form:

$$\mathbf{Q} = S\left(\mathbf{n} \otimes \mathbf{n} \frac{\mathbf{I}}{3}\right), \qquad (2.1)$$

36

Where $\mathbf{I}$ is the identity matrix. The total free energy $(\mathscr{F})$ of the NLC can be written as the volume integral of the sum of the elastic (F_{el}), thermotropic (F_{th}) and electrostatic energy (F_{es}) density functions:

$$\mathscr{F} = \int_V (F_{el} + F_{th} + F_{es}) \, dV. \tag{2.2}$$

The application of an electric field to a NLC induces dipoles, which may be caused by induced molecular dipoles and/or reorientation of enhanced existing molecular dipoles, which causes the director to align either parallel or perpendicular to the electric field, depending on the largest dielectric permittivity of the material. The preference for parallel or perpendicular alignment with an applied electric field is therefore determined by the dielectric anisotropy, $\Delta\varepsilon = \varepsilon_{\parallel} - \varepsilon_{\perp}$, the difference in permittivities parallel and perpendicular to the molecular axis [124]. The dielectric displacement field due to these dielectric effects is then:

$$\mathbf{D} = \varepsilon_0 \epsilon \mathbf{E}, \tag{2.3}$$

Where ε_0 is the permittivity of free space and ϵ is the dielectric permittivity tensor, which can be expressed in terms of the $\mathbf{Q}$-tensor as [125]:

$$\epsilon = \frac{\Delta\varepsilon}{S_{eq}} \mathbf{Q} + \tilde{\varepsilon} \mathbf{I}, \tag{2.4}$$

and where $\tilde{\varepsilon} = (2\varepsilon_{\perp} + \varepsilon_{\parallel})/3$ is the average permittivity and S_{eq} is the order parameter in the bulk of the LC at which the experimental measurement of $\Delta\varepsilon$ was undertaken. The resulting electrostatic energy density of the NLC is:

$$F_{es} = -\frac{1}{2}\mathbf{D}.\mathbf{E} = -\frac{1}{2}\varepsilon_0(\epsilon\mathbf{E}).\mathbf{E} = -\frac{1}{2}\varepsilon_0\epsilon\nabla U.\nabla U, \tag{2.5}$$

Where U is the electric potential and $\mathbf{E} = \nabla U$.

Using the commonly assumed one-constant approximation for the elastic constants of the NLC [120], the elastic energy density and thermotropic energy density may be written as:

$$F_{el} = \frac{L}{2}|\nabla \mathbf{Q}|^2 \qquad \text{and} \qquad F_{th} = A\text{tr}(\mathbf{Q}^2) + \frac{2B}{3}\text{tr}(\mathbf{Q}^3) + \frac{C}{2}\text{tr}\left(\mathbf{Q}^4\right), \qquad (2.6)$$

Where L is an average elastic constant related to the splay bend and twist constants K_{11}, K_{22} and K_{33}, tr(.) signifies the trace of a tensor, $A = a(TT^*) = a\Delta T$ is a temperature-dependent coefficient, with $a > 0$ and T^* the temperature at which the isotropic state $\mathbf{Q} = 0$ becomes unstable, and B and C are assumed to be temperature independent. In the simulations below, these coefficients were set to $A = 6.5 \times 10^5 Nm^{-2}$, $B = 16 \times 10^5 Nm^2$ and $C = 39 \times 10^5 Nm^2$ [120].

The total free energy density is therefore written as:

$$\mathscr{F} = \int_V \frac{L}{2}|\nabla \mathbf{Q}|^2 + A\text{tr}(\mathbf{Q}^2) + \frac{2B}{3}\text{tr}(\mathbf{Q}^3) + \frac{C}{2}\text{tr}\left(\mathbf{Q}\right)^4 \frac{1}{2}\varepsilon_0\varepsilon\nabla U.\nabla U \ dV. \qquad (2.7)$$

The equilibrium director configuration can be obtained by minimizing the total free energy in eq. 2.7 using the calculus of variations, which leads to the partial differential equations for the minimizing $\mathbf{Q}$-tensor components,

$$\left(\frac{\partial F_b}{\partial Q_{i,j}}\right)_{,j} = \frac{\partial F_b}{\partial Q_i}, \qquad (2.8)$$

where the $_{,j}$ subscript denotes partial differentiation with respect to the $\mathbf{j}^{\text{th}}$ component of the position vector, which in the present 2-dimensional setting is $\mathbf{x} = (x,z)$, and the summation convention has been used. Together with the equation for the components of the $\mathbf{Q}$-tensor, Gauss's law for the electric potential must be simultaneously solved,

$$0 = \nabla.\mathbf{D} = \nabla.(\varepsilon_0(\epsilon\mathbf{E})) = -\varepsilon_0\nabla.((\epsilon\nabla U)) = -\varepsilon_0\left(\varepsilon_{ij}U_{,j}\right)_{,i}. \qquad (2.9)$$

2.4 Light Progression Modelling

2.4.1 Jones 2×2 matrix method

Light propagation inside LC cell can be simulated using mathematics models. If the interaction inside the material can be neglected, the Jones 2×2 matrix method can be used to calculate the propagation of an electromagnetic wave through a LC cell [104, 126]. In the Jones method, assuming light propagation is on z direction, the incident light is represented by components of electromagnetic wave on x and y axis, where

$$\mathbf{E} = \begin{bmatrix} E_x \\ E_y \end{bmatrix} \tag{2.10}$$

As mentioned previously, due to the anisotropy of LC material, the refractive index parallel and perpendicular to the long axis is different, which could be represented by n_o and n_e, respectively. When light passes through an LC cell, the director of the LC molecules can affect the phase of light. Assume light speed in vacuum is c, then light propagation speed on different axes is c/n_o and c/n_e, respectively. Normally, n_o is smaller than n_e, thus light propagation speed parallel to the long axis is larger than the light speed perpendicular to the long axis. The difference in light progression speed results in phase variation. According to the Jones method, the output light can be represented by:

$$\mathbf{E_o} = \begin{bmatrix} E_{xo} \\ E_{yo} \end{bmatrix} = e^{-i[\pi(n_e+n_o)h/\lambda]} \begin{bmatrix} e^{-i\Gamma/2} & 0 \\ 0 & e^{i\Gamma/2} \end{bmatrix} \begin{bmatrix} E_{xi} \\ E_{yi} \end{bmatrix} \tag{2.11}$$

Where $\Gamma = 2\pi(n_e - n_o)h/\lambda$ represents phase retardation. h is the thickness of cell and λ is the wavelength in vacuum. $e^{-i[\pi(n_e+n_o)h/\lambda]}$ is a phase factor which could be neglected since it is only related to the absolute phase. Therefore, the Jones 2×2 matrix is defined as:

$$\mathbf{G}(\Gamma) = \begin{bmatrix} e^{-i\Gamma/2} & 0 \\ 0 & e^{i\Gamma/2} \end{bmatrix} \tag{2.12}$$

However, the optical axis of LC layer is not always aligned with the defined x and y axis, which can be represented by the component on x and y axis. Assuming the optical axis has an angle β with the x axis in the plane, the incident light and output light could be then converted as:

$$\mathbf{E_i}' = \begin{bmatrix} E'_{xi} \\ E'_{yi} \end{bmatrix} = \begin{bmatrix} cos\beta & sin\beta \\ -sin\beta & cos\beta \end{bmatrix} \begin{bmatrix} E_{xi} \\ E_{yi} \end{bmatrix} \tag{2.13}$$

$$\mathbf{E_o}' = \begin{bmatrix} E'_{xo} \\ E'_{yo} \end{bmatrix} = \mathbf{G}(\Gamma)\mathbf{E_i}' \tag{2.14}$$

Then the equation describing the outgoing light can be expressed as:

$$\mathbf{E_o} = \begin{bmatrix} E'_{xo} \\ E'_{yo} \end{bmatrix} \begin{bmatrix} cos\beta & -sin\beta \\ sin\beta & cos\beta \end{bmatrix} \quad (2.15)$$

$$= \begin{bmatrix} cos^2\beta e^{-i\Gamma/2} + sin^2\beta e^{i\Gamma/2} & sin\beta cos\beta (e^{-i\Gamma/2} - e^{i\Gamma/2}) \\ sin\beta cos\beta (e^{-i\Gamma/2} - e^{i\Gamma/2}) & sin^2\beta e^{-i\Gamma/2} + cos^2\beta e^{i\Gamma/2} \end{bmatrix} \mathbf{E_i} \quad (2.16)$$

If the LC directors are not uniformly aligned, the Jones 2×2 method can still be used to calculate the transmission of light. For non-uniform birefringent film, it can be regarded as a stack of sublayers. Thus, the outgoing light of the previous sublayer can be used as the incident light of the next sublayer. The overall transmittance could be calculated by:

$$\mathbf{E_o} = \prod_{i=1}^{N} [\mathbf{R}(\beta_i)\mathbf{G}(\Gamma_i)\mathbf{R}^{-1}(\beta_i)]\mathbf{E_i} \quad (2.17)$$

Jones matrix method is commonly used in optic simulation light propagation in LC cells. However, there is also a limitation of this method. This method is only suitable for normal incident light, which neglects reflection inside the LC cell. Despite the extended Jones matrix has taken reflection and refraction between layers into consideration [127]. However, multiple reflections still cannot be simulated, which restrict it from being used to simulate LC cells with complex molecular alignment, such as CLC cell.

2.4.2 Berreman 4×4 matrix method

To address the limitation of the Jones 2×2 matrix method, which cannot simulate reflection and refraction between layers, the Berreman 4×4 matrix method was developed to solve the propagation of plane waves in anisotropic layers based on articles from Berreman and Schubert [128]. In the Berreman 4×4 method, the CLC layer is divided into multiple layers, which consider factors like reflection, transmission, and phase changes that occur at each interface between different layers. The propagation of the light waves in CLC sample could be represented by Maxwell's equation [104, 115]:

$$\nabla \cdot \mathbf{D} = 0 \tag{2.18}$$

$$\nabla \cdot \mathbf{B} = 0 \tag{2.19}$$

$$\nabla \times \mathbf{E} = -\frac{\partial \mathbf{B}}{\partial t} = ik_0 \mathbf{H} \tag{2.20}$$

$$\nabla \times \mathbf{H} = \frac{\partial \mathbf{D}}{\partial t} = -ik_0 \varepsilon \mathbf{E} \tag{2.21}$$

Assuming light wave propagation is on z axis, Maxwell's equations result in a propagation equation with the transverse components (E_x, E_y, H_x, H_y). After that, the propagation of the electromagnetic waves in the isotropic media could be calculated via the equation:

$$\frac{\partial \Phi}{\partial t} = -ik_0 \mathscr{D} \Phi(z) \tag{2.22}$$

Where $\mathscr{D}$ is the Berreman 4×4 matrix:

$$
\mathscr{D} =
\begin{bmatrix}
-\eta\dfrac{\varepsilon_{31}}{\varepsilon_{33}} & 1-\dfrac{\eta^2}{\varepsilon_{33}} & -\eta\dfrac{\varepsilon_{32}}{\varepsilon_{33}} & 0 \\[2ex]
\varepsilon_{11}-\dfrac{\varepsilon_{13}\varepsilon_{31}}{\varepsilon_{33}} & -\eta\dfrac{\varepsilon_{13}}{\varepsilon_{33}} & \varepsilon_{12}-\dfrac{\varepsilon_{13}\varepsilon_{32}}{\varepsilon_{33}} & 0 \\[2ex]
0 & 0 & 0 & 1 \\[2ex]
\varepsilon_{21}-\dfrac{\varepsilon_{23}\varepsilon_{31}}{\varepsilon_{33}} & -\eta\dfrac{\varepsilon_{23}}{\varepsilon_{33}} & \varepsilon_{22}-\dfrac{\varepsilon_{23}\varepsilon_{32}}{\varepsilon_{33}}-\eta^2 & 0
\end{bmatrix},
\tag{2.23}
$$

The component of the incident light $\eta = k_x/k_0$ is constant throughout the sample. Subsequently, the output light wave of a single layer could be calculated by integration equation 5 along the z axis, as shown below:

$$
\Phi(z+\triangle z) = e^{-ik_0\mathscr{D}(z)\triangle z}\Phi(z)
\tag{2.24}
$$

Therefore, since the CLC layer is divided into multiple thin films, the overall transmittance of the light wave can be calculated by:

$$
\Phi_t = \prod_{i=1}^{N}\Phi(\triangle z_i)
\tag{2.25}
$$

To prevent photosensitive epilepsy, 660 to 720 nm wavelengths of light need to be filtered by the glasses. Therefore, the transmittance of a CLC cell with a central wavelength of 690 nm is simulated, and the result is demonstrated in the result section.

2.5 Applications of Liquid Crystals

LCs have a wide range of applications in various fields, including display, sensing, reconfigurable optical devices and biomedical applications. The most common application of NLCs is LCDs. According to Section 1.4, due to the anisotropy of LC material, electromagnetic wave propagation at different directions have different speed, which results in phase retardation. For traditional twisted nematic (TN) display, polarizer and analyzer are placed on the top and bottom of the LCD stack, whose polarization directions are perpendicular to each other [129]. There are two alignment layers on each side of the cell, which are also perpendicular to each other. In this case, the LC molecules are twisted throughout the cell, which results in the polarization of incident light to rotate as it passes through the LC layer. The rotation angle of the polarized incident light is 90°. Therefore, when no voltage is applied to the LC cell, the LC molecules maintain their helical structure, and the polarized light passing through them experiences a twist. Since the analyzer and polarizer are perpendicular to each other, the polarized incident light could then pass the analyzer, thus the LC cell can be regarded as 'ON'. When there is a voltage across the LC layer, the molecules can be aligned with the electric field, straightening out the twist. In this case, the phase retardation is eliminated and the polarized incident light will be blocked by the analyzer, thus the LC cell can be regarded as 'OFF'. In color TN displays, color filters are used to create a full spectrum of colors. These filters are placed over the pixels, with each pixel associated with red, green, and blue subpixels. Each subpixel is isolated and can be controlled by the electric field.

In addition to display applications, LCs have been used as light modulation modules in more sophisticated non-display photonic devices [130] such as real-time holograms [131, 132], all-optical interconnects [133], optical tweezers [134], and many others [135]. Most recently, they have been used for the control of magnetic microbots [136], terahertz beam-steering applications [137] and for an artificial iris application [138, 139]. In all such light-modulation applications, LCs were switched from an initial state, which is determined by an alignment process, to a final equilibrium state.

Apart from display and light modulation applications, LCs are also widely used in sensing applications, which can detect various environmental parameters like humidity, pressure, and chemical substances. The most common example is temperature sensors. As mentioned in section 2.2, the pitch length of CLC could be determined by the temperature and concentration of the chiral dopant. For a specific CLC sensor with a fixed concentration of chiral dopant, temperature is the only factor that would influence the pitch length. Moreover, the variation in pitch length can be revealed by selective reflection. As the reflected colour of the CLC sensor changes, the temperature of the object is visualized. Normally, high temperature will result in a smaller pitch length, and then the reflect band shifts to shorter wavelengths, which is also known as blue shift.

LC materials have diverse applications in different fields, especially in display and sensing applications. The properties and behavior of LCs are influenced by factors including temperature, magnetic field and electric field. Therefore, LCs are widely used in reconfigurable devices. In the research, I will investigate using LC material in light modulation for wearable applications.

Liquid Crystal Cell Fabrication and Related Materials

LCs are involved in various modern display technologies, ranging from digital screens to optical devices. A basic LC cell includes substrates, alignment layers, spacers, transparent electrodes, and LC materials. An example structure of LC cell is demonstrated in Fig. 3.1. Moreover, each layer has multiple optional materials. In this chapter, I will introduce the fabrication of LC cells and related materials.
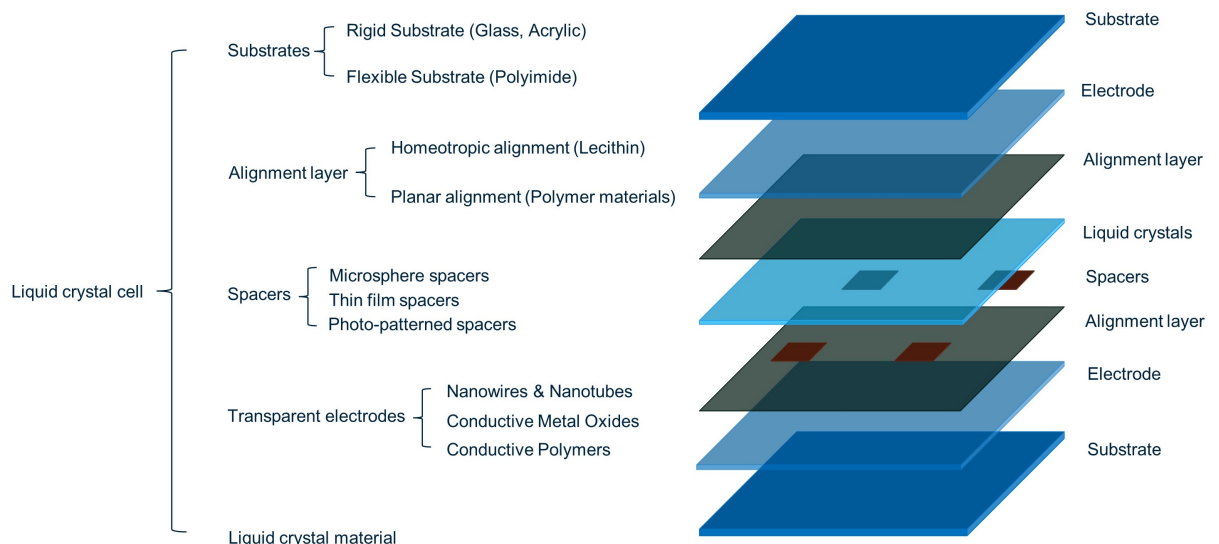
Figure 3.1: The schematic diagram of a LC cell, which includes substrates, alignment layers, spacers, transparent electrodes, and LC materials.

3.1 Transparent Electrodes

To integrate LCs with smart glasses applications, the use of transparent electrodes is necessary. Transparent electrodes are widely used in various modern electronic devices, particularly in applications that require the transparency of the system while also providing electrical conductivity. These transparent conductive materials have been applied in touchscreens, solar cells, organic light-emitting diodes (OLEDs) and smart windows [140]. For LC cell fabrication, transparent electrodes play a crucial role since they allow light to pass through while simultaneously facilitating the flow of electrical current. Many types of transparent electrodes have been used in photoelectric applications. Here, I listed 4 different transparent electrode materials and their pros and cons, including carbon nanotubes (CNTs), silver nanowires (AgNWs), Indium tin oxide (ITO) and Poly(3,4-ethylenedioxythiophene) polystyrene sulfonate (PEDOT:PSS), as is shown in Table 3.1. In this chapter, I will introduce three main categories of common transparent electrodes, outlining their advantages and disadvantages.

Table 3.1: Previous Research of Transparent Electrodes

Category	Material	Pros	Cons	Ref.
Nanoparticles	CNT	Flexible, Easy to Fabricate	High Cost	[141–143]
	AgNWs	Flexible, Easy to Fabricate	Oxidation	[144–146]
Metal Oxide	ITO	Good Transparency	Rigid	[147–149]
Conductive Polymer	PEDOT:PSS	Flexible, Good Transparency	High Sheet Resistance	[150–152]

3.1.1 Nanowires & Nanotubes

CNTs are well-known nanomaterials, which have been used for electronics, nano-composites, sensors and drug delivery applications. CNTs have cylindrical structures made up of carbon atoms arranged in a hexagonal lattice, much like a single layer of graphene rolled into a tube. Therefore, CNTs exhibit high strength and good conductivity. Additionally,

CNTs are highly transparent in the visible light spectrum. In comparison to other nanoparticle electrodes, such as AgNWs, CNTs are relatively stable in air and can maintain their properties for a long time. [153] However, the production cost of CNT electrodes is expensive, which limits their applications [154].

Apart from CNTs, AgNW is also a widely used transparent electrode material. Silver has excellent conductivity, and when formed into nanowires, AgNWs retain their high electrical conductivity. Similar to CNTs, AgNWs also exhibit good transparency in the visible light spectrum. Moreover, AgNWs have excellent flexibility, which enables them to be widely used in flexible electronic applications [155]. However, there are also drawbacks for AgNWs. Firstly, silver is easy to oxidize in air, especially in the presence of moisture, which results in high sheet resistance [156]. Secondly, AgNWs may not be suitable for high-temperature applications due to their relatively low melting point. High temperature can lead to a loss of structure and function [157].

3.1.2 Conductive Metal Oxides

Conductive metal oxides exhibit electrical conductivity, similar to metals, while also having the chemical composition of metal oxides, which have been used in a variety of electronic, optoelectronic, and energy-related applications. ITO is one of the most well-known conductive metal oxides, which have high transparency, conductivity, smoothness and stability [158]. Compared with nanoparticle electrodes, the advantage of ITO electrodes is smoothness, which is important for applications like LCDs and OLEDs, where a smooth, uniform surface is needed for high-quality display performance. However, ITO is rigid and brittle, so it is not suitable for flexible electronic devices, such as flexible screens and flexible sensors [159]. In addition, the deposition of ITO requires a sputter deposition system and consumables, such as an ITO target, which results in relatively high costs.

3.1.3 Conductive Polymers

Conductive polymers are a class of organic materials that are conductive and have the mechanical properties of traditional polymers. Apart from common applications of transparent electrodes, some conductive polymers exhibit bio-compatibility which can also be used in biomedical devices, for example, drug delivery systems and biosensors [160]. PEDOT:PSS is a conductive polymer composite that is widely used in various electronic and optoelectronic applications. Compared with conductive metal oxides and nanoparticle electrode materials, PEDOT:PSS exhibits relatively high sheet resistance, which limits it being applied in transparent circuits as wires. However, for some applications, PEDOT:PSS is used for plane electrodes to generate electric fields, which do not require low sheet resistance, such as LCD applications. Additionally, PEDOT:PSS has good chemical stability, which is essential for long-term device performance, especially when exposed to various environmental conditions [161]. Moreover, PEDOT:PSS electrodes can be processed from a solution, which could be deposited via spin coating, inkjet printing and roll-to-roll printing. Therefore, PEDOT:PSS is widely been used in industrial production.

In my research, I explored the fabrication of transparent electrodes with AgNW, PEDOT:PSS and ITO. In Chapter 4, I will introduce a process to deposit AgNW material on uneven surfaces using the Mylar bar-coating method, where a Polyvinyl chloride (PVC)-based Fresnel lens serves as the target surface. Additionally, I investigated the impact of varying AgNW suspension concentrations on transmittance and sheet resistance. To further reduce sheet resistance, PEDOT:PSS was deposited on the AgNWs. This work offers a solution for the uniform deposition of AgNWs on patterned surfaces, which can be applied to the next generation of optical devices. In Chapter 6 and 7, I demonstrate tunable CLC-based glasses for AR and photosensitive epilepsy treatment, which requires low sheet resistance and good stability. Therefore, ITO is used as electrode material in these two applications.

3.2 Alignment Layer

As previously shown from Fig. 2.2, alignment is necessary to enable LCs to be directional. The alignment layer is a thin coating applied to the inner surfaces of the LC cell. As mentioned in Chapter 2, the primary purpose of alignment layers is to utilize the anchoring effect to control the orientation of LC molecules, ensuring that they align in a specific direction. Alignment layers are crucial for LCD applications and other LC-based optical devices. Here, two main types of alignment are introduced, as well as the methods to achieve the alignment.

3.2.1 Homeotropic Alignment

Homeotropic alignment means that LC molecules are aligned perpendicular to the substrate surface. This alignment is applied in some advanced LCDs and electro-optic devices. Several methods can result in homeotropic alignment in LC materials. The first method is to apply a layer of alignment materials to the substrate surfaces to introduce homeotropic alignment, for example, lecithin [162, 108]. In addition, homeotropic can be introduced by creating surface structures or patterns at the nanoscale that guide the LC molecules into a homeotropic orientation [163, 164]. homeotropic aligned LCs can be driven by metallic interdigitated electrodes, which were reported in [165]. These were used for the measurement of flexoelectricity in NLCs.

3.2.2 Planar Alignment

Planar alignment means the LC molecules are oriented parallel to the substrate surface. This alignment is important in various LC devices, especially in LCD applications and electro-optic devices. Planar alignment is crucial for controlling the optical properties of LC materials. The surface treatment method can be used to achieve planar alignment. Firstly, coating the substrate with polymer materials, such as polyimide (PI) [166, 167], polyvinyl alcohol (PVA) [168, 169] and polymethyl methacrylate (PMMA) [170, 171]. After that, mechanical rubbing of the substrate surfaces in a specific direction using a cloth or soft brush can create microscopic grooves which guide the LC molecules to align parallel to the direction of rubbing. Planar alignment is advantageous for various display applications. For TN display applications, planar alignment is used in combination with a twist of LC material to control light transmission as is mentioned in Chapter 2. In Chapter 6 and 7, planar alignment is applied to a CLC-based lens to ensure uniform optic behaviors throughout the cell.

3.3 Spacers

In LC cell fabrication, spacers are used to control the thickness of the LC layer. These spacers help maintain a uniform gap between the substrates, ensuring that the optical properties of the cell meet the desired specifications. Here, three types of spacers that are commonly used in LC fabrication are listed.

3.3.1 Micro-spheres Spacers

Micro-spheres spacers are small spherical particles used in various technologies and industries [172]. Normally, glass micro-spheres spacers are used in LC cell fabrication since it is transparent and rigid. Micro-sphere spacers have uniform diameters that can range from a few microns to hundreds of microns. Micro-sphere spacers can be mixed with LC material and placed between top and bottom substrates, where the thickness is precisely controlled via the spacer. Using micro-sphere spacers in LC cell fabrication is simple to process and suitable for a wide range of LC devices. However, due to the rigidity of the spacer, it might cause damage to substrates during fabrication. Moreover, micro-spheres spacers are not suitable for flexible applications.

3.3.2 Thin Film Spacers

In addition to micro-sphere spacers, thin film spacers are also widely used in LC cell fabrication [173]. Spacer films are sheets of plastic or other materials with uniform thickness. The thin film spacers are required to be rigid and compatible with LC material, for example, Mylar film. Different from micro-sphere spacers, the thin film spacers need to be placed at the four corners of the bottom substrate and covered with the top substrate. After that, UV adhesive is applied to the edge of the cell and exposed to UV light to fix the gap between the two substrates. Compared with micro-sphere spacers, thin film spacer is low cost and easy to assemble. However, the thin film will occupy a certain area that will influence the optic properties of LC cells in that area.

3.3.3 Photo-patterned Spacers

Photo-patterned spacers are created with photoresist material. It allows for precise and patterned control of the LC cell thickness, enabling complex LC cell designs [174]. Here is a process of fabricating a 10-micron spacer using the photolithography method, as is shown in Fig. 3.2a. Firstly, the glass substrate was cleaned via IPA with an ultrasonic bath for 5 mins. This step is to clean the substrate so that the photoresist material can be better attached to its surface. Secondly, photoresist AZ4562 was uniformly coated on the substrate via spin coating at 2000 rpm for 30 seconds. Thirdly, the substrate was soft baked at 95°C for 30 seconds. This process evaporates the solvent in the photoresist and prepares it for exposure. AZ4562 is a positive photoresist so the exposed area could be dissolved by developer solvent. Therefore, the coated substrate was then exposed to UV light for 60 seconds via a mask aligner (MA6), with a mask that blocks the spacer area from the UV light. After that, the substrate was dipped in developer AZ 400k for 5 mins, which was diluted 1:5 with water. After that, the photoresist-based pattered spacers were fabricated. The last step was to rinse the substrate with running water for 5 minutes to remove the residual chemicals. Compared with previously mentioned spacers, photo-patterned spacers allow precise control of cell thickness and pattern of spacer, which enables more complex LC cell designs. As is shown in Fig. 3.2b and c, a LC cell was fabricated using photo-patterned spacers, which have high uniformity. However, the fabrication process is complicated and has higher manufacturing costs.

3.4 Fabrication Process

In the previous section, the materials related to LC cell fabrication are introduced, including electrode materials, alignment materials and spacer materials. In this section, I will introduce a process of fabricating a LC cell in the lab, as is shown in Fig 3.3. Firstly, the glass substrate was cleaned via IPA with an ultrasonic bath for 5 minutes and dried
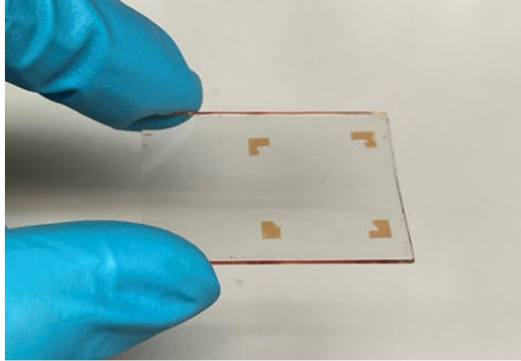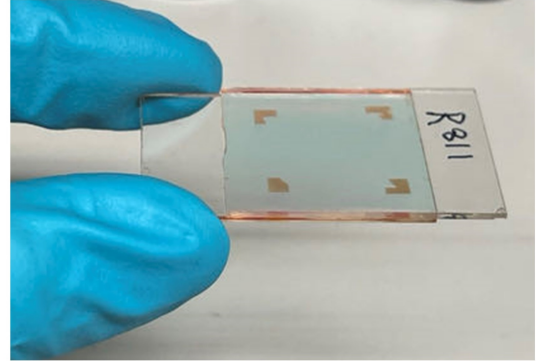
Figure 3.2: (a) Fabrication process of photo-patterned spacers. (b) Fabricated photo-patterned spacers using photoresist AZ4562 with 10 μm thickness. (c) a LC cell using photo-patterned spacers technique.

with a nitrogen gun. This step is to ensure the alignment layer can better adhere to the substrate. Secondly, an alignment layer is coated on the substrate via the spin-coating method. In my previous research, I used PMMA solvent (4% solid content anisole solvent, AllResist) and set the speed of the spin-coater to 2000 rpm, resulting in an alignment layer thickness of 150 nm. To align LC molecules in a certain direction, the alignment layer was rubbed by a soft brush or cloth at the desired orientation. Thirdly, four pieces of thin film spacers were placed at the four corners of the bottom substrate and covered with the top substrate. UV adhesive (NOA68) was smeared on two edges of the cell to fix the gap between the two substrates. After that, uniform force was added to two substrates to ensure the uniformity of the thickness, then the cell was exposed to UV light for 10 mins to cure the glue. Till now, an empty LC cell was fabricated. Subsequently, the cell was placed on a hot plate and heated to 50 °C and a droplet of LC material was dropped at one edge of the cell, where the LC material will flow into the empty cell due to surface tension. Noticeably, the temperature of the hot plate should be higher than the clear point of the LC material, so that the LC material will transform into an isotropic phase and speed up the process. The last step was to seal the rest of the two edges after the LC cell was filled with LC material.
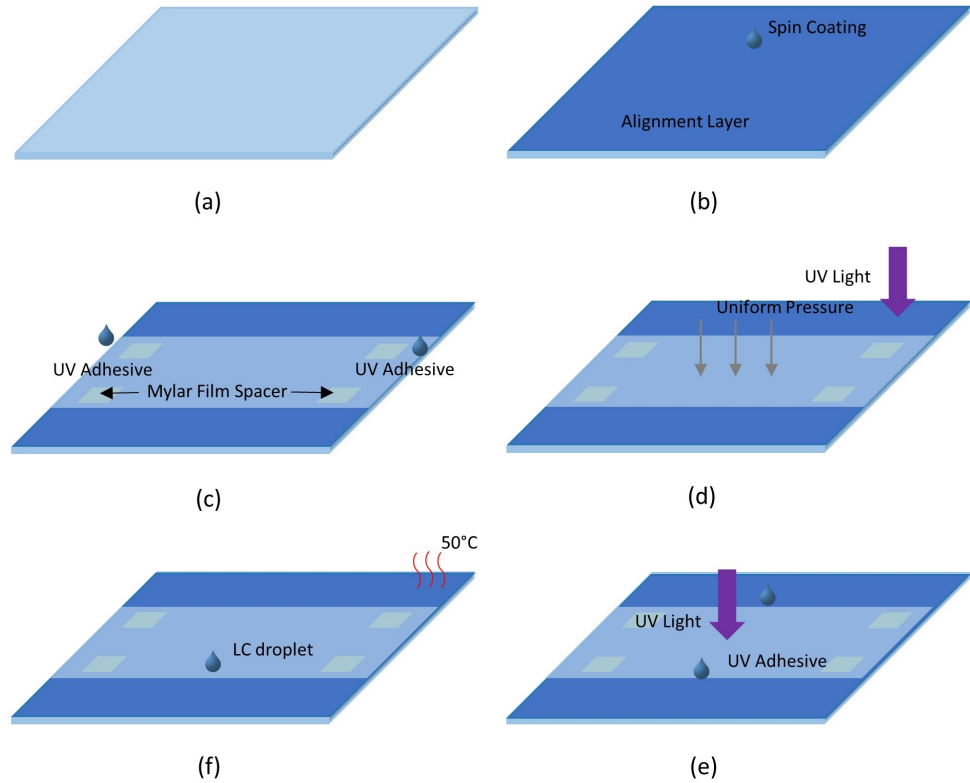
Figure 3.3: Fabrication process of a simple LC cell. (a) A glass substrate. (b) Spin-coating alignment layer. (c) Place thin film spacers between two substrates and fix the gap using UV adhesive. (d) Apply uniform pressure to the cell and expose it to UV light. (e) Place a droplet of LC material on the edge of the top substrate and heat the cell. LC material will flow into the gap between two substrates. (f) Seal other two edges of LC cell using UV adhesive.

3.5 Characterization

A range of characterization techniques has been employed, including the use of microscopes as mentioned in Chapter 2. In Chapter 4, sheet resistance was measured using a four-point probe method (Hall Effect Measurement System, Nanometrics), and transmittance under different light wavelengths was assessed with a UV-Vis spectrometer (Ultrospec 9000). Additionally, surface patterns were measured using an Optical Profilometer and Stylus Profilometer (Bruker). SEM and AFM images were captured to inspect the nanostructure of the electrode. In Chapters 6 and 7, thermal analysis was conducted using a DSC instrument (DSC 25, TA Instrument). The transmission spectrum of CLC lenses was measured by a spectrometer (USB2000+ fiber optic, Ocean Optics). An infrared thermal camera (Testo 865) was utilized to measure the surface temperature.

Chapter 4

Transparent Electrodes for Patterned Liquid Crystal Devices

AgNW is emerging as a next-generation transparent electrode material, offering enhanced flexibility and ease of fabrication compared to traditional transparent electrode materials, such as metallic oxides. Previous research has demonstrated the uniform deposition of Ag-NWs on flat surfaces, exhibiting high conductivity, flexibility, and excellent transmittance. However, the evolution of nano-electronics technology has necessitated the fabrication of transparent electrodes on non-flat surfaces, such as those found in zenithal bistable devices (ZBDs) and reconfigurable Fresnel lenses. In this study, I proposed a method to deposit AgNW material on uneven surfaces using the Mylar bar-coating method, with a PVC-based Fresnel lens serving as the target surface. Additionally, I investigated the impact of varying AgNW suspension concentrations on transmittance and sheet resistance. To further reduce sheet resistance, a layer of conductive polymer, PEDOT:PSS, was deposited on the AgNWs. This research offers a solution for the uniform deposition of AgNWs on patterned surfaces, paving the way for the next generation of optical devices.

4.1 Introduction

As nanofabrication technology advances, the demand for transparent electrodes in wearable and tunable optical devices is increasing. Traditional transparent electrode materials are metallic oxides, such as ITO. ITO exhibits good electrical properties and transparency, which has been widely employed in e-paper, solar cell, and display applications [153, 175]. However, due to the physical properties of metallic oxides, ITO is brittle and unsuitable for flexible devices. In addition to that, ITO electrode is costly and requires sophisticated equipment to fabricate. In such cases, conductive nanomaterials like graphene, AgNW, and CNT can be used to fabricate transparent and flexible electrodes, which have broad applications in foldable screens and e-skin devices [176–178]. Among these nanomaterials, AgNW offers relatively lower sheet resistance and fabrication costs, making it a popular choice for creating transparent and flexible electrodes [179, 180]. In this chapter, I focused on developing techniques to deposit AgNW on uneven substrate surfaces.

Previous studies have successfully deposited AgNW on flat surfaces using spin coating, drop coating or spray deposition. [181–184]. Different deposition processes result in varying transmittance and sheet resistance values, as shown in Table 4.1 [185, 155]. Post-processing can further reduce sheet resistance, employing both chemical and physical methods [185]. Chemical methods involve incubating AgNW-coated thin films in hydrogen chloride (HCl) vapor to reduce oxidized surfaces, significantly lowering sheet resistance. Physical methods, such as annealing [186, 181] and compression [187] , are the primary post-processes used to achieve reduced sheet resistance.

Existing literature mainly discusses AgNW electrode deposition on flat substrates. However, with the development of nanotechnology, researchers are now exploring the deposition of conductive materials on patterned substrates, such as ZBDs [188–190] and reconfigurable Fresnel lenses [191–193], as is shown in Fig. 4.1. The metallization processes typically involve evaporation and sputtering using metallic oxide materials, which

necessitate professional metallization equipment and increase fabrication costs. Additionally, metallic oxides are fragile, rendering them unsuitable for flexible cells. AgNW, as a more flexible and cost-effective alternative, is a viable substitute for traditional transparent electrode materials. Due to the complexity of the surface structure, it is difficult to deposit AgNW on Fresnel lenses using traditional methods such as, for example, drop coating and spin coating. One feasible solution is to use the Mylar-bar coating method. Specifically, Mylar-bar coating is a process to control and apply a precise and uniform thickness of liquid material onto a flexible substrate. The height of the Mylar bar above the substrate is adjustable, which determines the thickness of the coating material. In comparison with other coating methods, Mylar-bar coating is more suitable for depositing AgNWs on patterned surfaces since the gap between the Mylar bar and substrate could be adjusted to ensure the coating material is uniformly distributed on the surface.
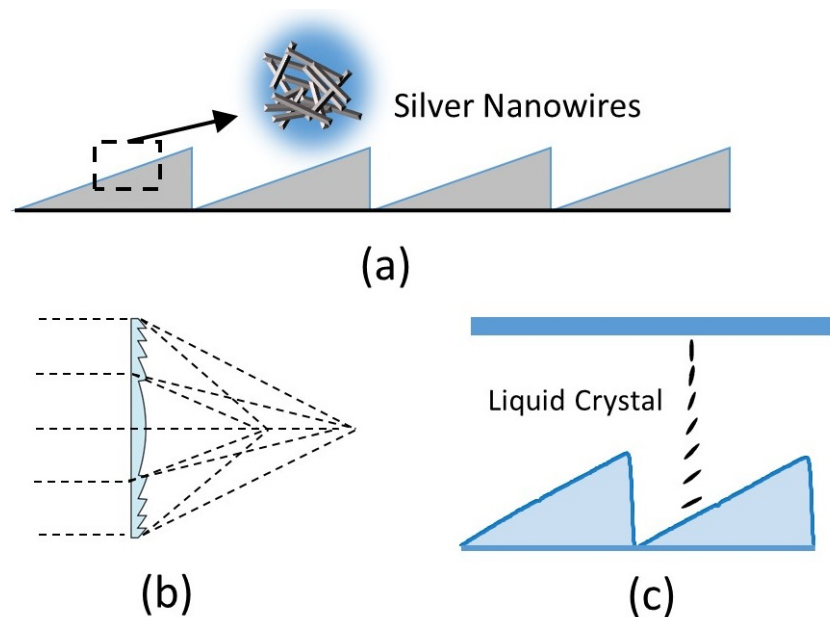
Figure 4.1: (a) The concept of depositing AgNWs on a patterned surface, as well as two potential applications that involve. (b) Reconfigurable Fresnel Lenses. (c) Zenithal Bistable Devices (ZBDs).

In this chapter, I will demonstrate the process of depositing AgNW on patterned surfaces and showcase how varying AgNW suspension concentrations influence transmittance and sheet resistance. I will also discuss post-processing techniques to further reduce sheet resistance. Specifically, I used a PVC-based Fresnel lens as the target substrate due to its low cost, flexibility, and scalability. Notably, the low melting point of PVC material ne-

cessitates temperature control below 50 degrees Celsius to avoid permanent deformation. The outcomes of the research will contribute significantly to the development of future reconfigurable LC technology, including optical switches [194, 195], tunable antennas [196], adjustable-focus eyewear [197] and innovative display technologies [198, 199].

Table 4.1: Previous Research of AgNWs

Ref.	Fabrication methods	Purpose	T (%)	R_{sheet}	Post-Processing
[181]	Drop Coating	Solar Cell	84.7	10.3	Annealing
[182]	Transfer process	Percolation Network	85	10	Annealing
[184]	Spray Deposition	/	90	50	/
[187]	Drop Coating	Solar Cell	/	8.6	Compression
[144]	Drop Coating	Transparent Electrodes	95	580	Illumination
[145]	Flood Coating	Patterned Electrode	87.4	8.2	Repeat Coating
[146]	Spin Coating	Flexible OLED	83	12	PEDOT:PSS

4.2 Methodology

4.2.1 Fabrication Process

Firstly, the AgNW isopropyl alcohol (IPA) suspension (5 mg/mL, Sigma-Aldrich) was diluted to concentrations ranging from 1 to 5 mg/mL using IPA. This step is to prepare different concentrations of AgNW suspensions for electrode fabrication. Using a high concentration of AgNW IPA suspension for electrode fabrication would result in a greater accumulation of silver material per unit area, leading to low sheet resistance but also reduced transmittance. Therefore, five different concentrations of AgNW IPA suspensions were prepared to examine the influence of AgNW suspension concentration on sheet resistance and transmittance.

Secondly, the substrate (Fresnel lens) was immersed in IPA solvent in an ultrasonic cleaner for five minutes and then dried using a nitrogen flow, as is shown in Fig. 4.2a. Notably, the Fresnel lens is made of PVC, which can dissolve in some alcoholic solvents, such as ethanol. Consequently, these materials must be avoided when cleaning samples and diluting AgNW suspension. Following this, two 50 μm spacers of Mylar film were placed at the edge of the cleaned substrate, as shown in Fig. 4.2b. The Mylar film spacer was adhered to using optical glue NOA61 and exposed to UV light to cure the glue. This step fixed the spacer and eliminated the gap between the spacer and the patterned substrate. The spacer ensured that each unit area of the substrate received the same volume of material, allowing for a uniform AgNW coating.

Subsequently, the AgNW suspension was dropped onto the edge of the substrate and deposited using the Mylar bar-coating method, as shown in Fig. 4.2c and d [200]. After deposition, the substrate was baked on a 50 °C hot plate for five minutes to solidify the AgNWs. Finally, the spacers and part of the edges were removed to obtain a uniformly coated area, as shown in Fig. 4.2e and f.

4.2.2   Post-processing

As previously mentioned, several post-processing methods can be used to further reduce the sheet resistance of AgNW electrodes. Annealing is an effective post-processing technique aimed at improving the quality of AgNW deposition by reducing the joint resistance between the nanowires. Typically, AgNWs could be annealed at temperatures ranging from 100 to 150 °C [201, 146]. However, due to the low melting point of PVC material, post-processes involving high temperatures are unsuitable for the application. Other high-temperature methods such as plasma and microwave processes can also cause a temperature increase in the substrate, potentially damaging the surface pattern. Moreover, mechanical compression methods were ruled out due to the inherent low rigidity of the
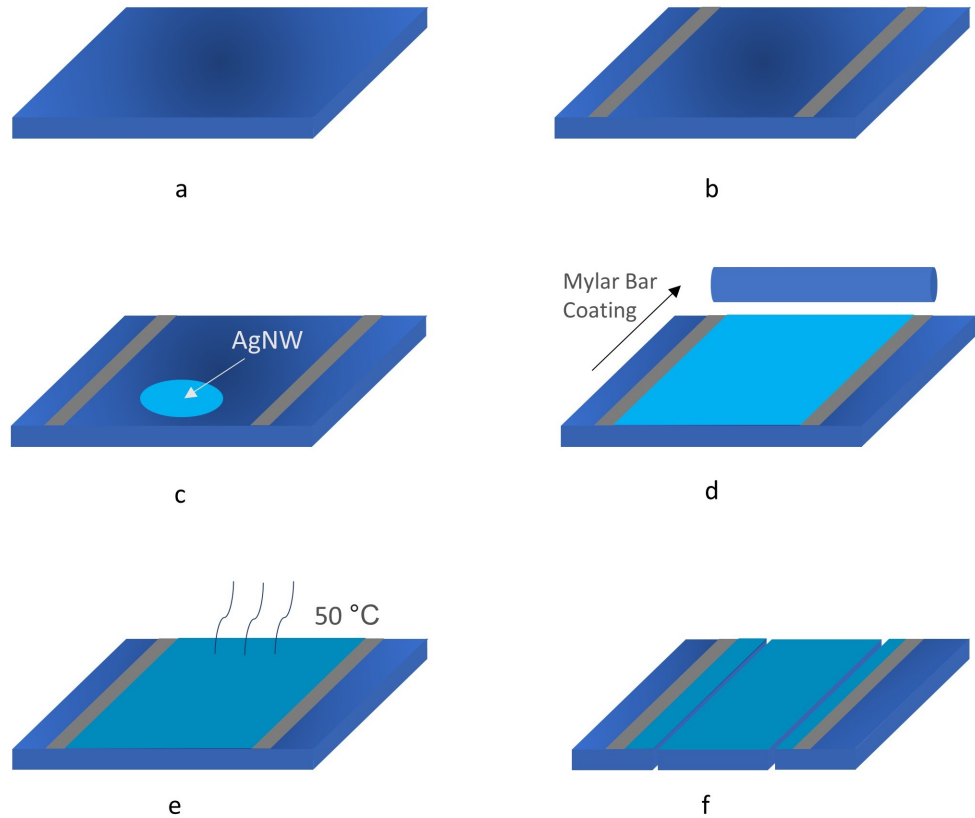
Figure 4.2: Processes of depositing AgNWs on patterned substrate. (a) Target substrate. (b) Two Mylar film spaces adhesive on two sides of the substrate. (c) Place one droplet of AgNW material on one side of the sample. (d) Use Mylar-bar coating method to uniformly deposit AgNW material. (e) Heat the substrate on a hot plate at 50 degrees to evaporate IPA. (f) Remove spacers and uncoated area.

PVC substrate. High pressure cannot be applied uniformly across the patterned surface without risking damage to the Fresnel lens pattern. Therefore, chemical processes emerged as the most suitable approach for PVC substrates, which is why I used PEDOT:PSS treatment as a post-processing technique to effectively reduce the sheet resistance.

PEDOT:PSS is a conductive polymer mixture widely used in transparent electrodes and flexible organic devices [202]. Previous research has demonstrated that PEDOT:PSS can reduce joint resistance in AgNW networks and decrease surface roughness by encapsulating AgNWs. In this chapter, I show that PEDOT:PSS can also improve the conductivity of patterned substrates without affecting their optical properties [146].

In the experiment, I first deposited AgNWs uniformly onto the substrate. Subsequently, Orgacon S305 (0.54 % PEDOT:PSS in H_2O, Sigma-Aldrich) was spin-coated over the AgNW layer at a speed of 1000 rpm, achieving a thickness ranging between 50 and 60 nm [203]. Following practices documented in prior literature, the substrates were then heated on a 50 °C hotplate for 10 minutes to solidify the polymer. It is important to note that PEDOT:PSS is typically applied from a solution, which requires solvent evaporation for film solidification. High-temperature annealing speeds up this evaporation, enabling the polymer chains to realign and the film to solidify more effectively. This process yields a denser and more ordered structure, thereby boosting electrical conductivity. However, due to the substrate's limitations, I could only solidify the PEDOT:PSS at 50 °C. While this is not the optimal annealing temperature for PEDOT:PSS deposition, the result still showcased commendable conductivity. After solidifying at 50 °C, there was a notable reduction in the sheet resistance of the AgNW. Based on prior research, I understand that increasing the film's thickness by repeating the spin-coating process can further enhance conductivity and smooth the surface. However, this method might also decrease light transmittance and slightly modify the surface pattern, potentially influencing optical properties.

4.2.3 Characterization

This chapter focuses on examining how different concentrations of AgNW suspension influence sheet resistance and transmittance. Additionally, I investigate the use of post-processing to further reduce sheet resistance. Sheet resistance was measured using the four-point probe method with a Hall Effect Measurement System (Nanometrics) [204]. Furthermore, transmittance under various light wavelengths was measured using a UV-Vis spectrophotometer (Ultrospec 9000). According to these measurements, I determined the relationship between the concentration of AgNW suspension and transmittance. The results also showed how the PEDOT:PSS process reduced both transmittance and sheet resistance.

Moreover, an Optical Profilometer and Stylus Profilometer (Bruker) were used to measure surface patterns after deposition. This step demonstrated that the deposition of AgNW and PEDOT:PSS did not influence the substrate's pattern, ensuring that the optical properties of the Fresnel lens remained unaffected. Additionally, SEM images were captured before and after the post-process to observe the impact of PEDOT:PSS on AgNWs in reducing sheet resistance. AFM was employed to measure surface geometry, illustrating that PEDOT:PSS reduced surface roughness and increased mesh connectivity within the AgNW network.

4.3   Results and Discussion

Initially, after applying five different concentrations of AgNW suspensions uniformly onto the Fresnel lens using the previously mentioned Mylar bar-coating method, the transmittance at different wavelengths was measured using UV-vis, as shown in Fig. 4.3a. The transmittance significantly decreased as the concentration of AgNW suspension increased. A higher concentration of AgNW suspension resulted in a denser AgNW network, which influenced the transmittance. Subsequently, the transmittance was measured after the PEDOT:PSS process and plotted in Fig. 4.3b. Compared to Fig. 4.3a, the transmittance dropped between 3 to 7% after the process. Notably, samples deposited with higher concentrations of AgNW suspension had denser AgNW networks, which retained more residual PEDOT:PSS material after spin coating, resulting in a larger drop in transmittance.

Moreover, I used the four-point probe method to measure the sheet resistances of five samples for each suspension concentration. The average sheet resistances for these are illustrated in Fig. 4.3c. The data indicated that a suspension with a lower concentration led to a sparser AgNW network, resulting in a higher sheet resistance. With the increase in concentration from 1 to 3 mg/mL, the sheet resistance dropped from 375.75 to 32.64
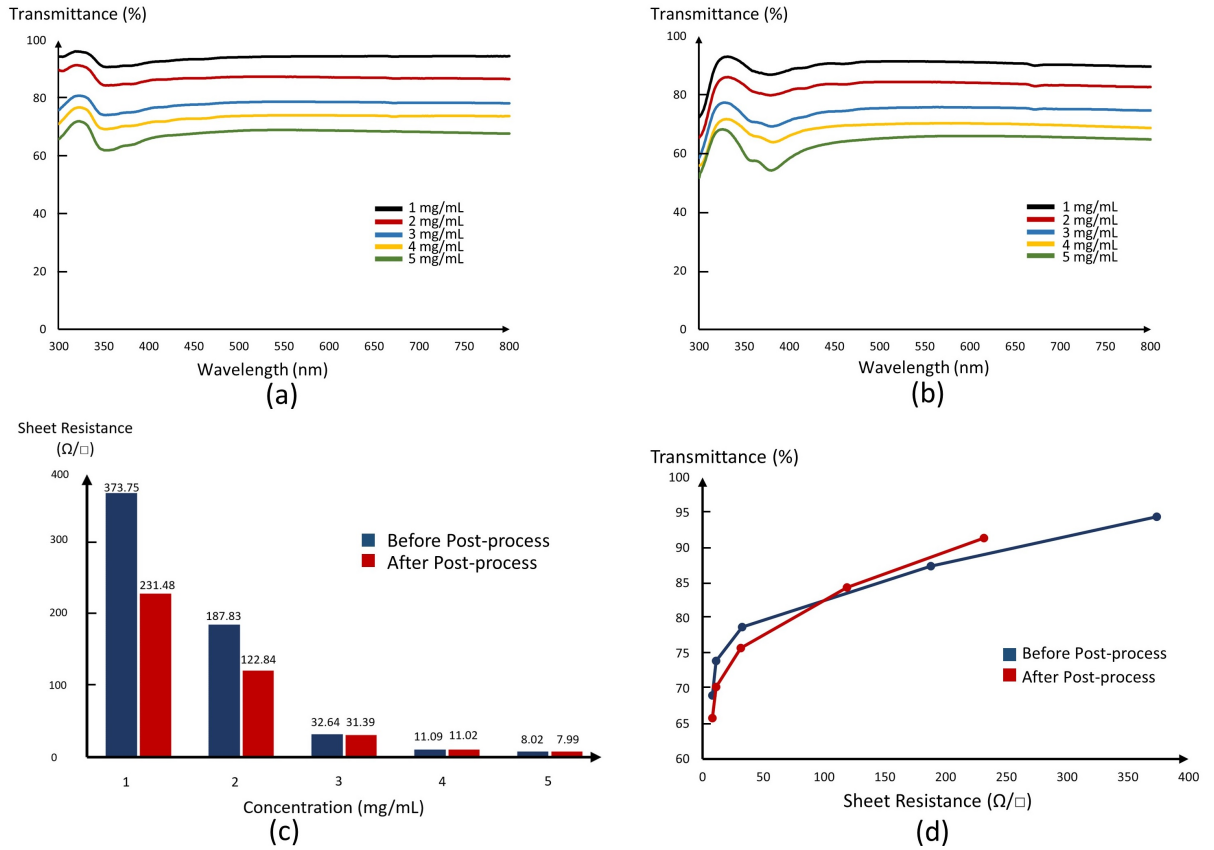
Figure 4.3: (a) Transmittance of samples coated by different concentration of AgNW suspension before PEDOT:PSS process. (b) The transmittance after PEDOT:PSS process. (c) Sheet resistance of samples coated by different concentration of AgNW suspension before and after PEDOT:PSS process. (d) The relationship between sheet resistance and transmittance at 550 nm.

Ω/sq. However, for the samples with concentrations of 4 and 5 mg/mL, the reduction in sheet resistance was small, moving from 11.09 to 8.02 Ω/sq. Upon applying the PE-DOT:PSS process, another set of measurements was taken and is also shown in Fig. 4.3c. Relative to the earlier findings, the PEDOT:PSS process brought about a reduction in sheet resistance, demonstrating a more pronounced effect on samples with lower concentrations. For instance, the average sheet resistance for the 1 mg/mL AgNW samples was originally 373.75 Ω/sq and decreased to 231.48 Ω/sq post-PEDOT:PSS treatment. However, for denser AgNW samples, particularly those above 3 mg/mL, the influence of the PEDOT:PSS process on sheet resistance was minimal. The underlying reason for this observation is linked to the structure of high-density AgNW samples, since they possess a greater number of crossing junctions within their networks. These junction resistances are

connected in parallel, meaning high-density AgNW samples are less affected by junction resistance compared to their low-density counterparts. Since PEDOT:PSS primarily acts to reduce junction resistance, it naturally has a more significant impact on reducing sheet resistance in samples with a lower density of AgNWs.

According to Fig. 4.3a-c, the relationship between transmittance and sheet resistance for different AgNW concentration samples can be determined. As shown in Fig. 4.3d, an intersection point occurs between the two curves at around 103 Ω/sq. For samples with a target sheet resistance above 103 Ω/sq, the PEDOT:PSS process could help achieve higher transmittance. However, for samples requiring sheet resistance no greater than that, the PEDOT:PSS process is not ideal, as it might result in lower transmittance. In this case, the AgNW electrode on the patterned surface is intended for reconfigurable LC devices, where sheet resistance within the range of hundreds Ω/sq is desirable.

To better understand the substrate's behavior, SEM images were captured before and after the PEDOT:PSS process, as shown in Fig. 4.4. Prior to the application of PEDOT:PSS, the AgNW material was uniformly distributed across the substrate, resulting in nanowires that overlapped to create a well-connected AgNW network. The SEM images confirm both the uniformity and connectivity of the AgNW layer, in both flat and corner regions of the substrate. Moreover, the images show that a higher concentration of AgNW suspension leads to a denser network, but leads to reduced light transmission. Following the deposition of the PEDOT:PSS layer, the SEM images showed that the AgNWs were encapsulated by this conductive polymer. This encapsulation lowered the overall resistance of the AgNW network, thereby contributing to a subsequent reduction in sheet resistance.

In addition to reducing sheet resistance, PEDOT:PSS can also decrease surface roughness, which can be beneficial when fabricating LC cells with the substrate. A rough surface has an anchoring effect on LC molecules, which can cause light distortion. In Fig. 4.5, AFM images were taken to demonstrate that the PEDOT:PSS process can reduce surface
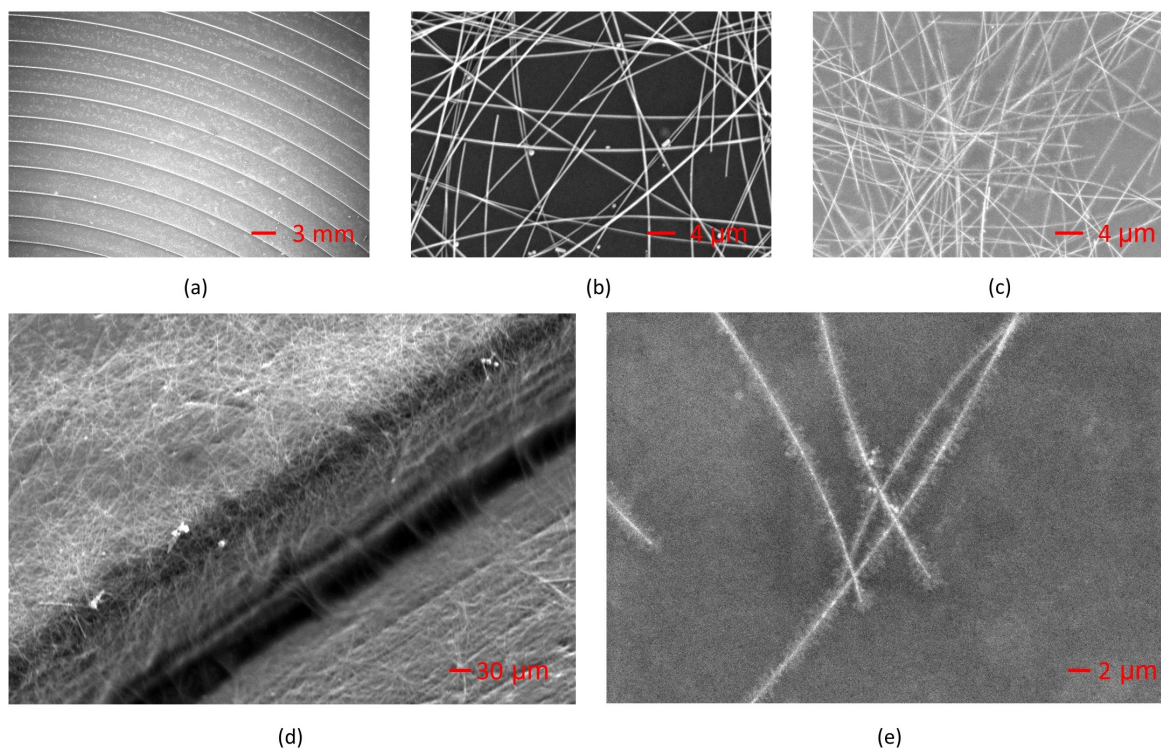
Figure 4.4: (a) Low magnification SEM image of Fresnel lens structure. (b) AgNWs network on flat area before PEDOT:PSS process. (c) AgNWs network on flat area after PEDOT:PSS process. (d) AgNWs network on patterned area. (e) AgNWs encapsulated by PEDOT:PSS.

roughness. Fig. 4.5a and b were captured before and after the post-process for a 3 mg/mL sample, where the surface roughness decreased significantly after the process. The height difference of the surface was 368.9 nm before the PEDOT:PSS process and dropped to 97.9 nm afterwards.

Furthermore, an optical profilometer was used to measure the geometry of an uncoated Fresnel lens, as shown in Fig. 4.6a. This surface structure enables the Fresnel lens to focus light and magnify objects. To ensure the optical properties of the substrate are not affected by the coated layers, the surface geometry of samples was measured by profilometers before and after deposition, as demonstrated in Fig. 4.6b. Compared to the non-coated sample, the patterns on coated substrates were slightly rounded at the corners, but the rest of the area maintained its structure. This result confirms that the substrate is still functional and that the processes do not affect its optical properties.
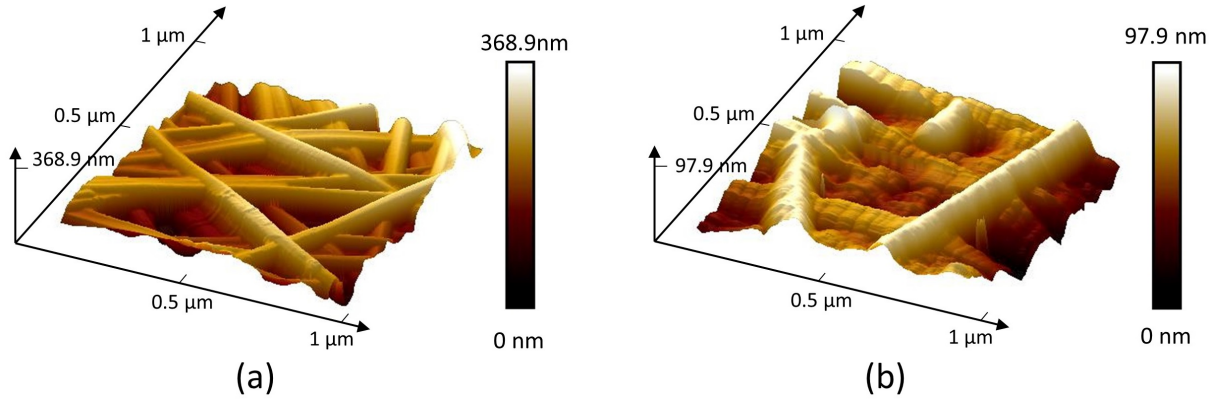
Figure 4.5: (a) 3 mg/mL sample before PEDOT:PSS process. (b) 3 mg/mL sample after PEDOT:PSS process.

4.4 Conclusion

In this chapter, I proposed a method to deposit AgNW material on patterned surfaces and studied how different concentrations of AgNW suspension influence transmittance and sheet resistance. Firstly, different concentrations of AgNW suspension were uniformly deposited on PVC-based Fresnel lenses. Secondly, transmittance and sheet resistance were measured before any post-processing. Samples deposited with 1 mg/mL suspension had an average sheet resistance of 373.75 Ω/sq and transmittance of around 94% at 550 nm, while the 5 mg/mL samples had a sheet resistance of 8.02 and transmittance of 69% at 550 nm. Afterward, the PEDOT:PSS process was investigated to reduce sheet resistance. According to the measurements, sheet resistance dropped significantly among the 1 mg/mL and 2 mg/mL samples, from 373.75 to 231.48 and 187.83 to 188.84 Ω/sq, respectively. However, for low sheet resistance samples, such as those deposited with suspensions over 3 mg/mL, the PEDOT:PSS process had a limited effect on further reducing sheet resistance. My analysis indicates that the PEDOT:PSS process could benefit plate electrodes with target sheet resistance above 103 Ω/sq. In this case, this work targets reconfigurable LC lenses and ZBD devices. According to previous studies, researchers have shown that substrates with sheet resistance ranging from 21.3 Ω/sq to 650 Ω/sq exhibit similar performance when switching a basic LC cell. Thus, the PEDOT:PSS process could be beneficial for AgNW transparent electrodes in these futuristic LC devices.
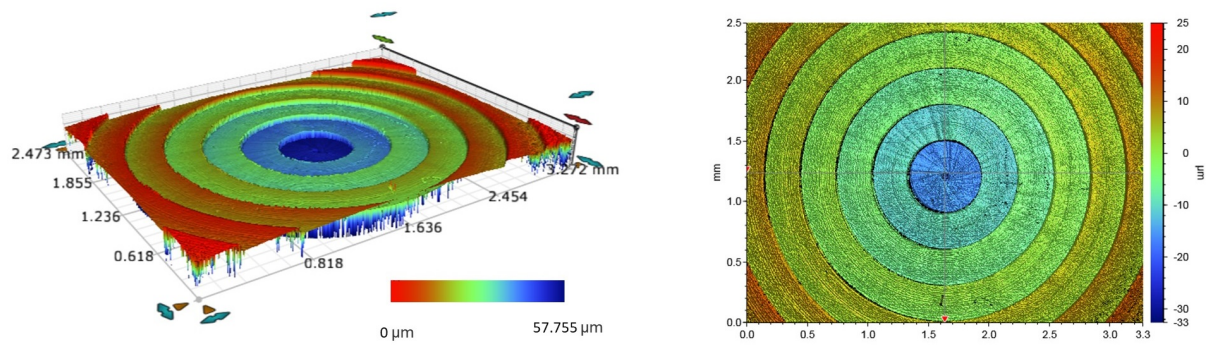
(a)
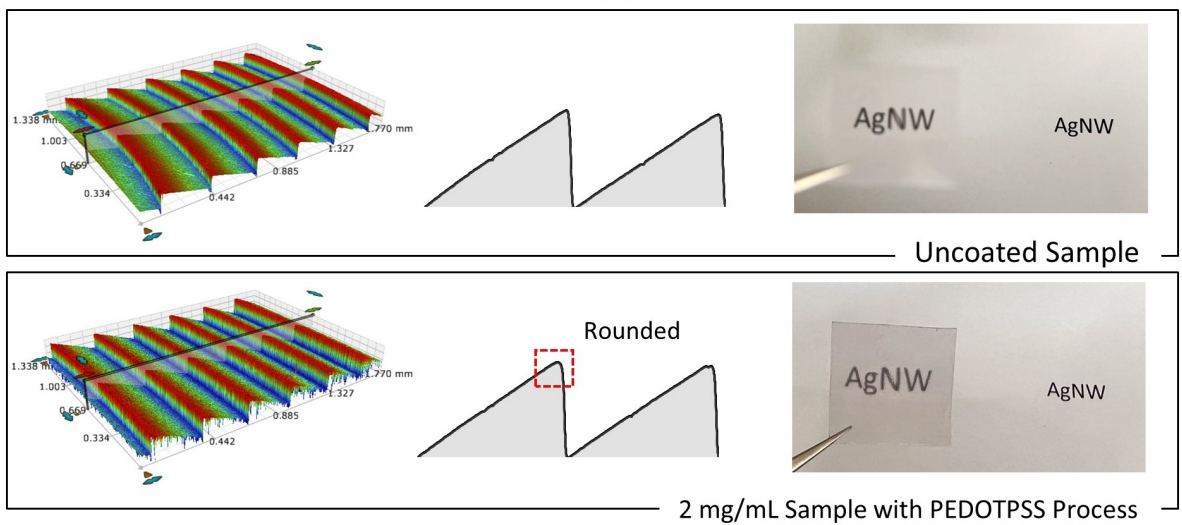
(b)

Figure 4.6: (a) The basic structure of an uncoated Fresnel lens. (b) Comparison between an uncoated sample and 2 mg/mL sample. The surface structure was measured via profilometers.

Compared to previous research on flat surfaces, this work has relatively higher sheet resistance for the same transmittance, which is due to the properties of the substrate. Any post-processing that introduces heat compression to the surface might damage the pattern. Therefore, only limited post-processing methods are suitable for this substrate. However, PVC substrates offer advantages such as low cost, ease of fabrication, and resizability. This work presents a feasible solution for depositing nanowires on patterned surfaces. Future research could further improve the method by investigating other post-processing techniques to enhance sheet resistance without affecting the transmittance of the substrate.

<div align="right">Chapter 5</div>

Reconfigurable Antenna for Smart Eye Glass Device

The antenna is one of the key building blocks of many wearable electronic devices, and its functions include wireless communications, energy harvesting and radiative wireless power transfer (WPT). In an effort to realise lightweight, autonomous and battery-less wearable devices, I demonstrated a reconfigurable antenna design for 5G wearable applications that require ultra-low driving voltages (0.4-0.6 V) and operate over a high frequency range (3.3-3.8 GHz). For smart glasses applications, previous antenna designs were 'fixed' and mounted on the eyeglass frame itself. Based on the theory that was presented in Chapter 2, I demonstrate a reconfigurable design that could be achieved on the lens itself, using an anisotropic LC material. I also demonstrate how LC alignment and electric field patterns strongly influence the tuning capabilities of these antennas in the gigahertz range and present a smart, reconfigurable spiral antenna system with a LC substrate.

5.1 Introduction

The electronic antenna is a circuit element that transforms a guided wave in transmission lines into a free-space wave and vice versa. Antennas are essential components for wireless communication systems and are widely used in both wearable and implantable devices. The two main applications of antennas in the literature are energy harvesting [205] and data transmission [44]. In this chapter, I demonstrated how an antenna's frequency can be tuned using LC materials, making it appealing for a range of energy harvesting and telecommunications applications.

Multi-functional wearable devices require both a wide frequency bandwidth and a miniaturized scale. For energy harvesting applications, a tunable frequency bandwidth device enables multiple RF wavelengths in free space to be harvested. Similarly, for communications applications, a tunable antenna enables wearable devices to transmit and receive broadband information [206], and helps reduce mismatch and noisy interference when communicating with other devices [207]. In addition, and in comparison with traditional antennas, a tunable antenna can establish communication with multiple devices with different frequencies, which could play an important role in MIMO networks [208], making dynamically tunable antenna front ends a necessity in the near future. Consequently, I demonstrated a tunable antenna design that covers the frequency range of communications systems and consumes minimum energy in a limited area. Such an antenna design could be mounted on wearable or implantable devices to enable both communications and energy harvesting capabilities.

There are many tunable antenna strategies reported in the literature. For example, the method demonstrated by Huang *et al.* involved tuning the impedance of the matching network to change the reflection coefficient of frequency [209]. Other previous studies attempted to achieve electronic reconfigurability of the reflective arrays using varactor diodes [210]. Other methods involved using reconfigurable substrate materials, such as

controllable dielectrics [211, 212] and Barium Strontium Titanate [213]. However, the complexity of these approaches are not optimal when targeting wearable devices. In terms of LC-tunable antennas, A. Gaebler *et al.* devised a novel tunable antenna for millimeter wave applications [214] using a commercial NLC mixture, K15. According to their results, the resonant frequency could be tuned from $33.25\,\mathrm{GHz}$ to $37.1\,\mathrm{GHz}$, with a driving voltage reaching 20 V to tune the LC substrate. Obviously, this driving voltage is impractical for a wearable application, and the purpose of this chapter is to demonstrate that such a tunable wavelength range can be achieved using a much smaller driving voltage, making use of the previously demonstrated results showing that LCs demonstrate excellent RF performance in the gigahertz range and that the frequency range and tunable bandwidth can be expanded using different LC mixture materials [215, 216].

As utilized in the above-mentioned papers, and in the present work, the key benefit of LC-based antennas is their ability to exhibit analogue tuning of properties such as their permittivity and refractive index. As is mentioned in Chapter 2, this ability stems from the anisotropic nature of the LC phase which, at the molecular level, consists of anisotropic molecules which may be, for instance, rod-shaped or disc-shaped. This molecular shape anisotropy results in orientational, and sometimes positional, order, which then translates into a bulk phase anisotropy. This orientational ordering of the molecules means that the 'director', the ensemble average direction of LC molecular orientation, can be defined [120]. These anisotropic properties allow LCs to be manipulated through a balance of forces and torques due to an applied electric field and elastic effects, yielding a reconfigurable design where the bandwidth of the antenna can be easily and accurately tuned [136, 219]. In this chapter, I will consider those NLC which exhibit orientational anisotropy but no positional anisotropy.

Examples of antennas mounted on smart glasses are shown in Fig. 5.1(a)(i) and (ii), [218, 217]. In Fig. 5.1(a)(i), the antenna was placed on the eye-glass frame. In addition to such an antenna being fixed, placement on the eye-glass frame results in a bulky eye-glass frame. In Fig. 5.1(a)(ii), the antenna is instead placed at the far edge of the lens of glasses,
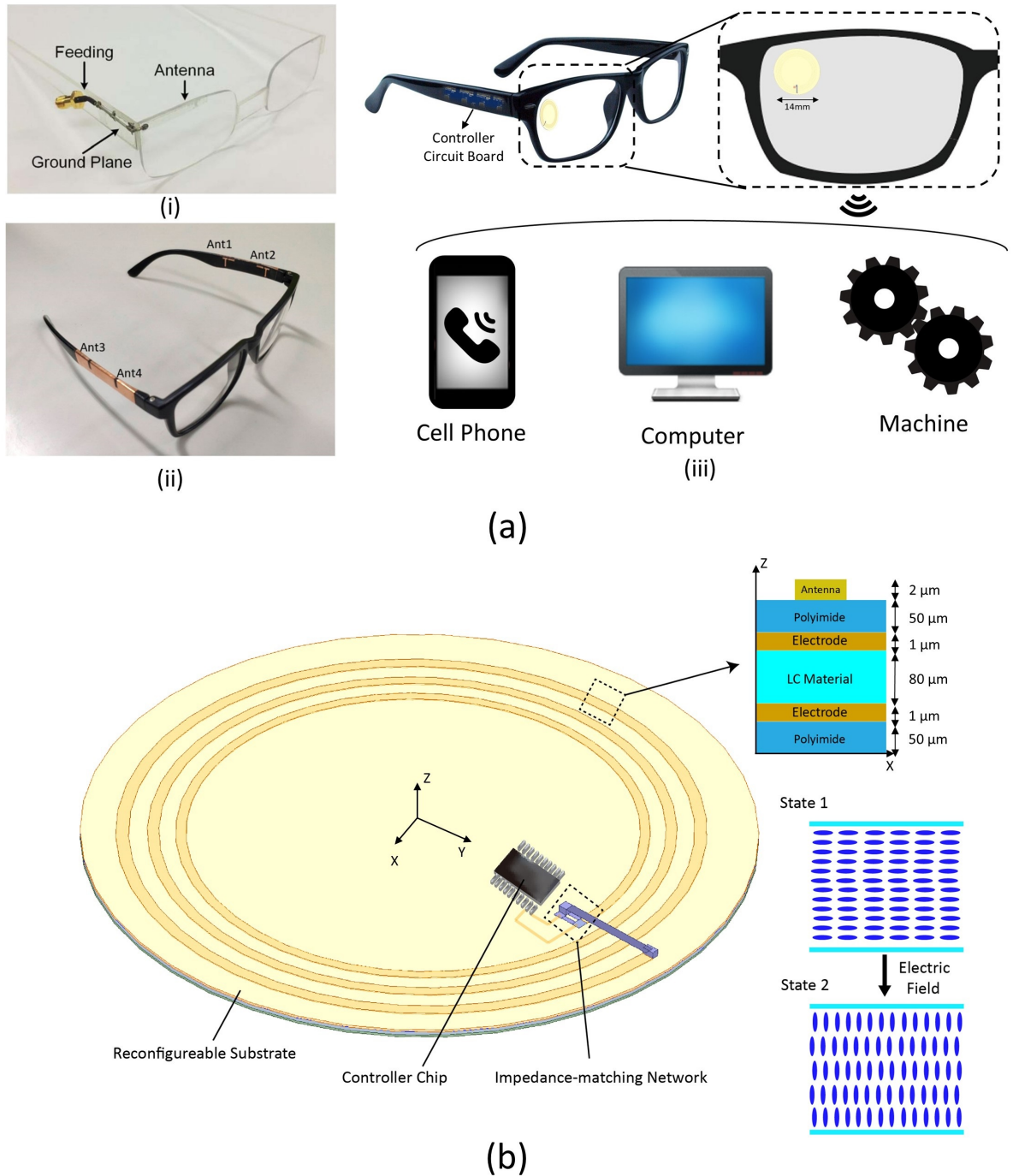
Figure 5.1: (a) (i) and (ii) show previous antenna designs for smart glasses, wherein (i) a transparent antenna is mounted on the lens [217] and in (ii) a patch antenna is mounted on the frame of the glasses [218]. (a) (iii) shows how the proposed antenna could fit on the lens of a smart glass in my design, as well as possible applications of this tunable antenna. (b) Schematic diagram of the tunable antenna and the structure of the reconfigurable layer.

which can reduce the size of the glasses frame without directly blocking the user's view. Here, I proposed a tunable antenna that is integrated into 'intelligent' glasses, where the antenna and the LC substrate are mounted on the glass lens, as shown in Fig. 5.1(a)(iii). According to the literature, antennas mounted on the far edge of the lens can minimize the influence of vision obstruction [217]. Moreover, the proposed design consists of transparent materials to avoid blocking the user's view. Overall, the proposed antenna consists of a dielectric layer, an electrode layer and a LC layer, as shown in Fig. 5.1(b). As previously mentioned, the LC director orientation is influenced by an applied electric field. Therefore, my hypothesis involves 'tuning' the antenna's bandwidth by switching the LC directors from an initial planar state to a state determined by an applied voltage, which leads to a variation of the material's dielectric permittivity [220].

The key design parameters for this technology are therefore to fit the dimensions of typical eyeglass lenses, have high transparency, and operate at a low voltage and with a target frequency. With regard to transparency, previous transparent antenna designs have achieved average antenna transmittance of around 81%, sufficiently high as to avoid impacting a user's vision [217], and in this design, I therefore aim for transparency higher than 80%. Moreover, since high voltages are unacceptable for wearable devices, and where the power supply of smart electronics is usually around 3 to 5 V [221] I aim for voltages lower than 5 V. As is mentioned previously, the 5G network will be used in the future development of most IoT applications [222], so my target is to design and tune the antenna within a 5G frequency band.

In this chapter, I demonstrate a 'proof-of-principle' of using an LC for the design of an antenna with the above design requirements. I use LC and antenna simulations to demonstrate the feasibility of such a device. My results illustrate that the proposed tunable antenna could be driving with 0.4 to 0.6 V and cover the section of the 5G communication frequency range from 3.3 to 3.8 GHz, which both more than adequately satisfy the design

criteria for wearable applications. Apart from communication applications, the tunable antenna could also be applied to harvest energy from within the 5G frequency range. In comparison with previous designs, this design has a smaller footprint, thinner substrate material and lower driving voltage, which is more suitable for wearable applications.

5.2 Methodology

To realize the controllable antenna, I proposed a multi-layer substrate with a sandwich structure consisting: dielectric layers, grid electrodes, LC material and alignment layers. The dielectric layer, typically PI, protects the user's eyes from the electric field. A transparent electrode layer consisting of indium tin oxide (ITO) was used, as well as a planar alignment layer, which can be achieved by rubbing the PI layer in one direction, creating microgrooves along which the LC aligns [223]. Moreover, the LC cell thickness can be fixed through the use of SiO_2 micro-spheres spacer within the LC layer.

In Table 5.1, I list four commonly available NLC materials and mixtures. When choosing the NLC material for this application low LC driving voltages are needed to ensure device safety and portability, and therefore LCs with high $\Delta\varepsilon$ and low K_{11} are more suitable for low-power applications. Furthermore, relatively low splay, twist and bend elastic constants (K_{11}, K_{22} and K_{33}) are required to reduce the device response time. Based on these considerations, RDP-84909 (DIC cooperation) was chosen as the most suitable LC material.

Table 5.1: Material parameters for the LCs considered during this study [224–230]. The parameters for RDP-84909 are provided by DIC Corporation, Japan.

Parameter	5CB	BLO48	RDP-84909	E7
Clearing temperature, $T^{NI}(°C)$	35	100	91.7	59.85
$\varepsilon_\perp$	6.9	5.2	8	5.17
$\Delta\varepsilon$	11	16.9	39.1	14.37
n_o ($\lambda = 532\,nm$)	1.532	1.573	1.48	1.53
Δn ($\lambda = 532\,nm$)	0.174	0.226	0.1464	0.22
K_{11} (pN)	6.4	15.5	4.6	11.2
K_{22} (pN)	3	12	1.2	6.8
K_{33} (pN)	10	28	13.8	17.8

A spiral antenna was chosen since it is a commonly used antenna geometry in wearable applications, due to its simplicity, universality and low-cost [231, 232]. My antenna was designed for 5G applications, where I chose n78 from frequency range 1 (FR1) of the 5G mobile network, i.e., 3.3–3.8 GHz [233]. The electromagnetic waves in this range are defined as centimeter waves. Due to their small wavelength, centimeter waves could be received in narrow beams, which is suitable for data linking, point-to-point communication and radar applications.

As is shown in Fig. 5.1(b), a copper-based single-armed Archimedean spiral coil was chosen for its typical wide bandwidth and circular polarization, and impedance matching was used due to the geometry limitation. The thickness of the antenna is $2\mu m$ and the width is 200 μm. In comparison with a traditional patch antenna, the single-armed Archimedean spiral coil design has less antenna area, which can reduce vision obstruction. A matching parallel capacitor was used to adjust the antenna to the desired resonant frequency with maximized power delivery, using equation [234]:

$$f = \frac{1}{2\pi\sqrt{L_s C_p}} \tag{5.1}$$

Where L_s is the equivalent inductance of the spiral antenna and C_p represents the total capacitance of the device. Finite element analysis was carried out with High Frequency Structure Simulator (HFSS) software, where the Archimedean spiral geometry was defined as: $r = r_\theta + \alpha\phi$, where $r_\theta = r_0$ and $r_\theta = r_1$ are the inner and outer radii of the starting circle, α is the growth rate of the spiral arm, ϕ denotes the angle or the arc value, and the spiral lines were defined as $x_t = r_\theta e^{\alpha t} \cos t$, and $y_t = r_\theta e^{\alpha t} \sin t$. The specific parameters of antenna were defined as follows: $\alpha = 17.5\,\text{mm}$, $\phi = 6\pi$, $r_0 = 4.5\,\text{mm}$, $r_1 = 4.7\,\text{mm}$, $C = 0.8\,\text{pF}$. Copper elements define the inductance of the spiral coil and the gaps between generate the equivalent capacitance of the device.

The surface current distribution presented in Fig. 5.2(a) indicates the current flows on the antenna surface, which is restricted by the spiral geometry. Additionally, the induced electric field indicates a higher concentrated electric field intensity on the intermediate spirals. The Specific Absorption Rate (SAR) simulated was constrained to $0.8538\,\text{W/kg}$ as is shown in Fig. 5.2(b), which is within the safety regulation standard ($2\,\text{W/kg}$). [235]. The radiation patterns for two different LC states are demonstrated in Fig. 5.2(c). The reflection coefficients (S11) are -15.8 dB and -20.8 dB when ε equals to 8 and 47.1 respectively. Additionally, the radiation pattern is slightly changed with two different dielectric permittivity, which showcases that the propagation direction of the antenna is stable as the LC substrate is switched.

Grid electrodes were chosen on both the top and bottom electrode layers rather than plate electrodes since the latter would reflect electromagnetic waves and prevent them from reaching the reconfigurable LC layer. In Fig. 5.3(a), a top-bottom grid electrode array with $1\,\mu\text{m}$ width and $49\,\mu\text{m}$ gap (2% of grid density) were simulated using the **Q**-tensor theory described above. The grid electrodes have similar performance (in terms of electric field intensity and direction) to plate electrodes and, consequently, the LC molecules exhibit similar behavior with each type of electrode. The transmittance of the

(a)

(b)

(c)

State 1: ε=8   State 2: ε=47.1
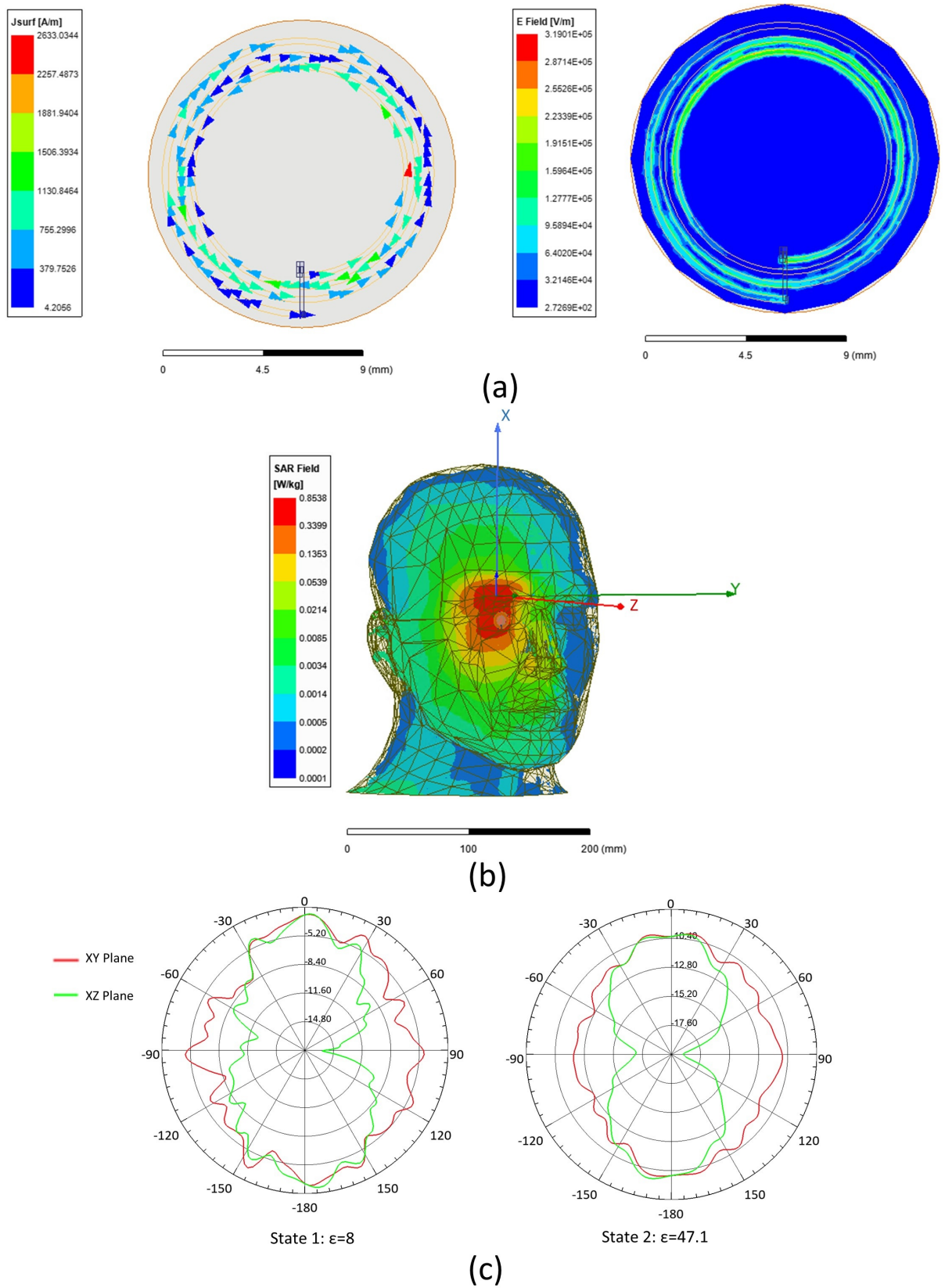
Figure 5.2: (a) The surface current density on the antenna and the electric field intensity on the top surface when the LC director is planar aligned ($V = 0$). (b) Specific Absorption Rate (SAR) simulation, demonstrating that the antenna is safe for near-eye operation. (c) The radiation pattern for two different LC states.
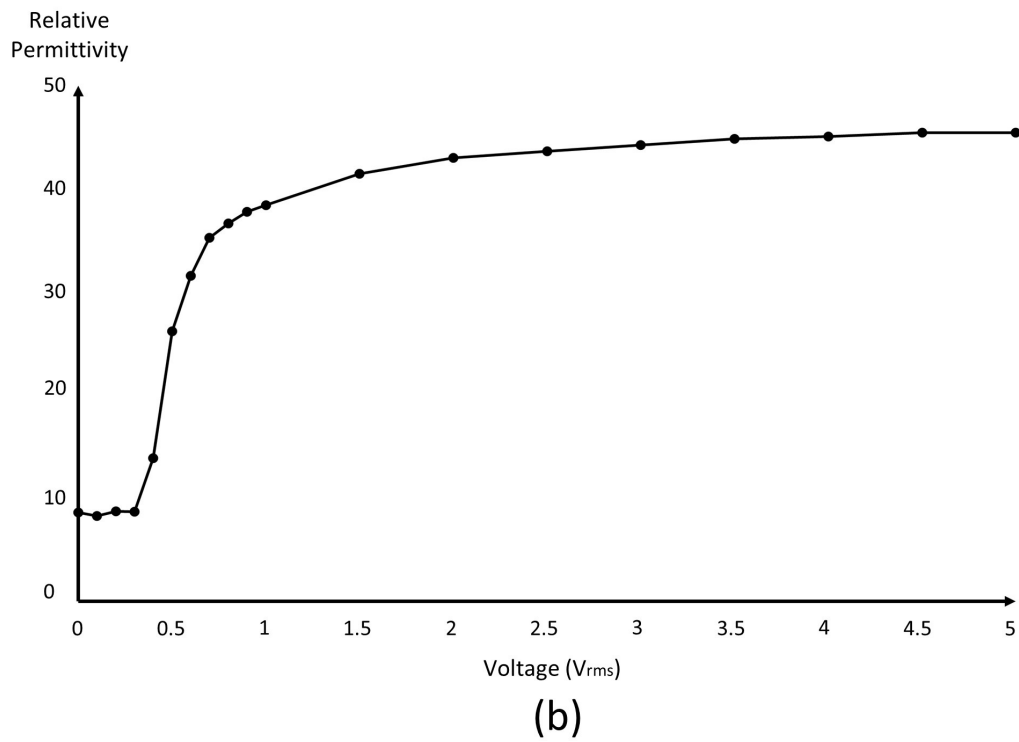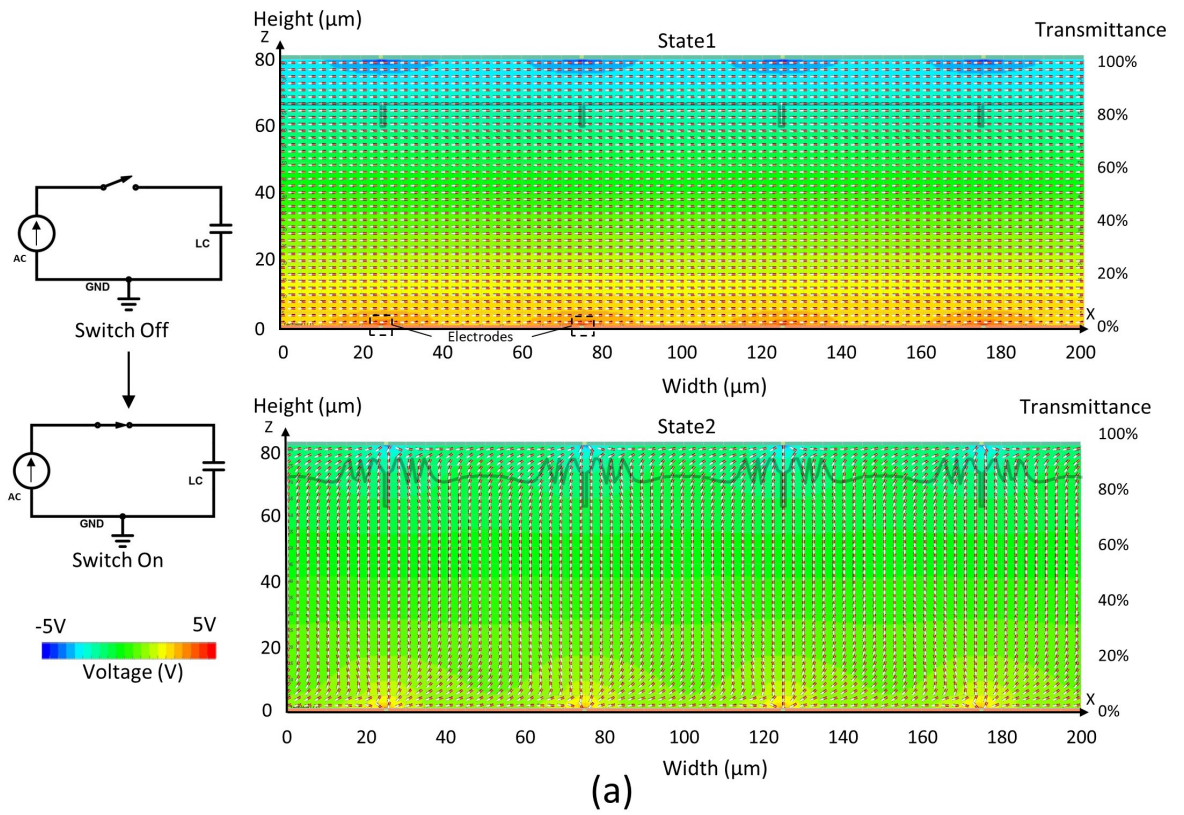
Figure 5.3: (a) The electrode structure and **Q**-tensor simulation results of the LC layer. The LC substrate can be switched from state 1 to state 2. (b) Plot of the Freedericksz curve for RDP-84909.

cell was then calculated using the 4x4 Berreman matrix method described above and is also shown in Fig. 5.3(a). The transmittance throughout the cell is between 91% to 74%. The lowest transmittance occurs where the electrodes are located and therefore the LC cell with grid electrodes would have a higher average transmittance than plane electrodes.

The threshold voltage required to tilt the LC directors from planar towards the vertical can be determined using [115]:

$$V_c = \pi \sqrt{\frac{K_{11}}{\varepsilon_0 \Delta \varepsilon}} \tag{5.2}$$

Which shows that the cell thickness does not affect the threshold voltage. Although a thick cell will result in a relatively long response time [206], thicker LC cells will have a more significant frequency bandwidth variation from switching the director configuration of the LC substrate. In this case, thicker substrates lead to wider antenna tuning frequencies. Therefore, to ensure both high tunability and low response time, the thicknesses of the LC and PI layers were set to $80\,\mu$m and $50\,\mu$m, respectively.
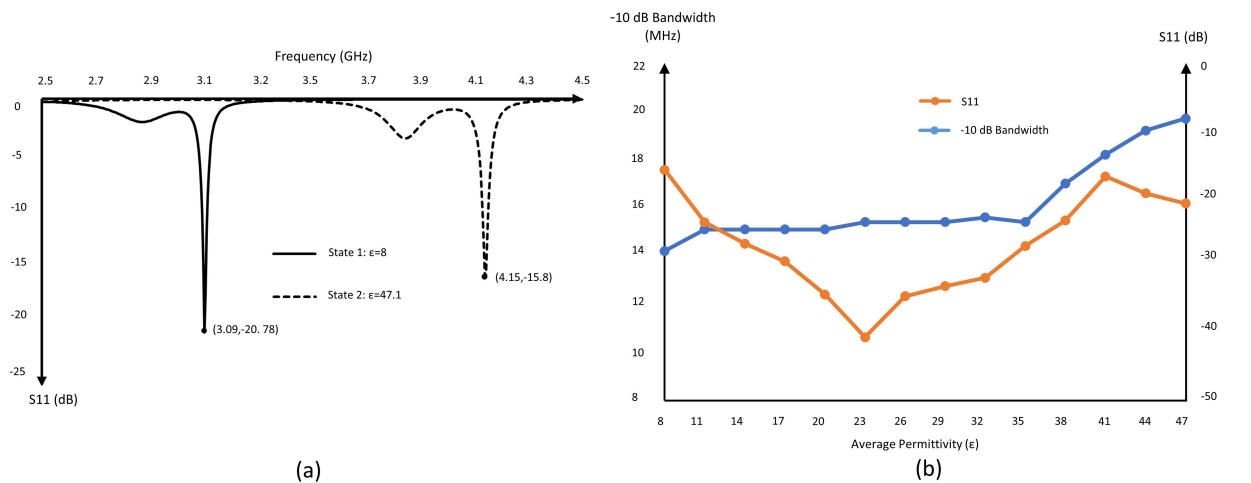
Figure 5.4: (a) Plots of the S11 parameter of the antenna when the substrate is in two different states. This figure shows the theoretical maximum tunability. (b) Plots of S11 and -10 dB bandwidth when the permittivity of the LC layer varies from 8 to 47. Therefore, the antenna could operate with the proposed variation of substrate permittivity.

5.3 Results and Discussions

As mentioned previously, to reduce the response time, the antenna was mounted on a 180 μm reconfigurable substrate. Assuming a relatively weak anchoring effect, all LC directors can be assumed to have planar and homeotropic alignment in state 1 (no applied voltage) and state 2 (with applied voltage), respectively. In this case, the theoretical maximum tunable frequency range can be calculated. For the LC material RDP-84909, the permittivities of the two states are 47.1 and 8, respectively, and therefore the maximum frequency shift is from 3.09 to 4.15 GHz (Fig. 5.4(a)), which is in the centimeter wave range.

In practice, due to the anchoring effect of the PI layer on the LC, the directors in contact with the edge of the alignment layers tend to maintain their original orientation. Thus, when a voltage larger than the threshold voltage is applied to the cell, the average permittivity of the cell will be smaller than $\varepsilon_\parallel$. In future works, the average capacitance between electrodes could be calculated using the simulation software TechWiz. Hence, the relative permittivity could be calculated with various input voltages. However, using the model in this work, in Fig. 5.3(b) the average permittivity is plotted against voltage, known as the Freedericksz curve, and shows a sharp rise of relative permittivity around 0.35 V, which is in agreement with the theoretical threshold voltage of RDP-84909 calculated as 0.362 V. Moreover, the permittivity increases significantly between 0.35 and 1 V, where the permittivity varies from 8 to 38.4. The relative increment of permittivity decreases after 2 V. According to the Freedericksz curve, for significant changes to the permittivity, it is possible to operate the reconfigurable substrate within a relatively small voltage range, between 0.35 to 1 V is preferred, an ideal range for wearable applications.

Simulations were then performed to obtain the relationship between LC substrate permittivity found through the Freedericksz curve, and the resonant frequency. In the antenna model, the substrate contains a dielectric layer and an LC layer, where I set the permittivity of the LC layer as variable, and thus obtain the frequency shift in response to this variation of permittivity. As is shown in Fig. 5.4(a), when the average permittivity of the substrate is increased from 8 to 47.1 (I neglect the anchoring effect to achieve maximum permittivity), the resonant frequency is shifted from 3.09 to 4.15 GHz, successfully covering the target frequency range n78 (3.3 to 3.8 GHz). The corresponding average permittivity varies from 14 to 32. Moreover, I also obtained -10dB bandwidth versus different permittivity, as is shown in Fig. 5.4(b). This curve illustrates that the -10dB bandwidths are within the range of 14.2 to 19.7 MHz, which can ensure the data transmission is taking place efficiently and at an acceptable speed.

Combining the Freedericz curve and the relationship between applied voltage and resonant frequency, shown in Fig. 5.5(a) I obtain the relationship between the applied voltage and the resonant frequency, as shown in Fig. 5.5(b). This figure plots the applied voltage from 0 to 3 V, since the antenna is designed for wearable applications, and shows that when the voltage is varied the resonant frequency varies from 3.09 to 4.15 GHz. As mentioned previously, the target frequency range of this antenna design is from 3.3 to 3.8 GHz which is covered when the voltage is between 0.4 and 0.6 V, which is suitable for low power consumption wearable applications.

Table 5.2: Comparisons with previous work

Reference	Antenna Type	Antenna Area (mm^2)	Frequency Range (GHz)	Driving Voltage (V)	Thickness of Substrate (μm)
[236]	Patch Antenna	1026.4	2.532 - 2.427	25	787
[237]	Patch Antenna	0.225	85 - 115	20	1020.2
[206]	Patch Antenna	400	4.84 - 5.12	-	300
[238]	Patch Antenna	612	2.02 - 2.4	-	500
[207]	Patch Antenna	434.7	2.7 - 2.9	-	500
My Design	Spiral Antenna	6.8	3.09 - 4.15 Target: 3.3 to 3.8	0.6	180
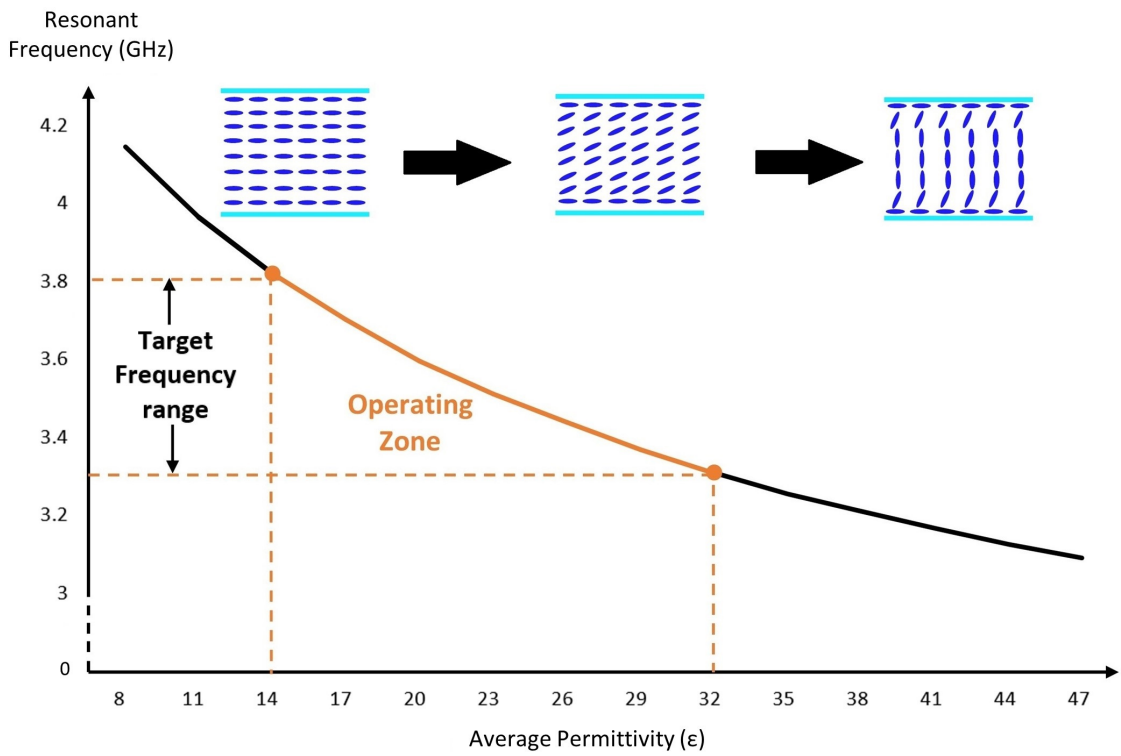
(a)
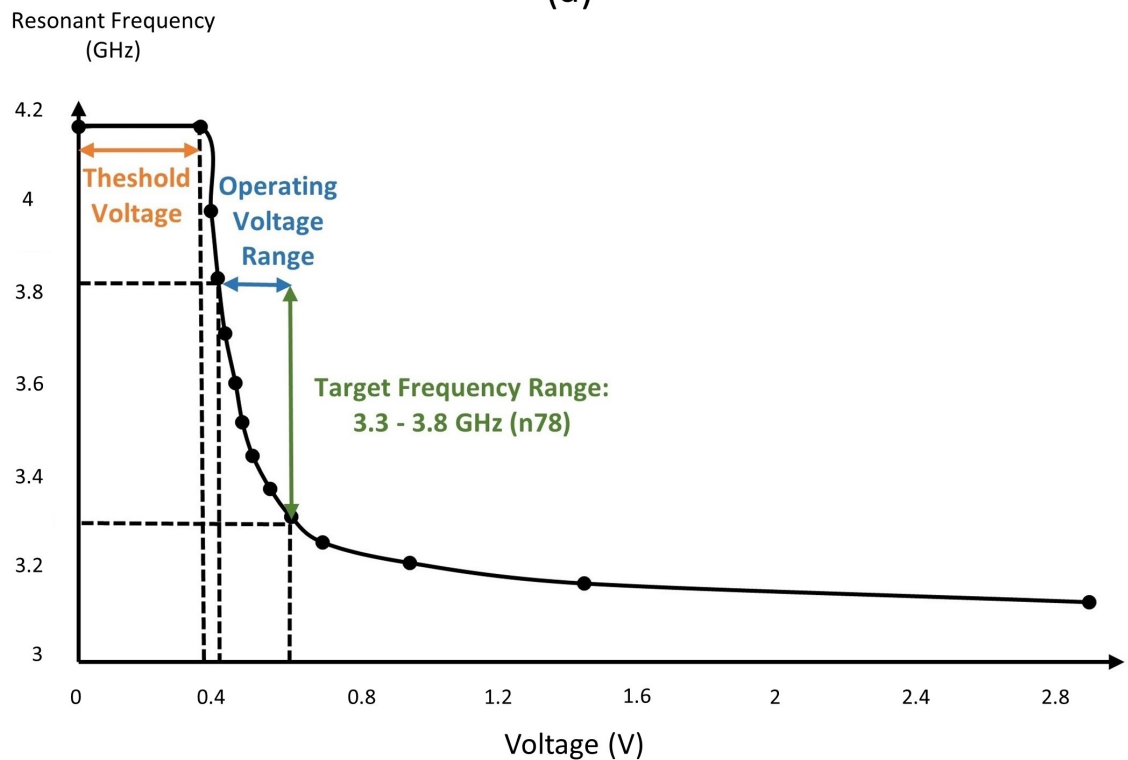
(b)

Figure 5.5: (a) Average permittivity versus resonant frequency. This plot demonstrates that the antenna could cover the target frequency range (n78: 3.3-3.8 GHz). (b) Plot of resonant frequency versus applied voltage. The driving voltage required to cover the target frequency ranges from 0.4 to 0.6 V.

In Table 2, the specifications of my antenna are compared with previous tunable antenna designs. The table lists important parameters for assessing the performance of the tunable antenna including antenna type, area, frequency range, driving voltage and substrate thickness. Noticeably, the driving voltage stands for the voltage to tune the LC substrate. It is clear that my tunable antenna design has a smaller footprint, thinner substrate material and lower driving voltage compared to other designs, and could potentially be used for wearable or implantable applications.

5.4   Conclusion

In this chapter, I have proposed a tunable centimeter wave antenna design for smart glasses applications. The antenna could be tuned from 3.3 to 3.8 GHz (FR1 n78 for 5G communication) using 0.4 to 0.6 V. The theoretical maximum tunability of this design is 1.06 GHz (3.09-4.15 GHz), which could be achieved only when the anchoring effect is neglected. Compared with previous designs, this antenna has lower driving voltage, smaller area and high tunability. This prospective design is suitable for wearable and implantable devices. The low driving voltage could allow this tunable antenna to be used in low-consumption and autonomous devices. The small area of the antenna could also enable its integration within a miniaturised design and its high tunability means that it can cover more frequencies and communicate with a wider range of devices compared to currently available designs.

Further work will focus on fabricating the antenna and developing the driving electronics for the reconfigurable surface. To fabricate the antenna pattern, laser printing or lithography techniques can be used, and glass spherical spacers would be used to control the thickness of the LC cell. The structure of the antenna and LC material will also be optimized to cover a wider bandwidth. Following this, the intention is to embed this antenna within a smart glasses system to expand the bandwidth allowing communication with multiple external devices, which will be of considerable benefit for IoT applications.

Chapter 6

Cholesteric Liquid Crystal Based Reconfigurable Optical Combiner for Head-Mounted Display Application

Recent advancements in Head-Mounted Displays (HMDs) showcase their potential to replace traditional displays such as LCDs and OLED screens. The upcoming generation of HMDs necessitates a seamless transition between AR and VR modes. In this chapter, I introduced an innovative CLC-based optical combiner for HMDs. This approach enables the display device to switch between AR, VR and transparent modes via temperature modulation. Since CLC materials demonstrate varying optical properties at different temperatures, I integrated a real-time temperature monitoring system that was paired with an external controller. This allowed for dynamic temperature adjustments of the optical combiner and enabled smooth transitions between display modes. Furthermore, I used the Berreman 4x4 matrix method to simulate the optical properties of the optical combiner, finding strong agreement with the experimental results. I explored the performance of the tunable optical combiners using 450, 532 and 635 nm laser sources. My findings demonstrate that CLC-based optical combiners can effectively switch between the three distinct modes at corresponding temperatures, paving the way for versatile applications in future HMDs.

6.1 Introduction

In recent years, tremendous advances in HMDs have made a significant improvement in the degree of HMI. HMDs include VR, AR and Mixed Reality (MR) technologies [239]. Specifically, VR allows users to experience and interact with a virtual 3D environment. To achieve this, users typically wear a VR headset that completely covers their field of view and often incorporates motion-tracking sensors to enable realistic interactions. With VR headsets, users can be fully immersed in the virtual world as their physical surroundings are completely blocked [240, 241]. AR overlays digital content onto the real world. Instead of replacing the real environment, AR headsets enhance it by adding computer-generated images, information and objects. AR headsets can mix the virtual and real worlds, which means that users can interact with virtual elements while still being aware of the real environment [242, 243]. MR refers to a mixture of VR and AR. In MR devices, virtual objects can interact with the real environment, where the user can interact with both real and virtual elements simultaneously. This blending of virtual and real-world elements enables a more immersive and interactive experience. Devices like Microsoft's HoloLens are examples of MR technology, offering a combination of VR and AR capabilities [244]. As technology progresses, the boundaries between VR, AR and MR may become more fluid. These technologies are all related to different forms of immersive technologies that blend the digital and physical worlds.

(a) (b) (c)
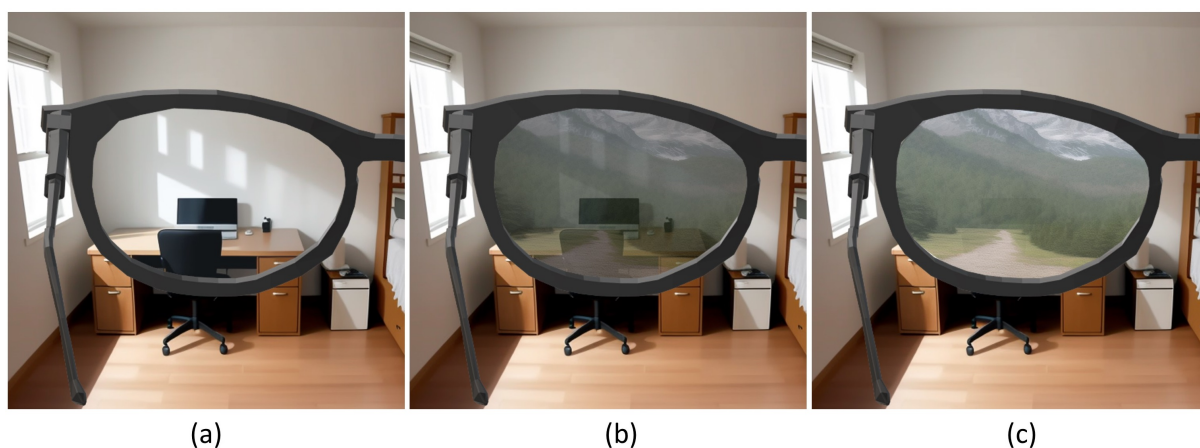
Figure 6.1: Futuristic XR glasses: Seamless transition between (a) Transparent mode, (b) Augmented Reality mode and (c) Virtual Reality mode.

Despite the notable progress in AR, VR and MR technology, it is still a challenge to switch between VR, AR and MR modes. Recently, most HMD devices have been designed to prioritize VR, AR and MR experiences. Therefore, users often need to switch between different devices or different applications to switch between VR, AR and MR modes [245]. The lack of smooth and uninterrupted transitions can adversely affect the user experience and hinder the seamless integration of virtual and real-world content. As AR and MR technologies both enable users to engage with a real environment, they have similar hardware requirements. In Table 1, I summarize three popular AR NED solutions that have been widely applied to industrial products. The prism solution used a reflective surface to project virtual images onto a glass lens [246, 239]. Compared to other AR glasses, the prism solution has limited FOV due to its optical design. Optical waveguide technology is a widely used AR solution which utilizes waveguide components to reflect light inside glass lenses and project virtual images to the eye [247]. Waveguide system enables pixel dots to be projected to different areas as the user moves the eye, leading to large FOV and high resolution. Despite large FOV and high resolution, lumination loss occurs during the incident light coupling and transmission in the waveguide. Additionally, chromatic aberration occurs as different wavelengths of light have different refractive indices and different propagation angles within the waveguide, which cause color distortion of the imaging system[248]. The freeform solution is another popular solution, which involves designing and manufacturing curved reflective optical surfaces, for example, birdbath optics, to achieve NED [249, 250]. Freeform AR glasses provide large FOV and good image quality. However, they have relatively thick lenses and low transparency due to the optical design. According to the survey, different AR solutions have their own advantages and disadvantages, and none of them could seamlessly switch between VR mode and AR (MR) mode.

Among these AR imaging systems, Optical combiners (OCs) play an important role in merging a virtual image with the real environment. In this chapter, I proposed a novel liquid-crystal-based OC that could be able to switch a HMD device between VR mode, AR (MR) mode and normal mode, as is shown in Fig. 6.1. Noticeably, Transparent mode

Table 6.1: State-of-the-Art of AR Imaging Solutions

Solution	Representative Product	Pros	Cons
Prism Solution [246, 239]	Google Glass	Low-cost, Lightweight	Obstruct Vision, Small FOV
Waveguide Technology [248, 247]	HoloLens, Magic Leap	Large FOV, High Resolution	Low Brightness, Chromatic Aberration
Freeform Solution [249, 250]	Nreal Light, Epson BT300	Large FOV, High Resolution, High Contrast	Bulky Optical System, Thick Lenses

means the OC demonstrates maximum transmittance and allows most light to go through the glass lens, which acts like a normal glass lens without obstructing any view. In traditional VR glasses, the imaging system is placed in front of the eye to generate a virtual image to achieve NED. The AR and MR glasses require an OC to combine virtual images with a real environment. In this case, if the transparency of OC could be manually controlled, it is possible to switch glasses from VR mode to AR or AR mode. To achieve this, CLC is introduced as a reconfigurable OC to display the item to the eye.

LCs exhibit properties of both liquids and crystalline solids, which have similar properties to crystals but are also able to flow like liquids. LC molecules have rod-like structures, whose behavior can be controlled by temperature, magnetic field and electric fields [70]. CLC is a type of LC material that exhibits a helical structure, which results in unique electric and optic properties, such as selective reflection. The selective reflect wavelength of a CLC cell is determined by pitch length, where pitch length stands for the distance it takes for the helical structure to complete one full twist [104]. Specifically, when incident light interacts with the helical structure of the CLC material, the light waves that match the pitch of the helix have constructive interference and are reflected back in a specific direction, which is known as selective reflection, also called Bragg reflection. CLCs can be obtained by mixing a chiral dopant with nematic LC material, which introduces chirality to the nematic LC molecules, resulting in the cholesteric phase. The pitch length of CLC materials is influenced by several factors, such as the temperature and concentration of the chiral dopant [115].
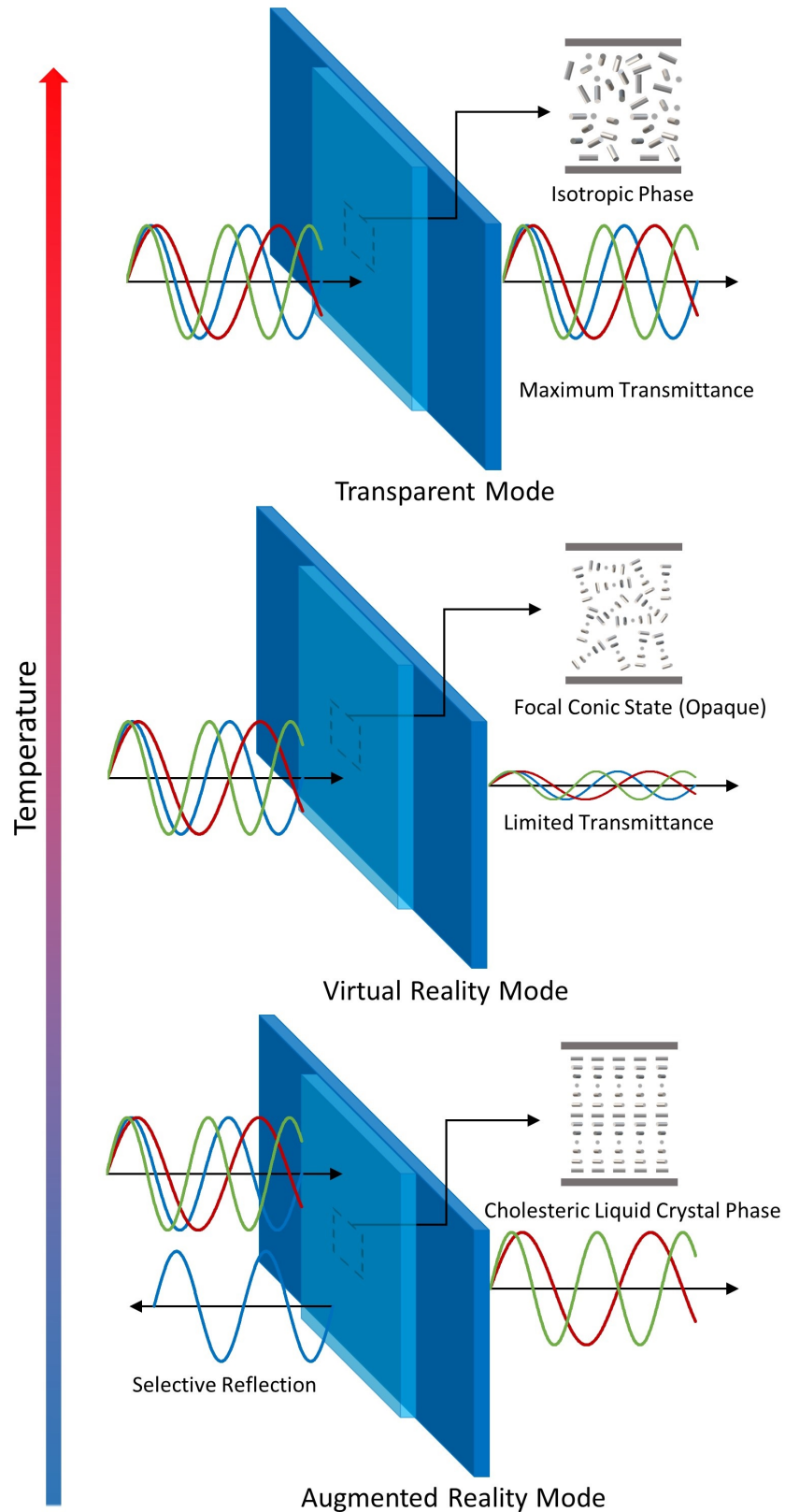
Figure 6.2: This figure showcases how light waves and LCs would be influenced as temperature rises. It also demonstrates how the OC could be switched between AR, VR and transparent mode on a physical level.

The relationship between CLC material and temperature is detailed explained in Fig. 6.2. Generally, if the temperature of a CLC material is above its melt point and lower than the clear point, it is in LC phase and exhibits selective reflection. In this temperature range, users are able to see both virtual images and real environments at the same time, so the OC is in AR mode. As the temperature further increases to the clear point, the LC is not fully transformed into an isotropic phase, where the disruption of helical structure can scatter or absorb light. Therefore, the transparency was reduced and the cell became cloudy, which is known as the focal conic state. In this scenario, the real environment was blocked and the user could only see the virtual image, so the OC is in VR mode. Furthermore, when the temperature is above the clear point, the helical structure of the CLC material will be fully destroyed and become the isotropic phase, where the LC molecules have a random orientation and behave as a liquid. Thus, the selective reflection property disappears and the CLC cell becomes fully transparent, which is transparent mode. Accordingly, a temperature controlled CLC based OC have the prospect of being applied to the next generation of HMDs to achieve a seamless transition between VR mode, AR mode and normal glasses.

According to previous research, CLC materials have been applied to OC film to enhance image quality in AR applications, for example, AR glasses [251, 252] and head-up display [253, 254]. However, the photoinitiator material is mixed with CLC material during the process. After photoinitiator material is exposed to UV light, it forms a polymer network, which can fix the LC molecules in a particular orientation. This process could stabilize the CLC film and fix the selective reflection wavelength, which can ensure that the reflect wavelengths are not influenced as a result of temperature variation. In this case, a reconfigurable CLC-based OC is required to be tuned as the temperature changes, and thus the CLC molecules should not be fixed. Temperature controlled CLC cells have been investigated in previous research [255, 256]. On the basis of previous research, the correlation between voltage and the temperature of the CLC cell has been explored, as well as the link between voltage and the center frequency of the reflective band. However, the mapping relationship of voltage and reflect wavelength is not rigorous. The influence of

environmental temperature on the LC cell cannot be ignored, which might introduce a systematic error. In this chapter, I designed a temperature control system on a CLC cell to monitor and control the CLC temperature in real-time. With the system, the reflection waveband of the CLC cell could be controlled via Bluetooth; hence, users can manipulate the OC transmittance and switch different display modes on AR glasses.

6.2   Methods

6.2.1   Mathematical Modeling

Berreman 4×4 matrix is a mathematics tool to simulate the optical behavior of anisotropic materials, such as the CLC cell. As an extension of the Jones matrix, this optical calculation could calculate the transmission and reflection of light through more complex multilayer structures [257]. Specifically, Berreman 4×4 matrix includes consideration of multiple reflections of the electric and magnetic waves between layers, hence Bragg reflection could be simulated. According to the previous survey, three types of light engines are commonly used in AR technology, including Liquid Crystal on Silicon (LCoS), Laser Beam Scanning (LBS) technology, and OLEDs [258]. Each pixel in these light engines is made up of red, green and blue (RGB) subpixels. In order to design an OC to project the virtual image to the eye, three CLC layers need to be fabricated and cascaded to reflect RGB light. Here, I simulated CLC material with different pitch lengths in order to reflect RGB light with center wavelength at 470, 520 and 620 nm.

Because of the anisotropy of LCs, LC materials have two refractive indexes along and perpendicular to the LC director, which are n_e and n_o, respectively. The central wavelength and bandwidth of Bragg reflection can be determined by the refractive indexes and pitch length [259]. Notably, the average refractive index can be calculated by:

$$n^2 = \frac{(n_e^2 + 2n_o^2)}{3} \tag{6.1}$$

In this work, nematic LC material E7 was used as the host material to prepare CLC material, thus the simulation was based on the parameter of E7. The refractive index of E7 n_o and n_e is 1.53 and 1.75 respectively [196]. This allows us to calculate the central wavelength and the bandwidth of Bragg reflection at normal incidence, which are

$$\lambda_{central} = nP \tag{6.2}$$

$$\Delta\lambda = \Delta nP \tag{6.3}$$

where n is the average refractive index and P is the pitch length. In this case, the target pitch length of RGB cells is 392, 333 and 280 nm respectively. Additionally, the bandwidth of the Bragg reflection can be calculated by pitch length, which are 85.8, 73.3 and 61.6 nm of RGB cells respectively. The bandwidth is sufficient to cover the spectrum of RGB light of different light engines, thus it can be used as OC film in AR applications. The transmittance of the CLC cell at different wavelengths was then simulated using the 4×4 Berreman matrix method, with the cell thickness being 6 μm. The simulation result will be demonstrated and further analyzed in the result section.
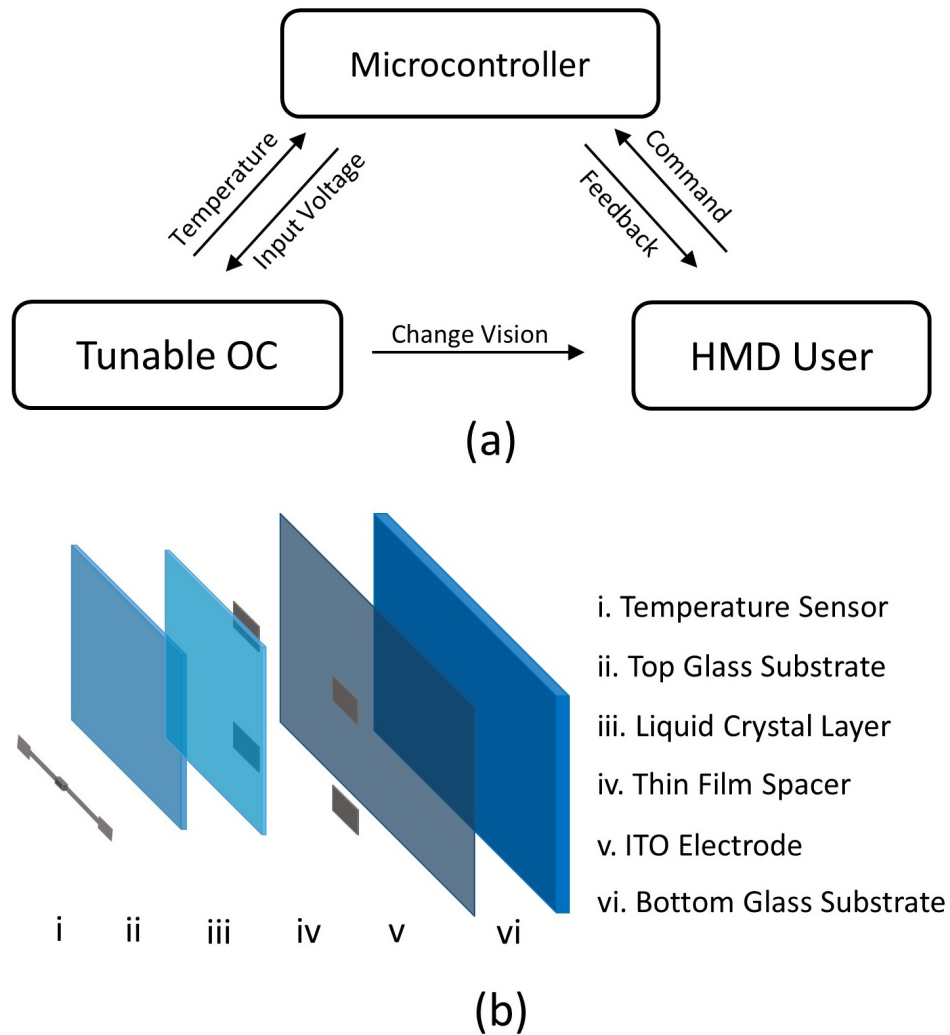
Figure 6.3: (a) Block diagram of the system. (b) Detailed structure of a single-layer tunable CLC-based OC.

6.2.2 System Design

A real-time temperature control system was proposed to switch different modes of CLC glass lenses. Fig. 6.3 a shows the relationship between tunable OC, microcontroller and HMD user. The closed loop demonstrated the basic theory of the tunable OC system. The CLC glass lens was made of indium tin oxide (ITO) coated glass, CLC material and cover glass, as is shown in Fig. 6.3 b. Specifically, a DC voltage source was added to an ITO-coated glass to generate heat. A negative temperature coefficient (NTC) thermistor was mounted on a thin cover glass to monitor the temperature variation in real-time. The purpose of using cover glass rather than a normal glass slide was to reduce the influence of

heat dissipation in the glass layer, so that the thermistor was closer to the LC layer, thus having a faster response to temperature change. The temperature of the glass lens could be then read out by an external microcontroller. After that, the microcontroller generated a control signal to a metal oxide semiconductor field-effect transistor (MOSFET) to change the voltage between the ITO glass. MOSFET was used to isolate potential large currents on ITO glass with the microcontroller. Additionally, the PID algorithm was applied to the system to dynamically control the temperature, which can increase the stability and accuracy of the control system. This system could be powered by a 3.7 V lithium battery. Moreover, the system could interact with external devices via Bluetooth, so that the user could switch the display mode of the HMD by giving instructions on the mobile phone or computer. The whole system could be integrated into a 2×5 centimeter Printed Circuit Board (PCB) and placed on eye-glass frame.

6.2.3   Preparation of CLCs

According to calculation, the OC films require CLC materials with 392, 333 and 280 nm pitch lengths. To prepare these materials, nematic LC material E7 and chiral dopant were mixed with different proportions. Researchers have studied the relationship between different concentrations of S811 and pitch length [255, 260]. Specifically, the pitch length of a CLC material with certain considerations varies as temperature changes in the LC phase range. Therefore, three different CLC materials to reflect RGB light are required to have 392, 333 and 280 nm pitch lengths at the same temperature. In this case, 23%, 28% and 30% w.t. S811:E7 mixture are able to reflect RGB light respectively at $32\,°C$. To prepare CLC materials, E7 and S811 were mixed in $50\,°C$ with a magnetic stirring rod for five minutes, 500 rpm. Subsequently, 50 μL CLC material was dropped on a glass slide and covered with 22×22 mm cover glass at $50\,°C$, which can ensure cell thickness

around 10 microns. Noticeably, this step was to verify the reflection properties of CLCs, where precise control of LC cell thickness was not required. Normally, CLC cell thickness of more than 10 pitches could lead to a broad reflection band and well-reflect intensity, which is ideal for assessing the optic properties of the material [104].

6.2.4 Fabrication of CLC cell

In order to monitor the temperature of CLC in real-time, a thermistor is required to be mounted on top of the cover glass to build a real-time sensing system. The thickness of the cover glass is 100 μm, which can reduce heat dissipation during transmission through the glass and thus reduce the response time. Firstly, the thermistor was fixed on the cover glass via optic adhesive (NOA68) and cured via UV light for 10 minutes. After that, wire bonding was required to establish the connection of the thermistor. Therefore, silver paint was printed on the cover glass via a shadow mask. Subsequently, the temperature of the cover glass could be read out by a voltage divider circuit. Furthermore, a calibration process was performed to establish a mapping between temperature and output voltage.

The following process was to fabricate a CLC cell. Firstly, an ITO-coated glass was used as a substrate, where a 200 nm PMMA was deposited as an alignment layer. After that, the alignment layer was mechanically rubbed in a specific direction via velvet cloth or soft bristle brush to create alignment grooves. Notably, the pitch length varies during the operation period. If alignment layers are on both sides of the cell, the orientation of the LC molecules on each side may conflict with each other, which will result in deformation and discontinuation of the helical structure of CLC material. Subsequently, the defects in CLC cell would influence optical performance, hence, it is advisable to have only one alignment layer. After the deposition of the alignment layer, Mylar film spacers were placed at each corner to control the thickness of the CLC cell. Specifically, 6 μm spacers were chosen since the cell thickness was over 10 pitch lengths of each CLC material.

6.3 Results and Discussion
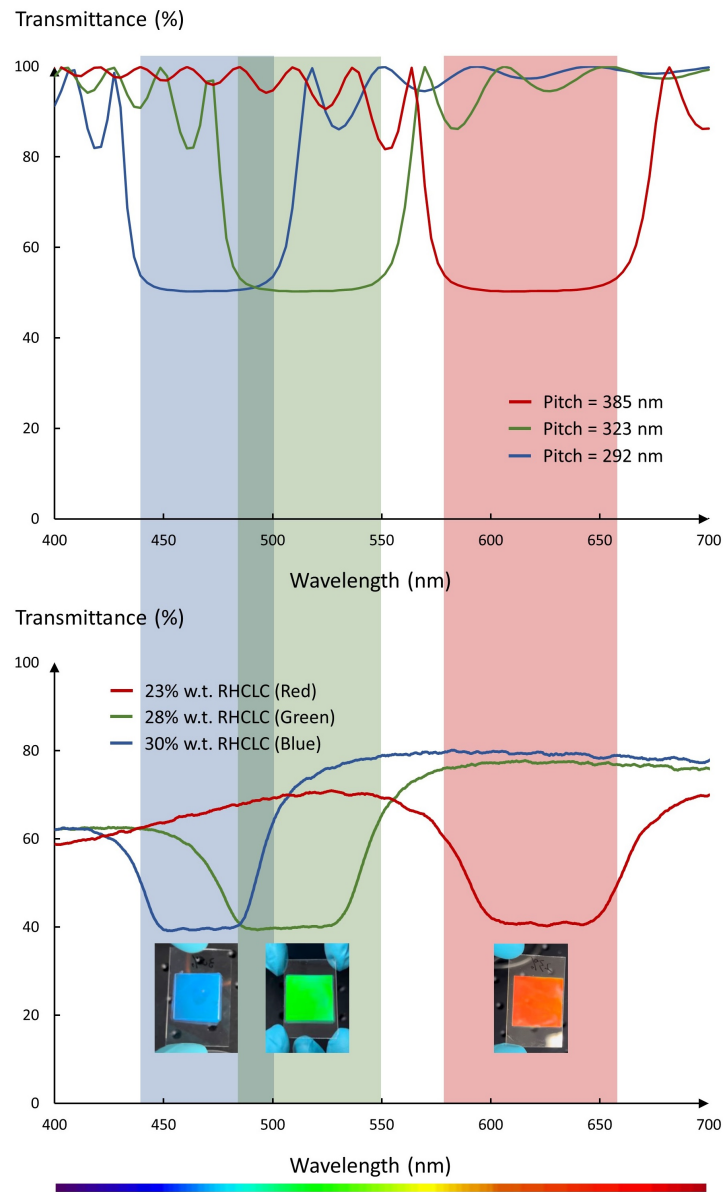
Figure 6.4: This figure demonstrates the simulation result of CLC cells with 292, 323 and 385 nm pitch lengths. Additionally, the simulation results are mapped with experimental results of three different concentrations of CLCs at $32\,^{\circ}\mathrm{C}$ to showcase that the CLC cells are able to reflect the target wavelength of light at 470, 520 and 620 nm.

The simulation results of CLCs with central reflection wavelength at 470, 520 and 620 nm are demonstrated in Fig. 6.4. In addition, the reflection band of 23%, 28% and 30% w.t. CLC cells were measured at $32\,^{\circ}\mathrm{C}$ by a spectrum analyzer, which demonstrated good consistency with simulation results. Noticeably, transmission mode was used to characterize CLC cells, since it is more straightforward to extract information about the CLC properties. With the reflection mode, the reflection introduced by glass substrates and

interference effects might result in a complex spectrum. Additionally, the results were supposed to showcase that the OCs were able to block RGB light in the environment thus increasing the contrast of the AR system. According to the result, the three different CLC cells exhibited selective reflection at RGB light respectively at 32 °C. It is noticeable that the experiment result has lower transmittance than the simulation result because the experiment result demonstrated the overall transmittance of the CLC cell, including the ITO electrode, alignment layer and glass substrates which would influence the transmittance.
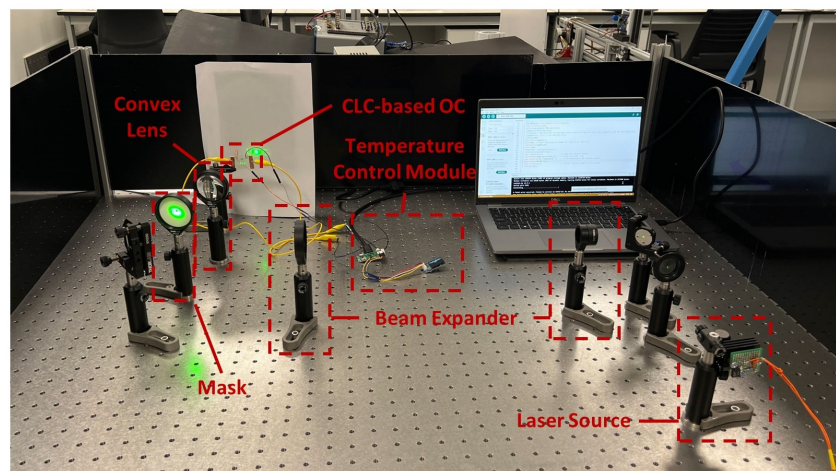
(a)
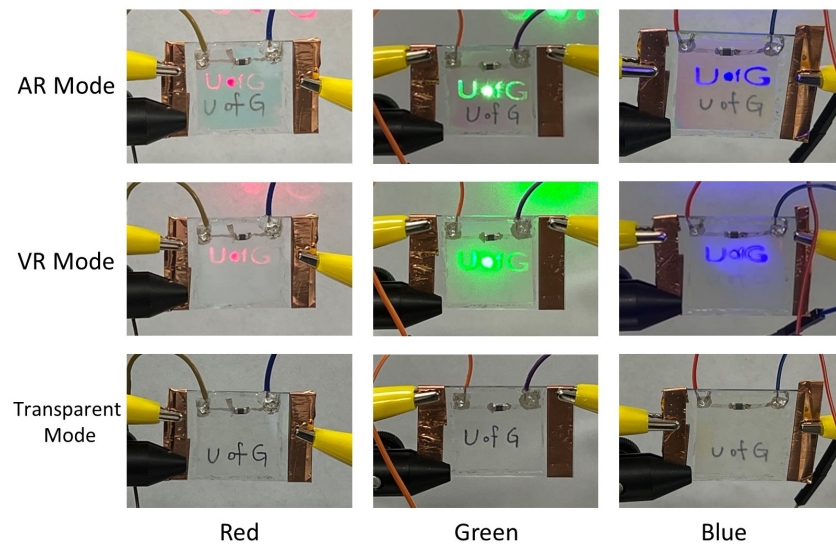
(b)

Figure 6.5: (a) An Optic system to project virtual image on CLC-based OC. (b) The result of the OC when switching between AR, VR and transparent mode with RGB laser input.

After that, 450, 532 and 635 nm of laser source are used to simulate light engine in HMDs and evaluate the performance of the tunable OCs. The optical system, shown in Fig. 6.5 (a), expands the laser beam, passes the light through the mask and projects a mask image onto a LC. The laser light is directed onto a Galilean beam expander using a one-inch mirror, where the laser spot is expanded to approximately 7 times its initial size. This magnified spot is then projected onto the mask. Finally, the mask pattern is projected onto a two-inch plano-convex lens which directs the light onto the LC.

To assess the performance of each layer of RGB OCs, measurements were taken at $32\,^{\circ}\mathrm{C}$, clear point temperature and $40\,^{\circ}\mathrm{C}$. Notably, the three different CLC materials have different clear point temperatures, which means that they reach VR mode at different temperatures. To be specific, the clear point temperature of 23%, 28% and 30% w.t. CLC cells are $36\,^{\circ}\mathrm{C}$, $34\,^{\circ}\mathrm{C}$ and $33\,^{\circ}\mathrm{C}$ respectively. Eventually, the RGB OCs were switched between three different modes with RGB laser input, which is shown in Fig. 6.5 (b). According to the results, both the background and virtual image could be seen clearly in AR mode, which is at $32\,^{\circ}\mathrm{C}$. As the temperature reached the clear point, the OCs were in VR mode, which became opaque and only virtual images could be seen. After that, the temperature was set to $40\,^{\circ}\mathrm{C}$ and laser input was turned off to simulate transparent mode. In transparent mode, the OC had maximum transparency and acted like normal glass.

Eventually, the RGB CLC cells were cascaded and heated to $32\,^{\circ}\mathrm{C}$, $36\,^{\circ}\mathrm{C}$ and $40\,^{\circ}\mathrm{C}$, which corresponded to AR mode, VR mode and transparent mode, respectively. It is noticeable that when the VR mode is at $35\,^{\circ}\mathrm{C}$, 28% and 30% w.t. CLCs are in isotropic phase and 23% w.t. CLC is around clear point thus the OC exhibits opacity. Transmittance was measured by a spectrometer, as shown in Fig 6.6. According to the result, in AR mode, the OCs were able to block around 60% of light in the RGB range from the environment, which could increase the contrast ratio of the virtual image. In VR mode, the OCs were opaque and the transmittance was lower than 5%, which could effectively block the vision of the HMD user so that the user could only see the virtual image. In transparent mode, the CLC materials
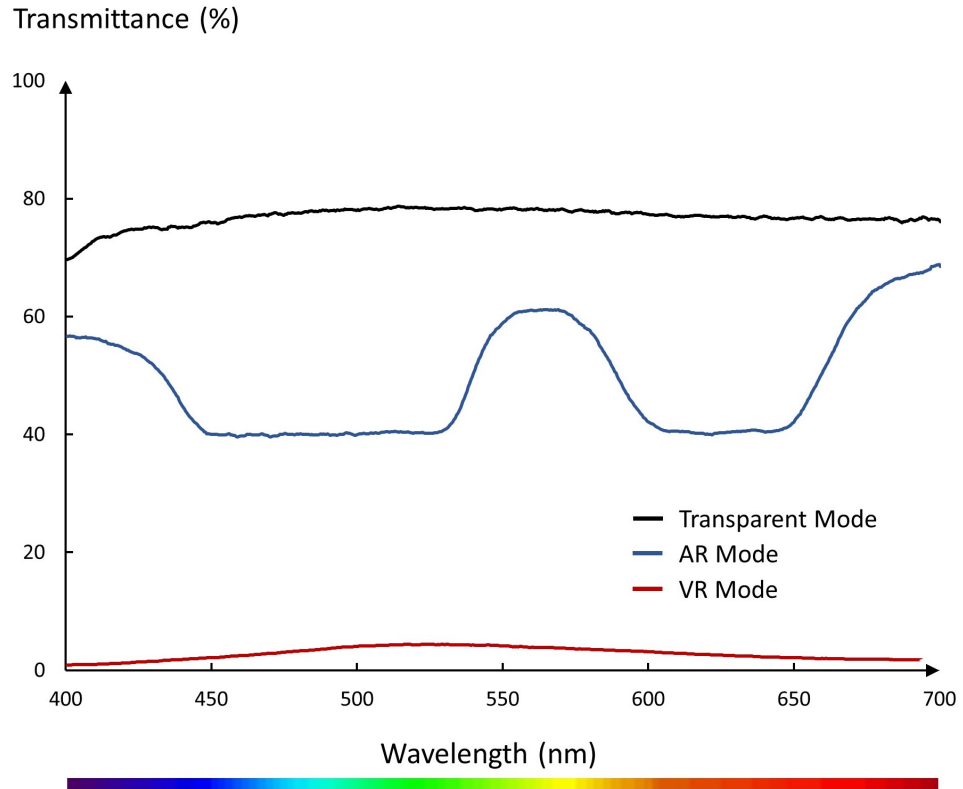
Figure 6.6: This figure shows the transmittance of AR, VR and transparent mode of the tunable OC at visible spectrum (400 - 700 nm).

were in isotropic phase and the OCs exhibited maximum transmittance. According to the result, the transparent mode could have transmittance up to 80%, which was significantly higher than AR and VR modes. In this case, the HMD could be regarded as 'off mode' and just like normal glasses. According to the results, the CLC-based OCs demonstrated good optical performance and were able to be switched between three different modes via temperature variation.

6.4 Conclusion

In this chapter, CLC-based OCs were proposed to realize seamless switching between AR, VR and transparent modes of HMDs. The optic properties of CLC materials can be changed via temperature variation. Specifically, CLCs will transform from LC phase to isotropic phase as temperature increases, which exhibit selective reflection, opacity and transparency at three different temperatures. In AR mode, CLC material showed the selective reflection property, which could block RGB light in the environment to increase the contrast of the virtual images. In VR mode, CLC material was close to the clear point and its helical structure was destroyed which led to an opaque of the OC. Therefore, the HMD user could not see the real environment but only the virtual image. In transparent mode, the temperature was above the clear point of the CLC material, which means the CLC material is fully transformed to isotropic phase. In the isotropic phase, the CLC material became transparent and maximized the transmittance of the OC. In the result section, the transmittances of the OCs were measured at three different modes, which showed good consistency with the simulation result. Additionally, virtual images were displayed on the OC in different modes to evaluate its performance. Generally, these CLC-based OCs demonstrated good reconfigurability and were able to be switched between three different modes. This technology is promising to be applied to futuristic HMDs and head-up display applications.

Thermal Controlled Cholesteric Liquid Crystal Wavelength Filter Lens for Photosensitive Epilepsy Treatment

This chapter introduced a potential approach to preventing photosensitive epilepsy by developing a thermal-controlled CLC wavelength filter lens. The lens exhibits excellent optical tunability, allowing it to dynamically change its stop band in response to temperature variations. At room temperature, the stop band of the CLC lens is not in the visible spectrum, so the lens acts like a normal glass lens. As the temperature increased to 36.5 $°C$, the lens effectively blocks light with wavelengths between 660 and 720 nm, which is known as the trigger wavelength of photosensitive epilepsy. CLC materials with opposite handedness are employed to provide over 98% cut-off of light at the stop band. In order to drive the CLC lenses, we proposed a smart glasses system that is able to monitor and dynamically control the temperature in real-time. A thermistor was mounted on the CLC cell as a temperature sensor, with the sensor data transmitted to an external microcontroller. Subsequently, the microcontroller will control the voltage added to CLC cell to adjust the temperature based on the feedback. The potential application of tunable lenses in photosensitive epilepsy treatment is a promising avenue for mitigating the impact of specific light stimuli on affected individuals.

7.1 Introduction

As is motioned in Chapter 2, a CLC-based optic filter is designed on the basis of its properties to block certain wavelengths of light. For example, excessive exposure to blue light from electronic devices might induce photoreceptor damage and biorhythm disorder, which could be prevented by color-filtered glasses [261, 262]. Moreover, selective reflection could be utilized to prevent photo-triggered diseases, for example, dyslexia and photosensitive epilepsy. Photosensitive epilepsy is a type of epilepsy in which seizures are triggered by exposure to flashing or flickering lights or certain visual patterns. Seizures can vary in severity and can range from brief episodes of altered consciousness to convulsions and loss of consciousness [263]. The trigger for photosensitive epilepsy is visual stimuli that cause rapid and repetitive changes in the intensity or patterns of light. This can include flickering lights, flashing lights, or contrasting geometric patterns. Common sources of visual triggers include video games, television shows or movies, and strobe lights at concerts or parties. In particular, light with wavelengths of 660 to 720 nm would trigger photosensitive epilepsy [264, 265]. According to previous research, color-filtered glasses have been applied to epilepsy treatment by blocking the light waveband that causes epilepsy [266]. The colored glasses could filter around 50% of red light, which significantly reduced epilepsy symptoms, including dizziness due to fluorescent lighting and aura caused by computer screens.

However, the colored glasses from the conventional epilepsy treatment are fixed, which means that they cannot adjust their optical properties according to the environment. For epilepsy patients, only a few scenarios are likely to be exposed to the light that would trigger photosensitive epilepsy, for example, using a smartphone and playing video games. Therefore, conventional colored glasses are not convenient for patients. In this case, I proposed a CLC-based tunable color filter glasses for epilepsy treatment that could switch its working mode to adapt to a different environment. The CLC-based lens could be designed to block the band of light from 660 to 720 nm, where the wavelength of the

block band could be controlled by temperature variation. Moreover, I proposed a dual-layer CLC lens configuration in which left-handed cholesteric liquid crystal (LHCLC) and right-handed cholesteric liquid crystal (RHCLC) layers are cascaded to provide a maximum cutoff of the target wavelength from 660 to 720 nm.

In previous research, researchers used the properties of CLCs to selectively reflect or transmit specific wavelengths of light based on temperature changes [255, 256]. By controlling the temperature of the CLC filter, the pitch of the CLC material is changed, thereby altering the reflected or transmitted wavelength. Since the pitch of the LC helix is temperature-dependent, previous research used a transparent electrode to generate heat. When the pitch of the cholesteric LC matches the wavelength of the incident light, the light is reflected and creates a specific band of color. According to previous research, researchers found the relationship between voltage and LC cell temperature, and then obtained the relationship between voltage and center frequency of the reflection band. However, the mapping from voltage to reflect waveband is not rigorous. The effect of environment temperature on the LC cell cannot be neglected, which will lead to systematic error. For example, lower room temperature will result in higher heat dissipation, thereby lower room temperature will result in lower LC cell temperature when input power is the same. This systematic error will largely affect the precision of the waveband filter in practical use. To eliminate this systematic error, I proposed a built-in temperature sensor in the CLC cell to monitor the temperature of the CLC material in real-time.

7.2   Methods

7.2.1   Theory and Calculations

To design a waveband filter for photosensitive epilepsy treatment, the target wavelength is between 660 to 720 nm, which would trigger photosensitive epilepsy. E7 is a specific mixture of LC compounds with a nematic phase, which consists of a mixture of various LC compounds, including 5CB, 7CB, 8OCB and 5CT. Compared with other pure substances of LC material, E7 demonstrates significant stability at different temperatures. It exhibits a nematic phase approximately at -55 °C to 60 °C, where, for example, 5CB is in LC phase from 22.5 °C to 35 °C [267, 111, 112]. Therefore, E7 has been extensively used in LCD technologies. To prepare CLC material to block the target waveband, nematic LC material needs to be mixed with chiral dopants to introduce chirality, which will result in the helical structure of nematic LC material. The ratio between the nematic LC host E7 and the chiral dopant will affect the pitch length 'P' and other characteristics of the CLC. Here, S811 and R811 are used in our design, as is shown in Fig. 7.1. These two chiral dopants have the same molecular formula, but are able to introduce opposite handedness to NLC materials due to their opposite chemical structure.
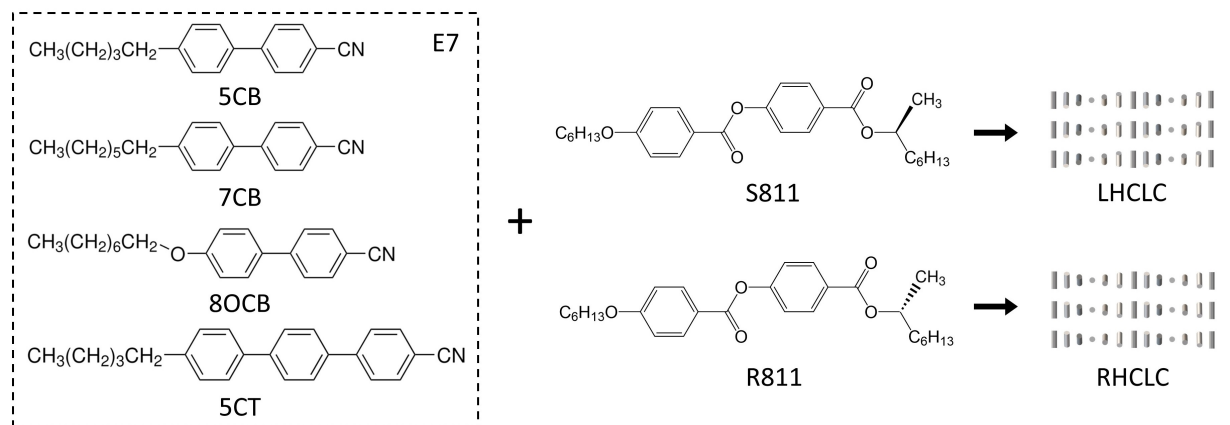
Figure 7.1: The chemical structure of related LC materials and chiral dopants. Opposite handedness of chiral dopants can introduce different orientations of helical structures.

The central wavelength and bandwidth of Bragg reflection could be calculated by refractive indexes and pitch length. Noticeably, due to the anisotropy of LC material, the refractive index has two values along and perpendicular to the LC director, which are n_e and n_o, respectively [259]. The central wavelength and bandwidth of Bragg reflection at normal incidence could be calculated by equation 6.1 to 6.3 [268]. E7 is a specific mixture of LC compounds with a nematic phase, which consists of a mixture of various LC compounds, including 5CB, 7CB, 8OCB and 5CT. The refractive index of E7 n_o and n_e is 1.53 and 1.75 respectively [196]. According to the formula, the target pitch length is 429 nm and the width of the notch band is 96.8 nm, which can cover the wavelength of the CLC cell. Subsequently, the transmittance of the CLC cell at different wavelengths could be simulated using the Berreman 4×4 method, as was mentioned in Chapter 2. To prevent photosensitive epilepsy, 660 to 720 nm wavelengths of light need to be filtered by the glasses. Therefore, the transmittance of the CLC cell with a central wavelength of 690 nm is simulated, and the result is demonstrated in the result section.

7.2.2   System Design

To achieve the reconfigurable CLC lens, a system was designed to monitor and dynamically control the selective reflection band of CLC lens in real time, as is shown in Fig. 7.2a. As discussed previously, the selective reflection band is related to the pitch length of CLC material, and the pitch length can be modulated by adjusting the temperature, thus here I proposed a feedback system for real-time temperature control. The lens consists of indium tin oxide (ITO) coated glass, an alignment layer, a spacer, a CLC layer and a cover glass with a temperature sensor. Specifically, a DC voltage source was employed on the ITO-coated glass to generate heat. A negative NTC thermistor was placed on a thin cover glass to continuously monitor the variation of temperature. Notably, NTC means the resistance of the thermistor decreases as its temperature increases. The thickness of a cover glass is around 100 μm, which could significantly minimize the impact of heat dissipation within the glass layers and enable quicker responses to temperature shifts.

After that, the difference between the actual temperature and the target temperature is used as input to an external controller, which can adjust the voltage added to CLC cell. Subsequently, the controller produces a pulse-width modulation (PWM) signal to control a MOSFET, which varies the voltage across the ITO glass via different duty cycles, as is shown in Fig. 7.2a. The MOSFET acts as a relay, preventing potential large currents on the ITO glass from affecting the operation of the microcontroller. Moreover, a Proportional-Integral-Derivative (PID) algorithm was employed within the system to dynamically control the temperature, which can enable the system to quickly stabilize at the target temperature.
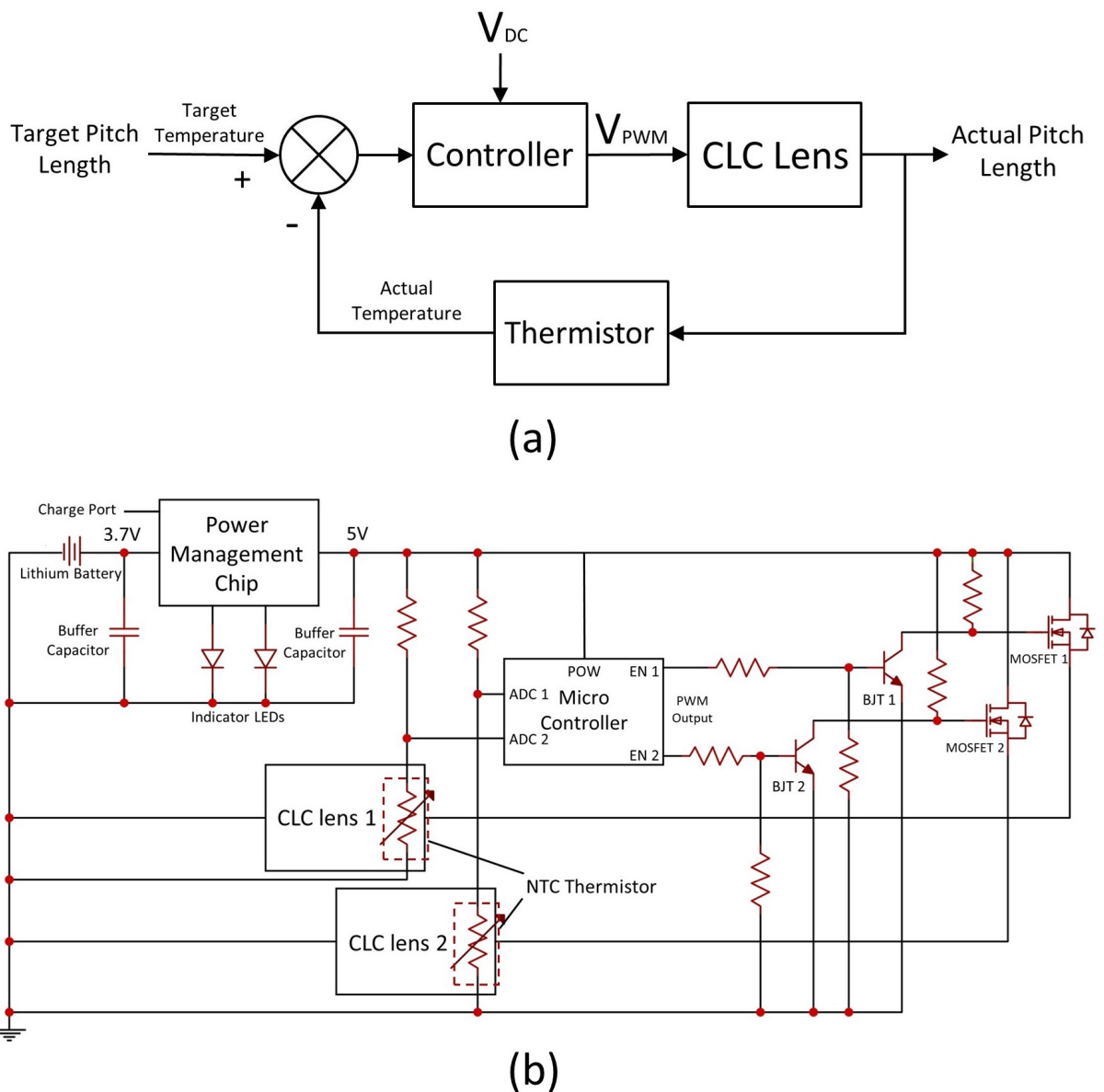
Figure 7.2: (a) The feedback system for dynamically controlling the pitch length of CLC lenses. (b) Simplified schematic diagram of the controller system design.

Subsequently, this system design was achieved via circuit design, where a simplified schematic diagram of the electronic system is demonstrated in Fig. 7.2b. Power for this setup is sourced from a 3.7 V lithium battery, which is desirable for wearable devices. The 3.7 V input is boosted to 5 V via a power management module. Subsequently, a voltage division circuit was used to convert the variations of thermistor resistance into voltage variations, which were read by the ADC pin on the microcontroller. In addition, the microcontroller can communicate with external devices via Bluetooth, which enables users to switch the modes of the glasses via smartphone or computer. After the temperature data from the thermistor was received by the microcontroller, a PID algorithm was used to convert the difference between the target temperature and actual temperature into a control signal and out from the 'EN' port. Noticeably, the control signals were PWM waves, allowing for the adjustment of the duty cycle to regulate the voltage applied across the CLC lenses. Moreover, bipolar junction transistors (BJTs) were worked as a current source in the system and coupled with resistors to produce enabling signals for MOSFETs. Eventually, the adjusted voltage was applied to the CLC lenses and maintained a selective reflection band at the target wavelength.

Preparation of Cholesteric Liquid Crystal

Researchers have studied how different proportions of NLC E7 and chiral dopant S811 would result in different pitch lengths [255]. Therefore, 21% w.t. CLC materials were employed in this work to block trigger wavelength for photosensitive epilepsy from 660 to 720 nm. According to our simulation, CLC materials with a 429 nm pitch length are required to block light in the range. Additionally, cascading a LHCLC cell and a RHCLC cell with the same pitch length can block over 95% of light within the target band. To prepare LHCLC material with 429 nm pitch length, E7 (SYNTHON Chemicals) and

S811 (95%, Sigma-Alrich) are mixed with 21% w.t. at 50 °*C*. Similarly, E7 and R811 (98%, Sigma-Alrich) are mixed with 21% w.t. at 50 °*C* to prepare RHCLC material. The CLC materials were well mixed by ultrasonic bath for 30 mins and cooled down to room temperature, then it became thick and clouded fluid.

7.2.3 Sensor Integration

In order to monitor the temperature in real-time, a temperature-sensing system should be integrated into the lens. There are many optional sensors for temperature monitoring, including thermistors, thermocouples and infrared thermometers. After evaluating the dimensions and characteristics of different sensors, the thermistor has been selected as a temperature sensor in the system. A NTC surface-mounted thermistor was integrated into the glass lens. Unlike PCBs, soldering electronic components on glass-based samples is challenging. Firstly, the circuit was printed on cover glass using silver paint with a shadow mask. Subsequently, the thermistor was adhered to the desirable position by optical adhesive NOA68 and exposed to UV light for 10 minutes. This step is to fix the thermistor on the cover glass. After that, silver paint was used to establish a connection between the thermistor and wires.

7.2.4 Fabrication of Liquid Crystal Cell

The fabrication of the CLC-based lens is demonstrated in Fig. 7.3. In step *a*, the 50×50 mm glass substrate was cleaned via IPA with an ultrasonic bath for 5 mins. This step was to clean the substrate so that the electrode material could be better attached to its surface. After that, as is shown in step *b*, an ITO layer with 1500 Å thickness was deposited on the glass substrate using sputter coated (Moorfield), which sheet resistance is around 13 Ω/sq and average transmittance at visible spectrum is around 87%. The step

c is to coat a layer of PMMA (4% solid content anisole solvent, AllResist) as alignment material. Mechanical rubbing of the substrate surfaces in one direction using cloth can create microscopic grooves which guide the LC molecules to align parallel to the direction of rubbing. After that, the top glass slide is placed on the bottom substrate with a 6 *μm* Mylar film spacer between them. Then, UV adhesive (NOA68) was smeared on the edge of the cell to fix the gap between the two substrates. After that, the cell was exposed to UV light to cure the adhesive material, then the Mylar film spacer was extracted. Till now, an empty LC cell was fabricated. Subsequently, the cell was placed on a hot plate and heated to 45 °C and a droplet of 21% wt. CLC material was dropped at one edge of the cell, where the LC material would flow into the empty cell due to surface tension. Noticeably, the temperature of the hot plate should be higher than the clear point of the LC material, so that the LC material will transform into an isotropic phase and speed up the process. The following step was to seal the rest of the two edges after the LC cell was filled with LC material, which prevented leakage of LC material and contamination. All previous process, as is demonstrated in Fig. 7.3 *a* to *g*, was to fabricate a single layer LC cell. Subsequently, steps *h* to *k* were to repeat processes from *d* to *g* and fabricate another CLC layer. Lastly, step *i* was to mount an NTC thermistor onto the CLC cell to monitor its temperature in real-time.
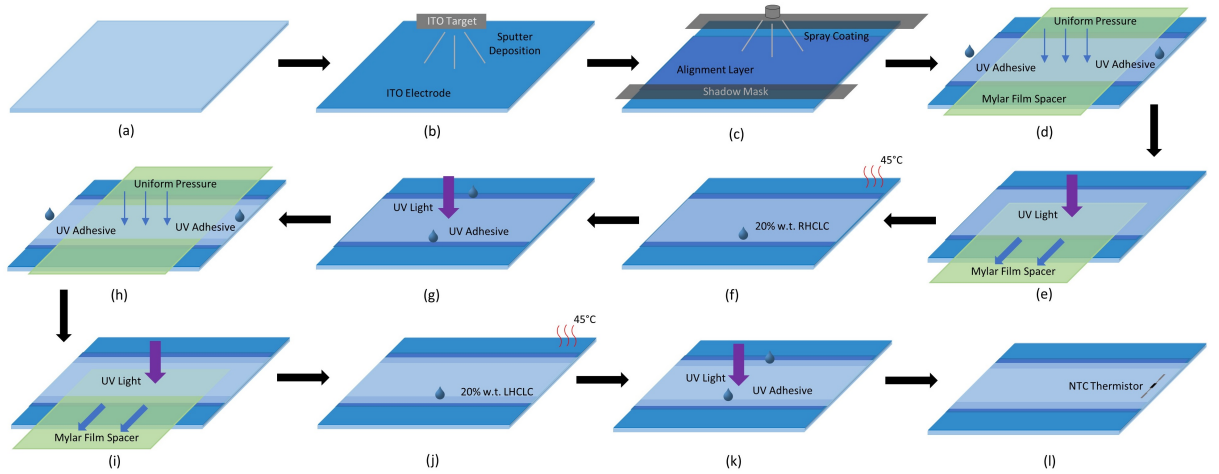
Figure 7.3: Fabrication process of a dual-layer CLC. (a) A 5×5 cm glass substrate. (b) Sputter coating of ITO electrode. (c) Spray coating alignment layer with shadow mask. (d) Fix two glass slides with Mylar film spacer and UV adhesive. (e) Cure UV adhesive and extract film spacer. (f) Place a droplet of CLC material at the edge of the empty cell, and heat the sample to 45 °C. (g) After CLC material filling the gap between two glass slides, sealing the rest two edges of CLC cell with UV adhesive. (h) Add another glass slide on top of the cell, and fix the gap with film spacer. (i)-(k) Repeating step (e)-(g). (l) Mount a thermistor and print circuit on the CLC cell for temperature monitoring.

7.2.5   Measurement and Characterization

The thickness of the electrode and alignment layers were measured via a profilometer (DektakXT, Bruker). The sheet resistance of the ITO electrode was measured using the four-point probe method with a Hall Effect Measurement System (Nanometrics). Thermal analysis was taken by DSC instrument (DSC 25, TA Instrument). Here, the heating cycle was set from 0 to 60 °C (ramp 10 °C/minute) to measure the melting point and clear point of 21% w.t. CLC materials. The heating cycle was repeated three times in the measurement. Noticeably, the observed differences in phase transitional points between heating and cooling processes arise from the enantiotropic and monotropic nature of LC materials, where phase transitional points during cooling have relatively smaller values compared with heating. The transmission spectrum of CLC lenses was measured by a spectrometer (USB2000+ fiber optic, Ocean Optics). During the measurement, the samples were heated to the target temperature, where the stop band was located at the trigger frequency of photosensitive epilepsy. Subsequently, the samples were cooled to room tem-

perature, and six measurements of transmission spectrum were taken during the period, which enabled us to obtain the relationship between temperature and selective reflection band. An infrared thermal camera (Testo 865) was used to calibrate the thermistor after the fabrication of CLC cells. This step is to establish the correlation between temperature and the resistance of the thermistor. Noticeably, the calibration process is necessary for each individual CLC cell since discrepancies in thermistor resistance might cause a system error. Additionally, the infrared thermal camera was used to capture a thermal image of the sample to showcase that the sample was heated uniformly.

7.3   Results and Discussion

To block light within the wavelength range of 660 to 720 nm, 21% w.t. LHCLC and RHCLC materials are employed. Subsequently, DSC analysis was executed to measure the heat flow of the materials, where phase transition temperature could be measured. According to the result, two materials exhibit similar thermal properties, as is shown in Fig. 7.4a. During the heating process, this 21% w.t. CLC materials exhibit LC phase from 21.02 to 44.76 $°C$. Additionally, this material exhibits LC phase from 15.98 to 40.86 $°C$ during the cooling cycle. Thus, the melting point and clear point of the CLC material are from 15.98 to 21.02 $°C$ and from 40.86 to 44.76 $°C$, respectively. Therefore, the temperature of the CLC cell is required to be controlled within 21.02 to 40.86 $°C$ to ensure the material in the LC phase. However, when the temperature is close to the clear point, the heat will destroy the helical structure of the CLC material, which results in the opacity of the CLC cell. Therefore, in the application, I maintain the operation temperature lower than 38 $°C$ to ensure the transmittance. In addition, the transmittance of LHCLC and RHCLC cells at different temperatures was measured, as is shown in Fig. 7.4b and c. It is noticeable that the waveform of the transmittance of LHCLC filters is similar to that of RHCLC filters, however, not exactly the same. For example, the selective reflection band of LHCLC material is slightly wider than that of RHCLC material. Moreover, LHCLC

demonstrated lower transmittance at the center wavelength of the selective reflection band. This difference is a result of the difference in purity of the chiral dopants S811 (95%) and R811 (98%). According to the measurement, the relationship between wavelength and temperature could be obtained, as is demonstrated in Fig. 7.4d. The trigger wavelength of photosensitive epilepsy is from 660 to 720 nm, which could be blocked by these two CLC materials at 36.5 $°C$.
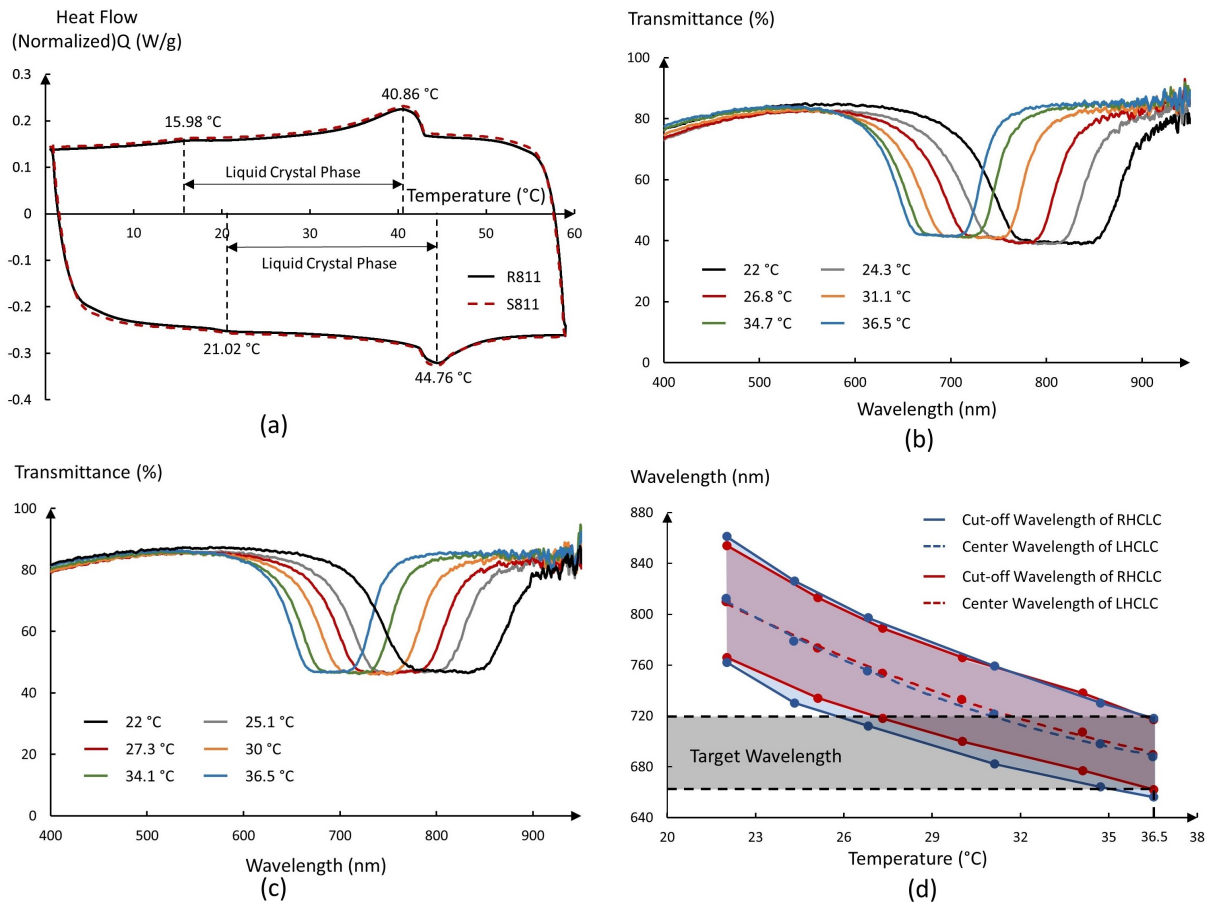
Figure 7.4: (a) DSC analysis of 21% w.t. S811:E7 LHCLC and R811:E7 RHCLC material. (b) The selective reflection of LHCLC at different temperatures. (c) The selective reflection of RHCLC at different temperatures. (d) The cut-off wavelength and center wavelength of selective reflection at different temperatures.

Therefore, 36.5 $°C$ was set as the target temperature range to activate the optical filter of CLC lenses to protect epilepsy patients. The visible spectrum varies among individuals, but it is commonly considered to span from 400 to 720 nm [269, 270]. At room temperature (approximately 25 $°C$), the reflection band of the CLC lens is not in the visible light range, thus the filter could be regarded as 'OFF'. At 36.5 $°C$, the reflection band is located at

around 660 to 720 nm, where the filter could be regarded as 'ON'. Therefore, based on its optical properties, I designed a tunable CLC filter lens that can be switched via temperature. As is shown in Fig. 7.5, the selective reflection of CLC materials with 429 and 503 nm pitch length are simulated using the Berreman 4×4 method, which could be matched with the experimental result of 21% w.t. LHCLC and RHCLC materials at 22 $^{\circ}C$ and 36.5 $^{\circ}C$.
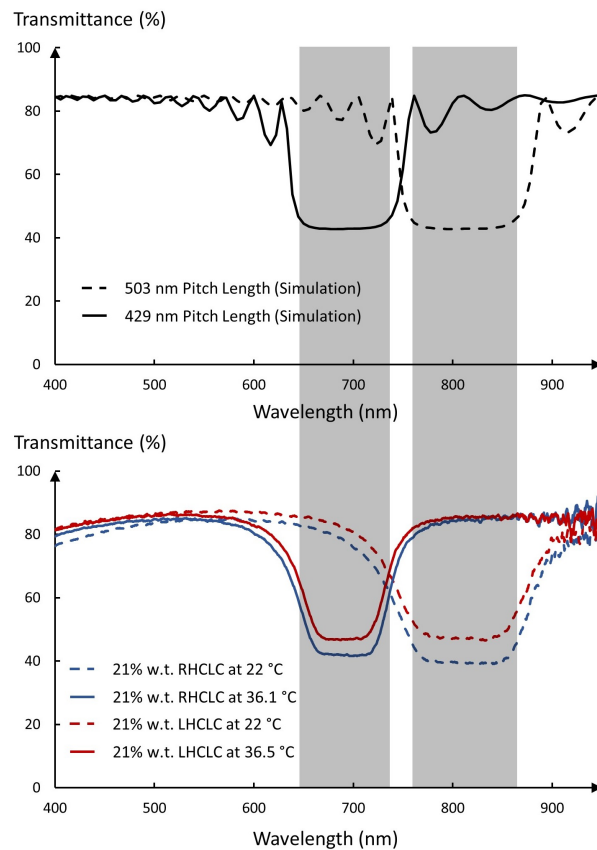
Figure 7.5: The simulation results of the CLC cell with pitch lengths of 429 nm and 503 nm are compared to experimental results of 21% w.t. RHCLC and LHCLC at 22 $^{\circ}C$ and 36.5 $^{\circ}C$.

A prototype of the color filter glasses is demonstrated in Fig. 7.6a. The figure showcases the alteration in background color when the filter was switched on and off. Moreover, the infrared thermal profile images of the CLC lens showcase that heat was uniformly distributed, which ensures the uniformity of the reflection of the target wavelength. The PCB design for the control system is demonstrated on the right side of the figure. The PCB is $48 \times 20mm$ in size, which is ideal for wearable applications. Subsequently, the spectrum

diagrams of dual-layer CLC lenses were shown in Fig. 7.6b. When the filter is off, the CLC lenses allow maximum transmittance in the visible spectrum. As the temperature rose to 36.5 °C, the filter was switched on, which is able to block over 98% of the target wavelength of light. The heating cycle is shown in Fig. 7.6c. Here, I repeated the heating cycle for 5 times, including heating, dynamic temperature control and cooling process, which showcased the good stability of the system.
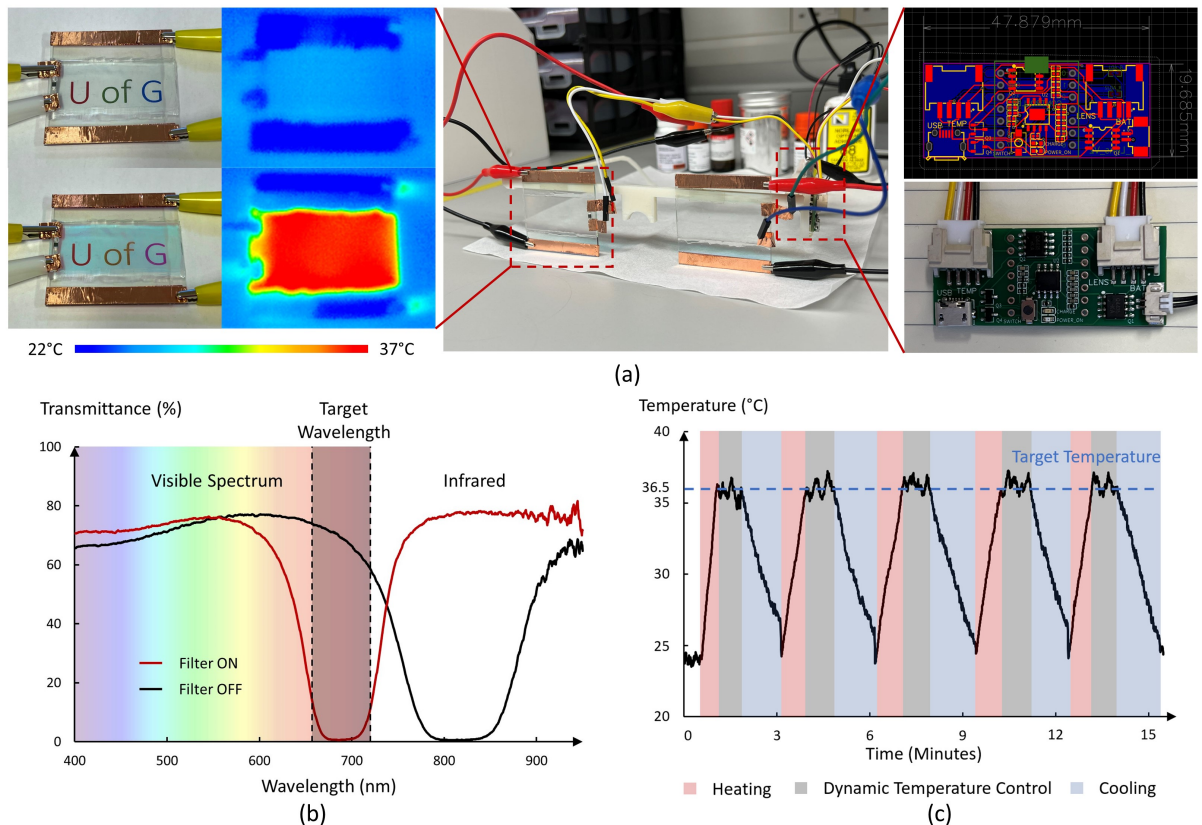
Figure 7.6: (a) The prototype of tunable glasses for photosensitive epilepsy. (b) The transition of the stop band when switching on and off the filter. (c) Heating cycle of the CLC lens.

7.4 Conclusion

In this chapter, I presented a novel tunable glasses lens that has the potential to be used for photosensitive epilepsy treatment using CLC materials. In the result section, the lenses exhibited outstanding optical tunability and were capable of varying the reflection band via temperature. At room temperature (around 25 $°C$), the reflection band of the CLC lens exceeds 720 nm, which is beyond the visible spectrum. Therefore, the lenses exhibited good transmittance within the visible spectrum, which could be considered as normal glasses lenses. To protect epilepsy patients, the lenses are required to be heated to 36.5 $°C$, ensuring that light with wavelengths between 660 and 720 nm is blocked. In evaluating the design, I noticed that the prototype works functionally when room temperature does not exceed 26 $°C$. It enables the tunable lenses suitable for the majority of scenarios since the trigger light sources normally come from digital devices, for example, video games and movies. If the environmental temperature exceeds 26 $°C$, a portion of the reflection band falls within the visible spectrum, which might influence the user experience. To cater to usage demand at high temperatures, chiral dopants with high HTP could be introduced to modify the sensitivity of CLC materials to temperature. Additionally, it is a general conclusion that light within 660 and 720 nm can trigger photosensitive epilepsy. However, different individuals have different trigger wavelengths [271, 272]. This issue could be solved by calibrating the working temperature of the CLC lenses. Moreover, the weight percentage of CLC materials could be further adjusted to cater to the requirements of the user.

Furthermore, these tunable glasses could be extended to other applications. For example, dyslexia is known as reading disorder, which might also result in writing and spelling ability disorders. Moreover, up to 20% of the general population may be affected by different degrees of dyslexia [273]. Based on the literature regarding dyslexia, researchers discovered that wearing yellow or blue filter glasses can help dyslexia patients [274, 275]. Apart from that, reading efficiency could be improved by highlighting words or sen-

tences [276]. Therefore, tunable color filter glasses could help dyslexia patients focus on reading. Additionally, researchers discovered that excessive exposure to blue light, particularly emitted from digital screens and LED lighting, can disrupt circadian rhythms by suppressing melatonin production, leading to sleep disturbances and potential long-term implications for overall well-being [277–279]. A tunable blue light filter glasses could be then developed to mitigate prolonged exposure to blue light for computer users [280, 281]. The tunable feature would enable the users to switch the glasses to normal mode in daily life.

The main challenge of the current prototype is to reduce the heating and cooling period, which might result in inconvenience of users. To address this problem, refining the design of the lens structure or incorporating advanced electrodes with improved thermal conductivity might help expedite the temperature changes. On the material aspect, a possible solution is to explore CLC materials with higher sensitivity to temperature, which enable larger stop band shifts with small temperature variations. Despite the presence of defects, this prototype successfully demonstrated the feasibility of employing CLC lenses to filter certain wavelength of light that is harmful to people. The lens exhibited tunability through temperature variation, showcasing its potential as an adaptable and responsive solution for filtering harmful light. Further refinement and optimization of the CLC lenses could lead to a more robust and reliable solution for practical applications.

Chapter 8

Conclusion and Future Outlook

In the last few decades, wearable devices have experienced rapid development. These advanced wearable devices can enhance the interaction between humans and electronic devices. In my thesis, I have explored how these reconfigurable can be used in various wearable applications that involve HMI with our eyes.

In Chapter 1, I reviewed previous research in the areas of smart contact lenses and smart glasses, and determined my research question based on the systematic survey, which informed the rest of my research question: 'Can LCs be used to facilitate HMI using our eyes?'. To address the research question, I introduced LC materials in Chapter 2, covering physical properties, common LC materials, mathematical modeling methods, and applications of LCs. Afterwards, I introduced the materials and techniques used in the fabrication of LC cells in Chapter 3, which included electrode materials, alignment methods, related materials, common types of spacers, and the fabrication process of a single-layer LC cell. Subsequently, in Chapter 4, I explored techniques for depositing transparent electrodes, proposing a method for depositing AgNW material on patterned surfaces. This work explores the impact of different concentrations of AgNW suspension on transmittance and sheet resistance. This work presents a feasible solution for depositing nanowires on pat-

terned surfaces using low-cost, easily fabricated PVC substrates. Future research will focus on exploring alternative post-processing techniques to enhance sheet resistance without compromising substrate transmittance. The outcome of this chapter could be applied to the next generation of LC-based optical devices, such as tunable Fresnel lenses and ZBDs.

In the subsequent chapters, I explored three applications that employed LCs to enhance the HMI in smart glasses. In Chapter 5, I proposed a reconfigurable antenna design for 5G wearable applications, which is a simulation-based work. The study explored how LC alignment and electric field significantly tuned antennas in the gigahertz range. This tunable antenna operated at ultra-low driving voltages (0.4-0.6 V), which was able to tune the resonant frequency of the antenna in the high-frequency range (3.3-3.8 GHz). In the context of smart glasses applications, where previous antenna designs were fixed on the eyeglass frame, the presented work showcased a reconfigurable design achievable on the lens itself using LC material. This work is simulation-based, and the future work is to fabricate the tunable antenna. In Chapter 6, I demonstrated CLC-based OCs which were able to seamlessly switch between AR, VR and transparent modes in HMD applications. The optic properties of CLC materials can be altered by varying temperatures, transitioning from LC phase to isotropic phase. This transformation results in selective reflection, opacity and transparency at different temperatures. In AR mode, the CLC material exhibits selective reflection, enhancing virtual image contrast by blocking RGB light from the environment. In VR mode, the CLC material becomes opaque, obstructing the view of the real environment and displaying only the virtual image. In transparent mode, the CLC material transforms to an isotropic phase, becoming fully transparent and maximizing the OC's transmittance. Furthermore, in chapter 7, I introduced an innovative tunable glasses lens designed for the treatment of photosensitive epilepsy using CLC materials. In the result section, the lenses exhibited exceptional optical tunability, capable of altering the reflection band through temperature adjustments. At room temperature (approximately 25 $°C$), the reflection band of the CLC lens was outside the visible spectrum, allowing for good transmittance within the visible range, resembling normal glass lenses. To protect epilepsy patients, the lenses need to be heated to 36.5

$°C$, effectively blocking light with wavelengths between 660 and 720 nm. This prototype successfully demonstrated the feasibility of utilizing CLC lenses to filter specific harmful wavelengths of light. Chapters 6 and 7 investigate the manipulation of CLC materials using temperature, which requires a lower driving voltage compared to traditional electric field control methods. However, the limitation of the prototype is the long heating and cooling period, potentially causing inconvenience for users. From a materials perspective, a potential solution is to investigate CLC materials which are more sensitive to temperatures. This characteristic would facilitate a more significant shift in the selective reflection band with minimal temperature variation. I will continue to work on the prototype to improve its performance in the future.
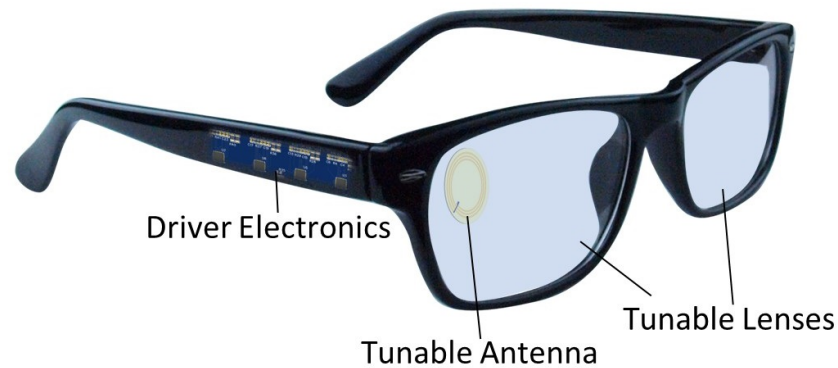
Figure 8.1: A futuristic smart glasses design involving tunable antenna and tunable lenses.

This thesis comprehensively explores the diverse applications of LC materials in wearable applications, extending beyond traditional LCD applications. In the thesis, I proposed three solutions utilizing LC materials to facilitate HMI using our eyes, which successfully answered my research question. Both tunable antenna and tunable filter lenses can be potentially integrated into one smart glasses design, as shown in Fig. 8.1. During my PhD journey, I gained expertise in LC material simulation, LC device fabrication, 3D modeling and electronic system design. Over the past three years, I have published four journal papers and four conference papers, contributing significantly to the advancements in this

field. Additionally, I currently have two journal papers under review, further demonstrating my contribution to this respective domain. I will continue work in this field after graduation, with a specific focus on implementing LC materials in the next generation of AR devices, including head-up displays (HUDs) and AR glasses.

Bibliography

1. Chen, C.-Y., Hasan, M. & Mohan, S. Securing real-time internet-of-things. *Sensors* **18,** 4356 (2018).

2. Wright, K. W. in *Pediatric Ophthalmology and Strabismus* 125–143 (Springer, 2003).

3. Carpenter, R. H. *Movements of the Eyes, 2nd Rev* (Pion Limited, 1988).

4. Leigh, R. J. & Zee, D. S. *The neurology of eye movements* (OUP USA, 2015).

5. Kohli, A. A., Woo, J. & Tamhankar, M. A. Cranial Nerve Palsies: What's New? *Advances in Ophthalmology and Optometry* **3,** 261–278 (2018).

6. Ludwig, P. E., Aslam, S. & Czyz., C. N. *Anatomy, Head and Neck, Eye Muscles* 2020. https://www.ncbi.nlm.nih.gov/books/NBK470534/.

7. Soukupova, T. & Cech, J. *Eye blink detection using facial landmarks* in *21st computer vision winter workshop, Rimske Toplice, Slovenia* (2016), 1–45.

8. Cheung, Y.-m. & Peng, Q. Eye gaze tracking with a web camera in a desktop environment. *IEEE Transactions on Human-Machine Systems* **45,** 419–430 (2015).

9. Corcoran, P. M., Nanu, F., Petrescu, S. & Bigioi, P. Real-time eye gaze tracking for gaming design and consumer electronics systems. *IEEE Transactions on Consumer Electronics* **58,** 347–355 (2012).

10. Tanwear, A. *et al.* Spintronic Sensors Based on Magnetic Tunnel Junctions for Wireless Eye Movement Gesture Control. *IEEE Transactions on Biomedical Circuits and Systems* (2020).

11. Massin, L., Seguin, F., Nourrit, V., Daniel, E., Lahuec, C. *et al.* Smart Contact Lens Applied to Gaze Tracking. *IEEE Sensors Journal* **21,** 455–463 (2020).

12. Królak, A. & Strumiłło, P. Eye-blink detection system for human–computer interaction. *Universal Access in the Information Society* **11,** 409–419 (2012).

13. Morris, T., Blenkhorn, P. & Zaidi, F. Blink detection for real-time eye tracking. *Journal of Network and Computer Applications* **25,** 129–143 (2002).

14. Porter, J. D., Burns, L. A. & May, P. J. Morphological substrate for eyelid movements: innervation and structure of primate levator palpebrae superioris and orbicularis oculi muscles. *Journal of Comparative Neurology* **287,** 64–81 (1989).

15. Lahdesmaki, I., Shum, A. J. & Parviz, B. A. Possibilities for continuous glucose monitoring by a functional contact lens. *IEEE instrumentation & measurement magazine* **13,** 14–17 (2010).

16. Park, J. *et al.* Soft, smart contact lenses with integrations of wireless circuits, glucose sensors, and displays. *Science Advances* **4,** eaap9841 (2018).

17. Xinming, L. *et al.* Polymeric hydrogels for novel contact lens-based ophthalmic drug delivery systems: A review. *Contact Lens and Anterior Eye* **31,** 57–64 (2008).

18. Kim, M. *et al.* An electrochromic alarm system for smart contact lenses. *Sensors and Actuators B: Chemical* **322,** 128601 (2020).

19. González-Arribas, E. *et al.* Transparent and capacitive bioanode based on specifically engineered glucose oxidase. *Electroanalysis* **28,** 1290–1297 (2016).

20. Quintero, A. V., Pérez-Merino, P. & De Smet, H. Artificial iris performance for smart contact lens vision correction applications. *Scientific reports* **10,** 1–12 (2020).

21. Raducanu, B. C. *et al.* An Artificial Iris ASIC With High Voltage Liquid Crystal Driver, 10-nA Light Range Detector and 40-nA Blink Detector for LCD Flicker Removal. *IEEE Solid-State Circuits Letters* **3,** 506–509 (2020).

22. Farandos, N. M., Yetisen, A. K., Monteiro, M. J., Lowe, C. R. & Yun, S. H. Contact lens sensors in ocular diagnostics. *Advanced healthcare materials* **4,** 792–810 (2015).

23. Tseng, R. C., Chen, C.-C., Hsu, S.-M. & Chuang, H.-S. Contact-lens biosensors. *Sensors* **18,** 2651 (2018).

24. Kim, J., Cha, E. & Park, J.-U. Recent advances in smart contact lenses. *Advanced Materials Technologies* **5,** 1900728 (2020).

25. Xia, Y. *et al.* State-of-the-Art in Smart Contact Lenses for Human–Machine Interaction. *IEEE Transactions on Human-Machine Systems* (2022).

26. Ghannam, R., Curia, G., Brante, G., Khosravi, S. & Hua, F. Implantable and Wearable Neuroengineering Education: A Review of Postgraduate Programmes. *IEEE Access* (2020).

27. Moreddu, R., Vigolo, D. & Yetisen, A. K. Contact lens technology: from fundamentals to applications. *Advanced healthcare materials* **8,** 1900368 (2019).

28. *Smart definition and meaning: Collins English Dictionary* (Accessed: Nov. 26, 2022). `https://www.collinsdictionary.com/dictionary/english/smart`.

29. *Electronics definition and meaning | collins english dictionary* (Accessed: Nov. 26, 2022). `https://www.collinsdictionary.com/dictionary/english/electronics`.

30. *Wireless definition and meaning: Collins English Dictionary* (Accessed: Nov. 26, 2022). `https://www.collinsdictionary.com/dictionary/english/wireless`.

31. Leonardi, M., Leuenberger, P, Bertrand, D., Bertsch, A. & Renaud, P. *A soft contact lens with a MEMS strain gage embedded for intraocular pressure monitoring* in *TRANSDUCERS'03. 12th International Conference on Solid-State Sensors, Actuators and Microsystems. Digest of Technical Papers (Cat. No. 03TH8664)* **2** (2003), 1043–1046.

32. Leonardi, M., Pitchon, E. M., Bertsch, A., Renaud, P. & Mermoud, A. Wireless contact lens sensor for intraocular pressure monitoring: assessment on enucleated pig eyes. *Acta ophthalmologica* **87,** 433–437 (2009).

33. Pandey, J. *et al.* A fully integrated RF-powered contact lens with a single element display. *IEEE Transactions on Biomedical Circuits and Systems* **4,** 454–461 (2010).

34. Yao, H., Afanasiev, A., Lähdesmäki, I. & Parviz, B. A. *A dual microscale glucose sensor on a contact lens, tested in conditions mimicking the eye* in *2011 Ieee 24th International Conference on Micro Electro Mechanical Systems* (2011), 25–28.

35. Choi, K. & Park, H. G. Smart reinvention of the contact lens with graphene. *ACS nano* **11,** 5223–5226 (2017).

36. Rabensteiner, D. F., Rabensteiner, J. & Faschinger, C. The influence of electromagnetic radiation on the measurement behaviour of the triggerfish® contact lens sensor. *BMC ophthalmology* **18,** 1–5 (2018).

37. Kusama, S., Sato, K., Yoshida, S. & Nishizawa, M. Self-Moisturizing Smart Contact Lens Employing Electroosmosis. *Advanced Materials Technologies* **5,** 1900889 (2020).

38. Khaldi, A. *et al.* A laser emitting contact lens for eye tracking. *Scientific Reports* **10,** 1–8 (2020).

39. Yao, H., Shum, A. J., Cowan, M., Lähdesmäki, I. & Parviz, B. A. A contact lens with embedded sensor for monitoring tear glucose level. *Biosensors and Bioelectronics* **26,** 3290–3296 (2011).

40. Chen, G.-Z., Chan, I.-S. & Lam, D. C. Capacitive contact lens sensor for continuous non-invasive intraocular pressure monitoring. *Sensors and Actuators A: Physical* **203,** 112–118 (2013).

41. Zhang, Y. *et al.* High resolution non-invasive intraocular pressure monitoring by use of graphene woven fabrics on contact lens. *Microsystems & nanoengineering* **5,** 1–8 (2019).

42. Vasquez Quintero, A., Arai, R., Yamazaki, Y., Sato, T. & De Smet, H. Near-Field Communication Powered Hydrogel-Based Smart Contact Lens. *Advanced Materials Technologies* **5,** 2000702 (2020).

43. Chiou, J.-C. *et al.* Toward a wirelessly powered on-lens intraocular pressure monitoring system. *IEEE journal of biomedical and health informatics* **20,** 1216–1224 (2016).

44. Chen, L. R., Shaker, G. & Safavi-Naeini, S. *Warpage-free antenna for smart contact lens applications* in *2017 IEEE International Symposium on Antennas and Propagation & USNC/URSI National Radio Science Meeting* (2017), 1293–1294.

45. Kim, J. *et al.* Wearable smart sensor systems integrated on soft contact lenses for wireless ocular diagnostics. *Nature communications* **8,** 1–8 (2017).

46. Lingley, A. R., Otis, B. P., Shen, T. T. & Parviz, B. A. A contact lens with integrated micro solar cells. *Microsystem technologies* **18,** 453–458 (2012).

47. Falk, M. *et al.* Biofuel cell as a power source for electronic contact lenses. *Biosensors and Bioelectronics* **37,** 38–45 (2012).

48. Takamatsu, T., Chen, Y., Yoshimasu, T., Nishizawa, M. & Miyake, T. Highly Efficient, Flexible Wireless-Powered Circuit Printed on a Moist, Soft Contact Lens. *Advanced Materials Technologies* **4,** 1800671 (2019).

49. Lee, H., Kim, S., Kim, K.-B. & Choi, J.-W. Scalable fabrication of flexible thin-film batteries for smart lens applications. *Nano Energy* **53,** 225–231 (2018).

50. Park, J. *et al.* Printing of wirelessly rechargeable solid-state supercapacitors for soft, smart contact lenses with continuous operations. *Science advances* **5,** eaay0764 (2019).

51. Jeon, C. *et al.* A Smart Contact Lens Controller IC Supporting Dual-Mode Telemetry With Wireless-Powered Backscattering LSK and EM-Radiated RF Transmission Using a Single-Loop Antenna. *IEEE Journal of Solid-State Circuits* **55,** 856–867 (2020).

52. Kim, H., Kim, J., Kang, J. & Song, Y.-W. Three-Dimensionally Printed Interconnects for Smart Contact Lenses. *ACS applied materials & interfaces* **10,** 28086–28092 (2018).

53. Vásquez Quintero, A., Verplancke, R., De Smet, H. & Vanfleteren, J. Stretchable electronic platform for soft and smart contact lens applications. *Advanced Materials Technologies* **2,** 1700073 (2017).

54. Song, C., Ben-Shlomo, G. & Que, L. A multifunctional smart soft contact lens device enabled by nanopore thin film for glaucoma diagnostics and in situ drug delivery. *Journal of Microelectromechanical Systems* **28,** 810–816 (2019).

55. Milton, H. E., Morgan, P. B., Clamp, J. H. & Gleeson, H. F. Electronic liquid crystal contact lenses for the correction of presbyopia. *Optics express* **22,** 8035–8040 (2014).

56. Chen, J. *et al. A foveated contact lens display for augmented reality* in *Optical Architectures for Displays and Sensing in Augmented, Virtual, and Mixed Reality (AR, VR, MR)* **11310** (2020), 1131004.

57. Kuhn, K. *et al.* Managing Process Variation in Intel's 45nm CMOS Technology. *Intel Technology Journal* **12,** 93–109 (2008).

58. Kinn, J. B. & Tell, R. A. A liquid-crystal contact-lens device for measurement of corneal temperature. *IEEE Transactions on Biomedical Engineering,* 387–388 (1973).

59. Xu, S. C., Gauthier, A. C. & Liu, J. The application of a contact lens sensor in detecting 24-hour intraocular pressure-related patterns. *Journal of ophthalmology* **2016** (2016).

60. Kingman, S. Glaucoma is second leading cause of blindness globally. *Bulletin of the World Health Organization* **82,** 887–888 (2004).

61. Kim, S.-K. *et al.* Wireless smart contact lens for diabetic diagnosis and therapy. *Science Advances* **6,** eaba3252 (2020).

62. Lin, Y.-R. *et al.* Noninvasive glucose monitoring with a contact lens and smartphone. *Sensors* **18,** 3208 (2018).

63. Kim, S., Jeon, H.-J., Park, S., Lee, D. Y. & Chung, E. tear Glucose Measurement by Reflectance Spectrum of a Nanoparticle Embedded Contact Lens. *Scientific Reports* **10,** 1–8 (2020).

64. Tinku, S., Adami, A. & Lorenzelli, L. *State of the art and perspectives on the fabrication of functional contact lenses* in *Proceedings of the 2013 ACM conference on Pervasive and ubiquitous computing adjunct publication* (2013), 397–404.

65. Vanhaverbeke, C., Verplancke, R., De Smet, J., Cuypers, D. & De Smet, H. Microfabrication of a spherically curved liquid crystal display enabling the integration in a smart contact lens. *Displays* **49,** 16–25 (2017).

66. Massin, L. *et al.* Development of a new scleral contact lens with encapsulated photodetectors for eye tracking. *Optics Express* **28,** 28635–28647 (2020).

67. Brunyé, T. T., Drew, T., Weaver, D. L. & Elmore, J. G. A review of eye tracking for understanding and improving diagnostic interpretation. *Cognitive research: principles and implications* **4,** 1–16 (2019).

68. Gravina, R. & Fortino, G. Wearable body sensor networks: state-of-the-art and research directions. *IEEE Sensors Journal* **21,** 12511–12522 (2020).

69. De Smet, J. *et al.* Progress toward a liquid crystal contact lens display. *Journal of the Society for Information Display* **21,** 399–406 (2013).

70. Ghannam, R. *et al.* Reconfigurable Surfaces Using Fringing Electric Fields from Nanostructured Electrodes in Nematic Liquid Crystals. *Advanced Theory and Simulations,* 2100058 (2021).

71. Liang, X. *et al. Live Demonstration: Gaze Following System for Noninvasively Testing Electronic Contact Lens* in *2020 27th IEEE International Conference on Electronics, Circuits and Systems (ICECS)* (2020), 1–2.

72. Syberfeldt, A., Danielsson, O. & Gustavsson, P. Augmented reality smart glasses in the smart factory: Product evaluation guidelines and review of available products. *Ieee Access* **5,** 9118–9130 (2017).

73. Lee, L.-H. & Hui, P. Interaction methods for smart glasses: A survey. *IEEE access* **6,** 28712–28732 (2018).

74. Sik Lanyi, C. & Withers, J. D. A. Striving for a safer and more ergonomic workplace: Acceptability and human factors related to the adoption of AR/VR glasses in industry 4.0. *Smart Cities* **3,** 289–307 (2020).

75. Jeong, I., Kim, J., Lee, B., Choi, J. & Kwon, Y. Comparison of RF integrated passive devices on smart silicon and glass substrate. *Microwave and Optical Technology Letters* **45,** 441–444 (2005).

76. Hong, Y. & Choi, J. 60 GHz patch antenna array with parasitic elements for smart glasses. *IEEE Antennas and Wireless Propagation Letters* **17,** 1252–1256 (2018).

77. Chung, M.-A. & Hsiao, C.-W. Dual-band 6×6 MIMO antenna system for glasses applications compatible with Wi-Fi 6E and 7 wireless communication standards. *Electronics* **11,** 806 (2022).

78. Cil, E. & Dumanli, S. The design of a reconfigurable slot antenna printed on glass for wearable applications. *IEEE Access* **8,** 95417–95423 (2020).

79. Yoshida, T. *et al.* A plastic holographic waveguide combiner for light-weight and highly-transparent augmented reality glasses. *Journal of the Society for Information Display* **26,** 280–286 (2018).

80. Chiu, Y.-C., Liu, L.-Y. & Wang, T. Automatic segmentation and summarization for videos taken with smart glasses. *Multimedia Tools and Applications* **77,** 12679–12699 (2018).

81. Wang, Z. *et al.* AirMouse: Turning a pair of glasses into a mouse in the air. *IEEE Internet of Things Journal* **6,** 7473–7483 (2019).

82. Li, Y., Cheng, Y., Meng, W., Li, Y. & Deng, R. H. Designing leakage-resilient password entry on head-mounted smart wearable glass devices. *IEEE Transactions on Information Forensics and security* **16,** 307–321 (2020).

83. Hong, I. *et al.* A 2.71 nJ/pixel gaze-activated object recognition system for low-power mobile smart glasses. *IEEE Journal of Solid-State Circuits* **51,** 45–55 (2015).

84. Meyer, J., Frank, A., Schlebusch, T. & Kasneci, E. A cnn-based human activity recognition system combining a laser feedback interferometry eye movement sensor and an imu for context-aware smart glasses. *Proceedings of the ACM on Interactive, Mobile, Wearable and Ubiquitous Technologies* **5,** 1–24 (2021).

85. Meyer, J., Gering, S. & Kasneci, E. Static Laser Feedback Interferometry-Based Gaze Estimation for Wearable Glasses. *IEEE Sensors Journal* **23,** 7558–7569 (2023).

86. Hellec, J., Chorin, F., Castagnetti, A. & Colson, S. S. Sit-to-stand movement evaluated using an inertial measurement unit embedded in smart glasses—A validation study. *Sensors* **20,** 5019 (2020).

87. Archer, J. *et al.* OCOsense TM smart glasses for analyzing facial expressions using optomyographic sensors. *IEEE Pervasive Computing* (2023).

88. Kwon, J., Ha, J., Kim, D.-H., Choi, J. W. & Kim, L. Emotion recognition using a glasses-type wearable device via multi-channel facial responses. *IEEE Access* **9,** 146392–146403 (2021).

89. Doniec, R. *et al.* Classification of roads and types of public roads using EOG smart glasses and an algorithm based on machine learning while driving a car. *Electronics* **11,** 2960 (2022).

90. Ahmed, R. E. *et al.* GPark: Vehicle parking management system using smart glass. *Journal of Sensors* **2016** (2016).

91. Spandonidis, C. *et al.* Development of Visual Sensors and Augmented Reality Based Smart Glasses for Enhancement of Business Sustainability and Wellbeing of the Aging Workforce. *IEEE Instrumentation & Measurement Magazine* **26,** 21–27 (2023).

92. Xia, K. *et al.* Wearable smart multimeter equipped with AR glasses based on IoT platform. *IEEE Instrumentation & Measurement Magazine* **23,** 40–45 (2020).

93. Runji, J. M. & Lin, C.-Y. Switchable glass enabled contextualization for a cyber-physical safe and interactive spatial augmented reality PCBA manufacturing inspection system. *Sensors* **20,** 4286 (2020).

94. Chang, W.-J., Chen, L.-B. & Chiou, Y.-Z. Design and implementation of a drowsiness-fatigue-detection system based on wearable smart glasses to increase road safety. *IEEE Transactions on Consumer Electronics* **64,** 461–469 (2018).

95. Chang, W.-J. *et al.* MedGlasses: A wearable smart-glasses-based drug pill recognition system using deep learning for visually impaired chronic patients. *IEEE Access* **8,** 17013–17024 (2020).

96. Bai, J., Lian, S., Liu, Z., Wang, K. & Liu, D. Smart guiding glasses for visually impaired people in indoor environment. *IEEE Transactions on Consumer Electronics* **63,** 258–266 (2017).

97. Busaeed, S., Mehmood, R., Katib, I. & Corchado, J. M. LidSonic for Visually Impaired: Green Machine Learning-Based Assistive Smart Glasses with Smart App and Arduino. *Electronics* **11,** 1076 (2022).

98. Mukhiddinov, M. & Cho, J. Smart glass system using deep learning for the blind and visually impaired. *Electronics* **10,** 2756 (2021).

99. Matsuhashi, K., Kanamoto, T. & Kurokawa, A. Thermal model and countermeasures for future smart glasses. *Sensors* **20,** 1446 (2020).

100. Kusumi, K., Hachiya, K., Kudo, R., Kanamoto, T. & Kurokawa, A. Electronic component placement optimization for heat measures of smartglasses. *IEICE Electronics Express* **20,** 20230011–20230011 (2023).

101. Weste, N. H. & Harris, D. *CMOS VLSI design: a circuits and systems perspective* (Pearson Education, 2015).

102. IEEE. *International Roadmap for Devices and Systems (IRDS™) 2021 Edition* https://irds.ieee.org/editions/2021. Accessed: 2021-11-17. 2021.

103. Norman, G. A. V. Drugs, Devices, and the FDA: Part 1. *JACC: Basic to Translational Science* **1,** 170–179 (2016).

104. Goodby, J. W. *et al. Handbook of liquid crystals, 8 volume set* (John Wiley & Sons, 2014).

105. Kim, D.-H. *et al.* Lyotropic liquid crystal systems in drug delivery: a review. *Journal of Pharmaceutical Investigation* **45,** 1–11 (2015).

106. Simoni, F & Francescangeli, O. Effects of light on molecular orientation of liquid crystals. *Journal of Physics: Condensed Matter* **11,** R439 (1999).

107. Zhao, J., Zhang, L. & Hu, J. Varied alignment methods and versatile actuations for liquid crystal elastomers: A review. *Advanced Intelligent Systems* **4,** 2100065 (2022).

108. Hiltrop, K & Stegemeyer, H. Contact angles and alignment of liquid crystals on lecithin monolayers. *Molecular Crystals and Liquid Crystals* **49,** 61–65 (1978).

109. Gray, G. W., Vill, V., Spiess, H. W., Demus, D. & Goodby, J. W. *Physical properties of liquid crystals* (John Wiley & Sons, 2009).

110. Gray, G. W., Harrison, K. J. & Nash, J. New family of nematic liquid crystals for displays. *Electronics Letters* **6,** 130–131 (1973).

111. Elouali, M. *et al.* Dispersions of diamond nanoparticles in nematic liquid crystal/polymer materials. *Molecular Crystals and Liquid Crystals* **545,** 77–1301 (2011).

112. Zannoni, C. *Liquid Crystals and Their Computer Simulations* (Cambridge University Press, 2022).

113. Che, K.-J. *et al.* Microfluidic generation of cholesteric liquid crystal droplets with an integrative cavity for dual-gain and controllable lasing. *Lab on a Chip* **19,** 3116–3122 (2019).

114. Jau, H.-C. *et al.* Study of electro-optical properties of templated blue phase liquid crystals. *Optical Materials Express* **3,** 1516–1522 (2013).

115. Yang, D.-K. & Wu, S.-T. *Fundamentals of Liquid Crystal Devices* (John Wiley & Sons, 2014).

116. Saeva, F. & Wysocki, J. Induced circular dichroism in cholesteric liquid crystals. *Journal of the American Chemical Society* **93,** 5928–5929 (1971).

117. John, W. S., Fritz, W., Lu, Z. & Yang, D.-K. Bragg reflection from cholesteric liquid crystals. *Physical Review E* **51,** 1191 (1995).

118. De Gennes, P.-G. & Prost, J. *The physics of liquid crystals* (Oxford university press, 1993).

119. Frank, F. C. I. Liquid crystals. On the theory of liquid crystals. *Discussions of the Faraday Society* **25,** 19–28 (1958).

120. Mottram, N. J. & Newton, C. J. P. Introduction to Q-tensor theory. *arXiv e-prints* (2014).

121. Hong, M.-C. & Xin, Z. Global existence of solutions of the liquid crystal flow for the Oseen–Frank model in R2. *Advances in Mathematics* **231,** 1364–1400 (2012).

122. Svenšek, D. & Žumer, S. Hydrodynamics of pair-annihilating disclination lines in nematic liquid crystals. *Physical Review E* **66,** 021712 (2002).

123. Majumdar, A. & Zarnescu, A. Landau–de Gennes theory of nematic liquid crystals: the Oseen–Frank limit and beyond. *Archive for rational mechanics and analysis* **196,** 227–280 (2010).

124. Collings, P. J. & Hird, M. *Introduction to Liquid Crystals Chemistry and Physics* (Crc Press, 2017).

125. Barberi, R *et al.* Electric field induced order reconstruction in a nematic cell. *The European Physical Journal E* **13,** 61–71 (2004).

126. Jones, R. C. A new calculus for the treatment of optical systems. VII. Properties of the N-matrices. *Josa* **38,** 671–685 (1948).

127. Yeh, P. Extended Jones matrix method. *JOSA* **72,** 507–513 (1982).

128. Schubert, M. Polarization-dependent optical parameters of arbitrarily anisotropic homogeneous layered systems. *Physical Review B* **53,** 4265 (1996).

129. Chen, R. H. *Liquid crystal displays: fundamental physics and technology* (John Wiley & Sons, 2011).

130. Wilkinson, T., Henderson, C, Gil Leyva, D, Ghannam, R & Crossland, W. Non-display applications and the next generation of liquid crystal over silicon technology. *Philosophical Transactions of the Royal Society A: Mathematical, Physical and Engineering Sciences* **364,** 2721–2732 (2006).

131. Lindle, J. R., Watnik, A. T. & Cassella, V. A. Efficient multibeam large-angle nonmechanical laser beam steering from computer-generated holograms rendered on a liquid crystal spatial light modulator. *Applied optics* **55,** 4336–4341 (2016).

132. Mok, F., Diep, J., Liu, H.-K. & Psaltis, D. Real-time computer-generated hologram by means of liquid-crystal television spatial light modulator. *Optics Letters* **11,** 748–750 (1986).

133. Crossland, W. *et al.* Holographic optical switching: the" ROSES" demonstrator. *Journal of Lightwave Technology* **18,** 1845 (2000).

134. Curtis, J. E., Koss, B. A. & Grier, D. G. Dynamic holographic optical tweezers. *Optics communications* **207,** 169–175 (2002).

135. Zhang, Z., You, Z. & Chu, D. Fundamentals of phase-only liquid crystal on silicon (LCOS) devices. *Light: Science & Applications* **3,** e213 (2014).

136. Shields IV, C. W. *et al.* Control of the Folding Dynamics of Self-Reconfiguring Magnetic Microbots Using Liquid Crystallinity. *Advanced Intelligent Systems* **2,** 1900114 (2020).

137. Vasić, B., Isić, G., Beccherelli, R. & Zografopoulos, D. C. Tunable Beam Steering at Terahertz Frequencies Using Reconfigurable Metasurfaces Coupled With Liquid Crystals. *IEEE Journal of Selected Topics in Quantum Electronics* **26,** 1–9 (2019).

138. Quintero, A. V., Pérez-Merino, P. & Smet, H. D. Artificial iris performance for smart contact lens vision correction applications. *Scientific Reports* **10** (2020).

139. Raducanu, B. C. *et al.* An Artificial Iris ASIC With High Voltage Liquid Crystal Driver, 10-nA Light Range Detector and 40-nA Blink Detector for LCD Flicker Removal. *IEEE Solid-State Circuits Letters* **3,** 506–509 (2020).

140. Ginley, D. S. & Perkins, J. D. in *Handbook of transparent conductors* 1–25 (Springer, 2010).

141. Yim, J. H., Kim, Y. S., Koh, K. H. & Lee, S. Fabrication of transparent single wall carbon nanotube films with low sheet resistance. *Journal of Vacuum Science & Technology B: Microelectronics and Nanometer Structures Processing, Measurement, and Phenomena* **26,** 851–855 (2008).

142. De Volder, M. F., Tawfick, S. H., Baughman, R. H. & Hart, A. J. Carbon nanotubes: present and future commercial applications. *science* **339,** 535–539 (2013).

143. Thostenson, E. T., Ren, Z. & Chou, T.-W. Advances in the science and technology of carbon nanotubes and their composites: a review. *Composites science and technology* **61,** 1899–1912 (2001).

144. Garnett, E. C. *et al.* Self-limited plasmonic welding of silver nanowire junctions. *Nature materials* **11,** 241–249 (2012).

145. Park, J. *et al.* Highly Customizable Transparent Silver Nanowire Patterning via Inkjet-Printed Conductive Polymer Templates Formed on Various Surfaces. *Advanced Materials Technologies* **5,** 2000042 (2020).

146. Wei, B. *et al.* A highly conductive and smooth AgNW/PEDOT: PSS film treated by hot-pressing as electrode for organic light emitting diode. *Organic Electronics* **43,** 182–188 (2017).

147. Kulkarni, A., Schulz, K. H., Lim, T. & Khan, M. Dependence of the sheet resistance of indium-tin-oxide thin films on grain size and grain orientation determined from X-ray diffraction techniques. *Thin solid films* **345,** 273–277 (1999).

148. Minami, T. Present status of transparent conducting oxide thin-film development for Indium-Tin-Oxide (ITO) substitutes. *Thin Solid Films* **516,** 5822–5828 (2008).

149. Armstrong, N. R., Veneman, P. A., Ratcliff, E., Placencia, D. & Brumbach, M. Oxide contacts in organic photovoltaics: Characterization and control of near-surface composition in indium- tin oxide (ITO) electrodes. *Accounts of chemical research* **42,** 1748–1757 (2009).

150. Shi, H., Liu, C., Jiang, Q. & Xu, J. Effective approaches to improve the electrical conductivity of PEDOT: PSS: a review. *Advanced Electronic Materials* **1,** 1500017 (2015).

151. Lang, U., Naujoks, N. & Dual, J. Mechanical characterization of PEDOT: PSS thin films. *Synthetic Metals* **159,** 473–479 (2009).

152. Fan, X. *et al.* PEDOT: PSS for flexible and stretchable electronics: modifications, strategies, and applications. *Advanced Science* **6,** 1900813 (2019).

153. Hecht, D. S., Hu, L. & Irvin, G. Emerging transparent electrodes based on thin films of carbon nanotubes, graphene, and metallic nanostructures. *Advanced materials* **23,** 1482–1513 (2011).

154. Xu, G. *et al.* Binder-free activated carbon/carbon nanotube paper electrodes for use in supercapacitors. *Nano Research* **4,** 870–881 (2011).

155. Hu, L., Kim, H. S., Lee, J.-Y., Peumans, P. & Cui, Y. Scalable coating and properties of transparent, flexible, silver nanowire electrodes. *ACS nano* **4,** 2955–2963 (2010).

156. Mayousse, C., Celle, C., Fraczkiewicz, A. & Simonato, J.-P. Stability of silver nanowire based electrodes under environmental and electrical stresses. *Nanoscale* **7,** 2107–2115 (2015).

157. Lagrange, M *et al.* Optimization of silver nanowire-based transparent electrodes: effects of density, size and thermal annealing. *Nanoscale* **7,** 17410–17423 (2015).

158. Zhang, C., Ji, C., Park, Y.-B. & Guo, L. J. Thin-Metal-Film-Based Transparent Conductors: Material Preparation, Optical Design, and Device Applications. *Advanced Optical Materials* **9,** 2001298 (2021).

159. Huang, S., Liu, Y., Zhao, Y., Ren, Z. & Guo, C. F. Flexible electronics: stretchable electrodes and their future. *Advanced Functional Materials* **29,** 1805924 (2019).

160. Sharma, S., Sudhakara, P, Omran, A. A. B., Singh, J. & Ilyas, R. Recent trends and developments in conducting polymer nanocomposites for multifunctional applications. *Polymers* **13,** 2898 (2021).

161. Kim, S.-M. *et al.* Influence of PEDOT: PSS crystallinity and composition on electrochemical transistor performance and long-term stability. *Nature communications* **9,** 3858 (2018).

162. Hiltrop, K, Hasse, J & Stegemeyer, H. On the alignment of thermotropic nematic and smectic liquid crystals on lecithin coated surfaces. *Berichte der Bunsengesellschaft für physikalische Chemie* **98,** 209–213 (1994).

163. Gwag, J. S. *et al.* A functionally separated nanoimprinting material tailored for homeotropic liquid crystal alignment. *Nanotechnology* **19,** 395301 (2008).

164. Park, H.-G. *et al.* Homeotropic alignment of liquid crystals on a nano-patterned polyimide surface using nanoimprint lithography. *Soft Matter* **7,** 5610–5614 (2011).

165. Prost, J. & Pershan, P. S. Flexoelectricity in nematic and smectic-A liquid crystals. *Journal of Applied Physics* **47,** 2298–2312 (1976).

166. Van Aerle, N. & Tol, A. Molecular orientation in rubbed polyimide alignment layers used for liquid-crystal displays. *Macromolecules* **27,** 6520–6526 (1994).

167. Ge, J. J. *et al.* Rubbing-induced molecular reorientation on an alignment surface of an aromatic polyimide containing cyanobiphenyl side chains. *Journal of the American Chemical Society* **123,** 5768–5776 (2001).

168. Wei, X., Hong, S.-C., Zhuang, X., Goto, T. & Shen, Y. Nonlinear optical studies of liquid crystal alignment on a rubbed polyvinyl alcohol surface. *Physical Review E* **62,** 5160 (2000).

169. Cui, Y., Zola, R. S., Yang, Y.-C. & Yang, D.-K. Alignment layers with variable anchoring strengths from Polyvinyl Alcohol. *Journal of Applied Physics* **111** (2012).

170. Geary, J., Goodby, J., Kmetz, A. & Patel, J. The mechanism of polymer alignment of liquid-crystal materials. *Journal of applied physics* **62,** 4100–4108 (1987).

171. Rastegar, A, Škarabot, M, Blij, B & Rasing, T. Mechanism of liquid crystal alignment on submicron patterned surfaces. *Journal of Applied Physics* **89,** 960–964 (2001).

172. Park, J.-Y. & Kim, H.-K. Highly stretchable polymer-dispersed liquid crystal-based smart windows with transparent and stretchable hybrid electrodes. *RSC advances* **8,** 36549–36557 (2018).

173. Ober, C. K., Jin, J.-I., Zhou, Q. & Lenz, R. W. *Liquid crystal polymers with flexible spacers in the main chain* in *Liquid Crystal Polymers I* (1984), 103–146.

174. Park, H.-G., Byun, S.-U., Jeong, H.-C., Lee, J.-W. & Seo, D.-S. Photoreactive spacer prepared using electrohydrodynamic printing for application in a liquid crystal device. *ECS Solid State Letters* **2,** R52 (2013).

175. Kamiya, T. & Hosono, H. Material characteristics and applications of transparent amorphous oxide semiconductors. *NPG Asia Materials* **2,** 15–22 (2010).

176. Langley, D. *et al.* Flexible transparent conductive materials based on silver nanowire networks: a review. *Nanotechnology* **24,** 452001 (2013).

177. Ellmer, K. Past achievements and future challenges in the development of optically transparent electrodes. *Nature Photonics* **6,** 809–817 (2012).

178. Park, S., Vosguerichian, M. & Bao, Z. A review of fabrication and applications of carbon nanotube film-based flexible electronics. *Nanoscale* **5,** 1727–1752 (2013).

179. Takemoto, A. *et al.* Printable transparent microelectrodes toward mechanically and visually imperceptible electronics. *Advanced Intelligent Systems* **2,** 2000093 (2020).

180. Qiu, Y., Ma, S., Pei, Q. & Holbery, J. D. A Self-Conformable Smart Skin with Sensing and Variable Stiffness Functions. *Advanced Intelligent Systems* **1,** 1900054 (2019).

181. Lee, J.-Y., Connor, S. T., Cui, Y. & Peumans, P. Solution-processed metal nanowire mesh transparent electrodes. *Nano letters* **8,** 689–692 (2008).

182. Madaria, A. R., Kumar, A., Ishikawa, F. N. & Zhou, C. Uniform, highly conductive, and patterned transparent films of a percolating silver nanowire network on rigid and flexible substrates using a dry transfer technique. *Nano research* **3,** 564–573 (2010).

183. Lu, Y. & Chou, K. Tailoring of silver wires and their performance as transparent conductive coatings. *Nanotechnology* **21,** 215707 (2010).

184. Scardaci, V., Coull, R., Lyons, P. E., Rickard, D. & Coleman, J. N. Spray deposition of highly transparent, low-resistance networks of silver nanowires over large areas. *Small* **7,** 2621–2628 (2011).

185. Liu, C.-H. & Yu, X. Silver nanowire-based transparent, flexible, and conductive thin film. *Nanoscale research letters* **6,** 1–8 (2011).

186. Kim, C.-L., Lee, J.-Y., Shin, D.-G., Yeo, J.-S. & Kim, D.-E. Mechanism of heat-induced fusion of silver nanowires. *Scientific reports* **10,** 1–8 (2020).

187. Tokuno, T. *et al.* Fabrication of silver nanowire transparent electrodes at room temperature. *Nano research* **4,** 1215–1222 (2011).

188. Jones, J. C. *et al. Novel bistable liquid crystal displays based on grating alignment* in *Liquid Crystal Materials, Devices, and Flat Panel Displays* **3955** (2000), 84–93.

189. Bryan-Brown, G. P. & Jones, J. C. The Zenithal Bistable Display: A grating aligned bistable nematic liquid crystal device. *E-Paper Displays,* 131–152 (2022).

190. Spencer, T., Care, C., Amos, R. & Jones, J. Zenithal bistable device: comparison of modeling and experiment. *Physical Review E* **82,** 021702 (2010).

191. Sato, S., Sugiyama, A. & Sato, R. Variable-focus liquid-crystal Fresnel lens. *Japanese journal of applied physics* **24,** L626 (1985).

192. Sato, S, Nose, T, Yamaguchi, R & Yanase, S. Relationship between lens properties and director orientation in a liquid crystal lens. *Liquid Crystals* **5,** 1435–1442 (1989).

193. Lou, Y., Chen, L., Wang, C. & Shen, S. Tunable-focus liquid crystal Fresnel zone lens based on harmonic diffraction. *Applied Physics Letters* **101,** 221121 (2012).

194. Ghannam, R. *et al.* Reconfigurable Surfaces Using Fringing Electric Fields from Nanostructured Electrodes in Nematic Liquid Crystals. *Advanced Theory and Simulations* **4,** 2100058 (2021).

195. James, R., Willman, E., Ghannam, R., Beeckman, J. & Fernández, F. A. Hydrodynamics of fringing-field induced defects in nematic liquid crystals. *Journal of Applied Physics* **130,** 134701 (2021).

196. Xia, Y. *et al.* Reconfigurable Wearable Antenna for 5G Applications using Nematic Liquid Crystals. *arXiv preprint arXiv:2212.08622* (2022).

197. Lin, Y.-H., Wang, Y.-J. & Reshetnyak, V. Liquid crystal lenses with tunable focal length. *Liquid Crystals Reviews* **5,** 111–143 (2017).

198. Xiong, J., Hsiang, E.-L., He, Z., Zhan, T. & Wu, S.-T. Augmented reality and virtual reality displays: emerging technologies and future perspectives. *Light: Science & Applications* **10** (2021).

199. Yin, K. *et al.* Advanced liquid crystal devices for augmented reality and virtual reality displays: principles and applications. *Light: Science & Applications* **11** (2022).

200. Park, K.-I. *et al.* Flexible nanocomposite generator made of BaTiO3 nanoparticles and graphitic carbons. *Advanced materials* **24,** 2999–3004 (2012).

201. Leem, D.-S. *et al.* Efficient organic solar cells with solution-processed silver nanowire electrodes. *Advanced materials* **23,** 4371–4375 (2011).

202. Stapleton, A. J. *et al.* Planar silver nanowire, carbon nanotube and PEDOT: PSS nanocomposite transparent electrodes. *Science and technology of advanced materials* (2015).

203. Karimullah, A. S. *Application of conducting polymer electrodes in cell impedance sensing* PhD thesis (University of Glasgow, 2012).

204. Smits, F. Measurement of sheet resistivities with the four-point probe. *Bell System Technical Journal* **37,** 711–718 (1958).

205. Lingley, A. R. *et al.* A single-pixel wireless contact lens display. *Journal of Micromechanics and Microengineering* **21,** 125014 (2011).

206. Kim, D., Kim, K., Kim, H., Choi, M. & Na, J.-H. Design Optimization of Reconfigurable Liquid Crystal Patch Antenna. *Materials* **14,** 932 (2021).

207. Martin, N., Laurent, P., Person, C., Gelin, P. & Huret, F. *Patch antenna adjustable in frequency using liquid crystal* in *33rd European Microwave Conference Proceedings (IEEE Cat. No. 03EX723C)* **2** (2003), 699–702.

208. Jakoby, R., Gaebler, A. & Weickhmann, C. Microwave liquid crystal enabling technology for electronically steerable antennas in SATCOM and 5G millimeter-wave systems. *Crystals* **10,** 514 (2020).

209. Huang, L. & Russer, P. Electrically tunable antenna design procedure for mobile applications. *IEEE Transactions on Microwave Theory and Techniques* **56,** 2789–2797 (2008).

210. Hum, S. V., Okoniewski, M. & Davies, R. J. Realizing an electronically tunable reflectarray using varactor diode-tuned elements. *IEEE Microwave and Wireless Components Letters* **15,** 422–424 (2005).

211. Bildik, S. *et al. Reconfigurable liquid crystal reflectarray with extended tunable phase range* in *2011 41st European Microwave Conference* (2011), 1292–1295.

212. Perez-Palomino, G. *et al.* Design and demonstration of an electronically scanned reflectarray antenna at 100 GHz using multiresonant cells based on liquid crystals. *IEEE Transactions on Antennas and Propagation* **63,** 3722–3727 (2015).

213. Romanofsky, R. R. *et al.* K-band phased array antennas based on Ba/sub 0.60/Sr/sub 0.40/TiO/sub 3/thin-film phase shifters. *IEEE Transactions on Microwave Theory and Techniques* **48,** 2504–2510 (2000).

214. Gaebler, A *et al.* Liquid crystal-reconfigurable antenna concepts for space applications at microwave and millimeter waves. *International Journal of Antennas and Propagation* **2009** (2009).

215. Park, H. *et al.* Evaluating liquid crystal properties for use in terahertz devices. *Optics Express* **20,** 11899–11905 (2012).

216. Yang, J. *et al.* Electrically tunable reflective terahertz phase shifter based on liquid crystal. *Journal of Infrared, Millimeter, and Terahertz Waves* **39,** 439–446 (2018).

217. Hong, S., Kang, S. H., Kim, Y. & Jung, C. W. Transparent and flexible antenna for wearable glasses applications. *IEEE Transactions on Antennas and Propagation* **64,** 2797–2804 (2016).

218. Chung, M.-A., Hsiao, C.-W., Yang, C.-W. & Chuang, B.-R. 4× 4 MIMO antenna system for smart eyewear in Wi-Fi 5G and Wi-Fi 6E wireless communication applications. *Electronics* **10,** 2936 (2021).

219. Jones, R., Melnyk, O., Macêdo, R. & Camley, R. E. Vertically Stacked Soliton-Like Domain Walls in Nematic Liquid Crystals. *Advanced Theory and Simulations* **4,** 2100252 (2021).

220. Klasen, M. *et al.* Calculation of optical and dielectric anisotropy of nematic liquid crystals. *Japanese Journal of Applied Physics* **37,** L945 (1998).

221. Jiang, H. *et al.* Light-weight, flexible, low-voltage electro-thermal film using graphite nanoplatelets for wearable/smart electronics and deicing devices. *Journal of Alloys and Compounds* **699,** 1049–1056 (2017).

222. Borkar, S. & Pande, H. *Application of 5G next generation network to Internet of Things* in *2016 International Conference on Internet of Things and Applications (IOTA)* (2016), 443–447.

223. Toney, M. F. *et al.* Near-surface alignment of polymers in rubbed films. *Nature* **374,** 709–711 (1995).

224. Coles, H. Laser and electric field induced birefringence studies on the cyanobiphenyl homologues. *Molecular Crystals and Liquid Crystals* **49,** 67–74 (1978).

225. Miroshnychenko, D., Hill, N., Mottram, N. & Lydon, J. Evolution from a+ 2 defect to+ 1/2 defects in a cylindrical geometry. *Molecular Crystals and Liquid Crystals* **437,** 251–1495 (2005).

226. Cummins, P., Dunmur, D. & Laidler, D. The Dielectric Properties of Nematic 44 n-pentylcyanobiphenyI. *Molecular Crystals and Liquid Crystals* **30,** 109–123 (1975).

227. Blinov, L. M. & Chigrinov, V. G. *Electrooptic Effects in Liquid Crystal Materials* (Springer Science & Business Media, 1996).

228. Wang, H., Wu, T. X., Zhu, X. & Wu, S.-T. Correlations between liquid crystal director reorientation and optical response time of a homeotropic cell. *Journal of Applied Physics* **95,** 5502–5508 (2004).

229. Podoliak, N. *Magneto-optic effects in colloids of ferromagnetic nanoparticles in nematic liquid crystals* PhD thesis (University of Southampton, 2012).

230. Al-Qurainy, L. A. & Al Naimee, K. A. Temperature Effects on Liquid Crystal Nonlinearity. *Liquid Crystals, Recent Advancements in Fundamental and Device Technologies,* 159–176 (2017).

231. Baghernia, E., Movahedinia, R. & Sebak, A.-R. Broadband compact circularly polarized spiral antenna array fed by printed gap waveguide for millimeter-wave applications. *IEEE Access* **9,** 86–95 (2020).

232. Egorov, I. & Ying, Z. *A non-uniform helical antenna for dual-band cellular phones* in *IEEE Antennas and Propagation Society International Symposium. Transmitting Waves of Progress to the Next Millennium. 2000 Digest. Held in conjunction with: USNC/URSI National Radio Science Meeting (C* **2** (2000), 652–655.

233. Access, E. U. T. R. User Equipment (UE) radio transmission and reception. *3GPP TS* **36,** V10 (2011).

234. Pozar, D. M. *Microwave Engineering* (John wiley & sons, 2011).

235. Lin, J. C. A new IEEE standard for safety levels with respect to human exposure to radio-frequency radiation. *IEEE Antennas and Propagation Magazine* **48,** 157–159 (2006).

236. Xu, G. *et al.* Differential probe fed liquid crystal-based frequency tunable circular ring patch antenna. *IEEE Access* **6,** 3051–3058 (2017).

237. Sun, S.-Y. *et al.* Electronically tunable liquid-crystal-based F-band phase shifter. *IEEE Access* **8,** 151065–151071 (2020).

238. Missaoui, S., Missaoui, S. & Kaddour, M. Electrically tuned microwave CP cross slot patch antenna using liquid crystal technology. *Electromagnetics* **39,** 158–167 (2019).

239. Fang, W. *et al.* Head-mounted display augmented reality in manufacturing: A systematic review. *Robotics and Computer-Integrated Manufacturing* **83,** 102567 (2023).

240. Anthes, C., García-Hernández, R. J., Wiedemann, M. & Kranzlmüller, D. *State of the art of virtual reality technology* in *2016 IEEE aerospace conference* (2016), 1–19.

241. Burdea, G. C. & Coiffet, P. *Virtual reality technology* (John Wiley & Sons, 2003).

242. Carmigniani, J. & Furht, B. Augmented reality: an overview. *Handbook of augmented reality,* 3–46 (2011).

243. Billinghurst, M., Clark, A., Lee, G. *et al.* A survey of augmented reality. *Foundations and Trends® in Human–Computer Interaction* **8,** 73–272 (2015).

244. Rokhsaritalemi, S., Sadeghi-Niaraki, A. & Choi, S.-M. A review on mixed reality: Current trends, challenges and prospects. *Applied Sciences* **10,** 636 (2020).

245. Pointecker, F., Friedl, J., Schwajda, D., Jetter, H.-C. & Anthes, C. *Bridging the gap across realities: Visual transitions between virtual and augmented reality* in *2022 IEEE International Symposium on Mixed and Augmented Reality (ISMAR)* (2022), 827–836.

246. Teixeira, J. M., Ferreira, R., Santos, M. & Teichrieb, V. *Teleoperation using google glass and ar, drone for structural inspection* in *2014 xvi symposium on virtual and augmented reality* (2014), 28–36.

247. Xiong, J., Hsiang, E.-L., He, Z., Zhan, T. & Wu, S.-T. Augmented reality and virtual reality displays: emerging technologies and future perspectives. *Light: Science & Applications* **10,** 216 (2021).

248. Putilin, A., Morozov, A., Kopenkin, S., Dubynin, S. & Borodin, Y. P. Holographic waveguide periscopes in augmented reality displays. *Optics and Spectroscopy* **128,** 1828–1836 (2020).

249. Liu, Z. *et al.* Metasurface-enabled augmented reality display: a review. *Advanced Photonics* **5,** 034001–034001 (2023).

250. Cakmakci, O., Qin, Y., Bosel, P. & Wetzstein, G. Holographic pancake optics for thin and lightweight optical see-through augmented reality. *Optics Express* **29,** 35206–35215 (2021).

251. Chen, Q. *et al.* Multi-plane augmented reality display based on cholesteric liquid crystal reflective films. *Optics Express* **27,** 12039–12047 (2019).

252. Xiong, J., Tan, G., Zhan, T. & Wu, S.-T. Wide-view augmented reality display with diffractive cholesteric liquid crystal lens array. *Journal of the Society for Information Display* **28,** 450–456 (2020).

253. Zou, J. *et al.* High dynamic range head-up displays. *Optics Express* **28,** 24298–24307 (2020).

254. Stebryte, M. Reflective optical components based on chiral liquid crystal for head-up displays. *Liquid Crystals Today* **30,** 36–45 (2021).

255. Tzeng, S.-Y., Chen, C.-N. & Tzeng, Y. Thermal tuning band gap in cholesteric liquid crystals. *Liquid Crystals* **37,** 1221–1224 (2010).

256. Froyen, A. A., Wübbenhorst, M., Liu, D. & Schenning, A. P. Electrothermal color tuning of cholesteric liquid crystals using interdigitated electrode patterns. *Advanced Electronic Materials* **7,** 2000958 (2021).

257. Born, M. & Wolf, E. *Principles of optics: electromagnetic theory of propagation, interference and diffraction of light* (Elsevier, 2013).

258. Hsiang, E.-L. *et al.* AR/VR light engines: Perspectives and challenges. *Advances in Optics and Photonics* **14,** 783–861 (2022).

259. Dierking, I. *Textures of liquid crystals* (John Wiley & Sons, 2003).

260. Chen, W.-R. & Hwang, J.-C. The phase behaviour and optical properties of a nematic/chiral dopant liquid crystalline mixture system. *Liquid crystals* **31,** 1539–1546 (2004).

261. Tosini, G., Ferguson, I. & Tsubota, K. Effects of blue light on the circadian system and eye physiology. *Molecular vision* **22,** 61 (2016).

262. Bedrosian, T. & Nelson, R. Timing of light exposure affects mood and brain circuits. *Translational psychiatry* **7,** e1017–e1017 (2017).

263. Harding, G. F. & Jeavons, P. M. *Photosensitive epilepsy* **133** (Cambridge University Press, 1994).

264. Fisher, R. S., Harding, G., Erba, G., Barkley, G. L. & Wilkins, A. Photic-and pattern-induced seizures: a review for the Epilepsy Foundation of America Working Group. *Epilepsia* **46,** 1426–1441 (2005).

265. Okudan, Z. V. & Özkara, Ç. Reflex epilepsy: triggers and management strategies. *Neuropsychiatric disease and treatment,* 327–337 (2018).

266. Wilkins, A. J. *et al.* Treatment of photosensitive epilepsy using coloured glasses. *Seizure* **8,** 444–449 (1999).

267. Bedjaoui-Alachaher, L., Bensaid, H., Gordin, C. & Maschke, U. Solubility effects of multicomponent liquid crystal blends towards poly (n-butyl-acrylate). *Liquid Crystals* **38,** 1315–1320 (2011).

268. Mitov, M. Cholesteric liquid crystals with a broad light reflection band. *Advanced Materials* **24,** 6260–6276 (2012).

269. Palczewska, G. *et al.* Human infrared vision is triggered by two-photon chromophore isomerization. *Proceedings of the National Academy of Sciences* **111,** E5445–E5454 (2014).

270. Schnapf, J., Kraft, T. & Baylor, D. Spectral sensitivity of human cone photoreceptors. *Nature* **325,** 439–441 (1987).

271. Takahashi, Y, Fujiwara, T, Yagi, K & Seino, M. Photosensitive epilepsies and pathophysiologic mechanisms of the photoparoxysmal response. *Neurology* **53,** 926–926 (1999).

272. Takahashi, Y., Fujiwara, T., Yagi, K. & Seino, M. Wavelength dependence of photoparoxysmal responses in photosensitive patients with epilepsy. *Epilepsia* **40,** 23–27 (1999).

273. Stoker, G. *et al.* Dyslexia and related disorders reporting study. *American Institutes for Research* (2019).

274. Stein, J. Dyslexia: the role of vision and visual attention. *Current developmental disorders reports* **1,** 267–280 (2014).

275. Singleton, C. & Trotter, S. Visual stress in adults with and without dyslexia. *Journal of Research in Reading* **28,** 365–378 (2005).

276. Ikeshita, H., Yamaguchi, S., Morioka, T. & Yamazoe, T. Effects of Highlighting Text on the Reading Ability of Children with Developmental Dyslexia: A Pilot Study. *International Journal of Emerging Technologies in Learning* **13** (2018).

277. Wahl, S., Engelhardt, M., Schaupp, P., Lappe, C. & Ivanov, I. V. The inner clock— Blue light sets the human rhythm. *Journal of biophotonics* **12,** e201900102 (2019).

278. Hatori, M. *et al.* Global rise of potential health hazards caused by blue light-induced circadian disruption in modern aging societies. *npj Aging and Mechanisms of Disease* **3,** 9 (2017).

279. Tähkämö, L., Partonen, T. & Pesonen, A.-K. Systematic review of light exposure impact on human circadian rhythm. *Chronobiology international* **36,** 151–170 (2019).

280. Sasseville, A., Paquet, N., Sévigny, J. & Hébert, M. Blue blocker glasses impede the capacity of bright light to suppress melatonin production. *Journal of pineal research* **41,** 73–78 (2006).

281. Van der Lely, S. *et al.* Blue blocker glasses as a countermeasure for alerting effects of evening light-emitting diode screen exposure in male teenagers. *Journal of Adolescent Health* **56,** 113–119 (2015).